

ABSTRACT

RODKWAN, SUPASIT. A Numerical and Experimental Investigation of the Machinability of Elastomers. (Under the direction of Dr. John S. Strenkowski.)

In this dissertation, the machinability of elastomers is investigated. The main objective of the research is to determine the machining conditions for which an elastomer can be machined with a smooth surface finish. Both machining experiments and numerical simulations were carried out to achieve this goal. For the experimental studies, a series of orthogonal machining tests were conducted to investigate the effects of various machining parameters on chip morphology, machined surface condition, and resulting machining forces. Feed speed and rake angle were found to have a significant effect on the type of chip generated during orthogonal machining. High feed speed conditions and large rake angle tools produced long and continuous ribbon-like chips and a corresponding smooth machined surface. The design of the workpiece fixture in the lathe was also found to be critical for machining smooth surfaces.

In the numerical investigation, half-wedge indentation and orthogonal cutting models were developed to simulate incipient separation of elastomers. It was found that high tensile normal stress and maximum principal stresses, as well as a large concentrated strain energy density near the separation point lead to favorable conditions for the formation of continuous chips and a good surface finish. The indentation simulations correlated well with the cutting tests in which tools with a large rake angle and large feed produced continuous chips and a smooth surface finish. The models offer potential for identifying the cutting conditions and tools that produce a smooth machined surface finish of elastomers.

**A NUMERICAL AND EXPERIMENTAL INVESTIGATION
OF THE MACHINABILITY OF ELASTOMERS**

by

SUPASIT RODKWAN

A dissertation submitted to the Graduate Faculty of
North Carolina State University
in partial fulfillment of the
requirements for the Degree of
Doctor of Philosophy

MECHANICAL AND AEROSPACE ENGINEERING

Raleigh

2002

APPROVED BY:

Chair of Advisory Committee

*Dedicated to my parents, my wife and...
my aunt, Sa-ngiam Sawasdisarn, who passed away before I complete my degree
just only one month, her kindness would never be forgotten.*

BIOGRAPHY

Supasit Rodkwan was born in Bangkok, Thailand in 1969. He was an only child in the family raised by his mother, Preeya Rodkwan and his father, Chid Rodkwan. He graduated from Samsenwittayalai High School in Bangkok where his mother spent her almost entire career as a teacher in social science and history. His father, who received his Master degree in Public Administration from Syracuse University in 1972, has recently retired as a vice-governor at Satool province in southern region of Thailand. In 1990, Mr. Rodkwan received his Bachelor of Engineering degree in Mechanical Engineering from King Mongkut University of Technology Thonburi in Thailand. Soon after his graduation, he began his professional career as a mechanical engineer in a mechanical erection department at TPI Polene Co., Ltd., one of the largest cement production companies in Thailand. In 1993, he came to pursue his graduate study at the University of Southern California where he received his Master of Science in Mechanical Engineering with a concentration in Computer Aided Design/Computer Aided Manufacturing/Computer Aided Engineering (CAD/CAM/CAE) in 1995. Then, he enrolled as a graduate student in the Mechanical Engineering Department at the University of Kansas where he later received his Master of Science in Mechanical Engineering majoring in Computational Solid Mechanics in 1999. In 1997, he transferred to North Carolina State University to begin his Ph.D. study in an area of computational mechanics applied to manufacturing processes with Dr. John S. Strenkowski. After receiving his Ph.D. degree, he plans to return to Kasetsart University in Thailand where he has been appointed as a lecturer in the Department of Mechanical Engineering since October 2001.

ACKNOWLEDGEMENTS

I am very grateful to Dr. John S. Strenkowski, the chairman of my Ph.D. advisory committee, for his invaluable support, guidance and endless encouragement since the beginning of my enrollment at North Carolina State University. It has been my honor to have an opportunity to work with him for a number of years. I consider myself to be very fortunate to have him serving as my advisor. I also would like to thank Dr. John A. Bailey, who taught me the fundamentals of machining and material deformation during my graduate study, Dr. John S. Stewart, who provided me an valuable advice in machining and partial financial assistance during my Ph.D. study, and Dr. Melur K. Ramasubramanian for his kindness to serve on the Ph.D. advisory committee. In addition, I would like to thank Dr. Albert J. Shih and Juan-Pablo Gallego for their valuable suggestions throughout the research work in the machining of elastomers.

I also owe gratitude to Dr. Karan Surana, Deane E. Ackers Distinguished Professor of Mechanical Engineering at the University of Kansas, who first introduced me to the world of the finite element method. In addition, I would like to thank Dr. Yi-Min Wei and Dr. Chang-Chi Hsieh, Dr. Xiangfu Wang, former graduate students in the Department of Mechanical and Aerospace Engineering at North Carolina State University, for their valuable discussions on the subject of the machining process. Appreciation is extended to Rufus (Skip) Richardson and Mike Breedlove for their assistance in preparation of cutting tools, specimens, and lathe setup. Special thanks are also given to my colleagues in the elastomer machining group: Jun Yan, Jie Luo, Perry E. Miller, Mark A. Lewis, and Darrin R. Poirier.

I gratefully acknowledge the financial support from the National Science Foundation as well as the industrial collaboration of Michelin Americas R&D Corporation and Lord Corporation. Additionally, my graduate study at North Carolina State University was made possible with partial funding from the Department of Mechanical and Aerospace Engineering, the Integrated Manufacturing Systems Engineering Institute (IMSEI), and the Wood Machining and Tooling Research Program (WMTRP) at North Carolina State University. Their courtesies are always greatly appreciated.

Finally, I would like to express my deep appreciation to my parents, and my dearest wife, Nussara Boonkungwan, for their unconditioned love, inspiration and support during an endless period of my graduate study in the United States. I hope that completion of my Ph.D. degree would bring them peace and true happiness.

TABLE OF CONTENTS

| | |
|---|-----------|
| LIST OF TABLES | ix |
| LIST OF FIGURES..... | x |
| LIST OF SYMBOLS | xix |
| | |
| 1. INTRODUCTION | 1 |
| 1.1 Scope and Objective of Dissertation | 4 |
| 1.2 Overview of Dissertation | 6 |
| | |
| 2. LITERATURE REVIEW | 7 |
| 2.1 General Description of Elastomers | 7 |
| 2.2 Analysis of the Strain Energy Function for Elastomers | 10 |
| 2.2.1 A Statistical Approach | 10 |
| 2.2.2 A Phenomenological Approach..... | 11 |
| 2.3 Analysis of a Wedge Indentation Process | 14 |
| 2.3.1 Wedge Indentation of Metals | 14 |
| 2.3.2 Wedge Indentation of Elastomers..... | 17 |
| 2.4 Analysis of a Machining Process | 19 |
| | |
| 3. ELASTOMER MACHINING EXPERIMENTS..... | 26 |
| 3.1 Introduction | 26 |
| 3.2 Experimental Setup | 26 |
| 3.3 Experimental Results and Discussions..... | 31 |
| | |
| 4. DESCRIPTION OF MODEL DEVELOPMENT | 46 |
| 4.1 A General Description of the ABAQUS Software..... | 46 |
| 4.1.1 ABAQUS/Standard | 48 |
| 4.1.2 ABAQUS/Explicit..... | 49 |
| 4.2 Finite Element Implicit and Explicit Time Integration | 50 |

TABLE OF CONTENTS (continued)

| | |
|---|-----------|
| 4.3 Contact and Interaction Concepts in Wedge Indentation and Orthogonal Cutting Models..... | 53 |
| 4.4 Description of Indentation and Orthogonal Cutting Models..... | 56 |
| 4.4.1 Modeling of Indentation of AISI 4340 Steel..... | 57 |
| 4.4.2 Modeling of Orthogonal Cutting of AISI 4340 Steel..... | 61 |
| 4.4.3 Modeling of Indentation of Elastomers..... | 67 |
| 4.4.4 Modeling of Orthogonal Cutting of Elastomers..... | 75 |
| 5. SIMULATIONS OF ORTHOGONAL CUTTING AND WEDGE | |
| INDENTATION..... | 80 |
| 5.1 Simulations of AISI 4340 Steel..... | 80 |
| 5.1.1 Orthogonal Cutting Simulation..... | 80 |
| 5.1.2 Wedge Indentation Simulation with a 70 degree Half-Wedge Angle.... | 87 |
| 5.2 Simulations of Indentation of Elastomers..... | 93 |
| 5.2.1 Wedge Indentation for a 80 degree Half-Wedge Indenter (Case 1)..... | 97 |
| 5.2.2 Wedge Indentation for a 40 degree Half-Wedge Indenter (Case 2)..... | 102 |
| 5.2.3 Wedge Indentation for a 40 degree Half-Wedge Indenter and Tip Edge Radius of 0.01270 mm (Case 3)..... | 110 |
| 5.2.4 Wedge Indentation for a 40 degree Half-Wedge Indenter for Feed of 0.2540 mm (Case 4)..... | 117 |
| 5.2.5 Wedge Indentation for a 40 degree Half-Wedge Indenter and a Friction Coefficient of 1.20 (Case 5)..... | 122 |
| 5.2.6 Wedge Indentation for a 40 degree Half-Wedge Indenter and Boundary Condition Type 2 (Case 6)..... | 127 |
| 5.3 Simulations of Orthogonal Cutting of Elastomers..... | 132 |

TABLE OF CONTENTS (continued)

| | |
|--|------------|
| 6. CONCLUSIONS AND FUTURE WORK..... | 140 |
| 6.1 Conclusions | 140 |
| 6.2 Future Work | 142 |
| REFERENCES..... | 144 |

LIST OF TABLES

| | |
|---|----|
| Table 2.1 Comparison of properties of elastomers with other materials | 9 |
| Table 4.1 A summary of the material properties of AISI 4340 steel..... | 60 |
| Table 4.2 Temperature-dependent thermal expansion coefficients for AISI 4340 steel. .. | 63 |
| Table 4.3 Temperature-dependent elastic properties of AISI 4340 steel..... | 63 |
| Table 4.4 Temperature-dependent elastic-plastic properties of AISI 4340 steel..... | 64 |
| Table 5.1 Summary of operating conditions used in wedge indentation simulations of elastomers.. .. | 94 |
| Table 5.2 Summary of operating conditions for evaluating various effects on elastomer machinability..... | 96 |

LIST OF FIGURES

| | |
|---|----|
| Figure 2.1 Comparison between orthogonal and oblique cutting..... | 20 |
| Figure 2.2 Nomenclature of orthogonal cutting..... | 20 |
| Figure 3.1 Fixture design and cutting tool setup for the elastomer machining experiments..... | 27 |
| Figure 3.2 Side view of workpiece in the lathe chuck for the elastomer machining experiments..... | 28 |
| Figure 3.3 Nomenclature of cutting tool angles..... | 29 |
| Figure 3.4 Chip types for various rake angles and feed speeds for a cutting speed of 2.50 m/s..... | 32 |
| Figure 3.5 Photographs of machined surfaces for a cutting speed of 2.50 m/s, three rake angles and two feed speeds..... | 33 |
| Figure 3.6 Typical measured machining forces in three axes (cutting, thrust, and transverse components) for a sharp cutting tool with a rake angle of 10 degrees, feed speed of 0.0635 mm, and cutting speed of 2.50 m/s..... | 35 |
| Figure 3.7 Typical measured machining forces in three axes (cutting, thrust, and transverse components) for a sharp cutting tool with a rake angle of 50 degrees, feed speed of 0.2540 mm, and cutting speed of 2.50 m/s..... | 35 |
| Figure 3.8 Measured force components for a sharp cutting tool with various tool rake angles, a feed speed of 0.0635 mm and a cutting speed of 2.50 m/s..... | 37 |
| Figure 3.9 Measured force components for a sharp cutting tool with various tool rake angles, a feed speed of 0.2540 mm and a cutting speed of 2.50 m/s..... | 37 |
| Figure 3.10 Comparison of measured cutting forces for cutting tools with various rake angles and feed speeds for a cutting speed of 2.50 m/s..... | 38 |
| Figure 3.11 Comparison of measured thrust forces for cutting tools with various rake angles and feed speeds for a cutting speed of 2.50 m/s..... | 38 |
| Figure 3.12 Apparatus for measuring the cutting edge sharpness..... | 39 |
| Figure 3.13 Schematic diagram to determine the tool edge radius..... | 40 |
| Figure 3.14 Unused tool edge with a nose width of 10 microns (10 degree rake angle, 5 degree clearance angle)..... | 43 |

LIST OF FIGURES (continued)

| | |
|--|----|
| Figure 3.15 Used tool edge with nose a width of 15 microns (10 degree rake angle, 5 degree clearance angle)..... | 43 |
| Figure 3.16 Unused tool edge with a nose width of 10 microns (30 degree rake angle, 5 degree clearance angle)..... | 44 |
| Figure 3.17 Used tool edge with nose a width of 15 microns (30 degree rake angle, 5 degree clearance angle)..... | 44 |
| Figure 3.18 Unused tool edge with a nose width of 10 microns (50 degree rake angle, 5 degree clearance angle)..... | 45 |
| Figure 3.19 Used tool edge with nose a width of 15 microns (50 degree rake angle, 5 degree clearance angle)..... | 45 |
| Figure 4.1 ABAQUS modules | 47 |
| Figure 4.2 Contact and interaction discretization | 54 |
| Figure 4.3 Initial mesh of a half-wedge indentation model of AISI 4340 steel..... | 58 |
| Figure 4.4 Initial mesh of a half-wedge indentation model of AISI 4340 steel (detailed view) | 58 |
| Figure 4.5 Initial mesh for the orthogonal cutting model of AISI 4340 steel..... | 62 |
| Figure 4.6 Initial mesh for half-wedge indentation model of elastomers | 68 |
| Figure 4.7 Initial mesh for half-wedge indentation model of elastomers (detailed view). | 68 |
| Figure 4.8 Uniaxial tensile stress-strain relationship for elastomer used in the wedge indentation model. | 69 |
| Figure 4.9 Schematic of the uniaxial deformation mode..... | 71 |
| Figure 4.10 Schematic of the equi-biaxial deformation mode..... | 71 |
| Figure 4.11 Schematic of the planar deformation mode..... | 71 |
| Figure 4.12 Initial mesh for the orthogonal cutting model of elastomers..... | 76 |
| Figure 4.13 Uniaxial tensile stress - extension ratio relationship used in orthogonal cutting model of elastomers..... | 78 |
| Figure 5.1 Undeformed and deformed configurations of the finite element mesh..... | 81 |

LIST OF FIGURES (continued)

| | |
|---|----|
| Figure 5.2 Von Mises stress contours (MPa) at early configuration (analysis step 3, increment 60) | 83 |
| Figure 5.3 Von Mises stress contours (MPa) at final configuration (analysis step 4, increment 6)..... | 83 |
| Figure 5.4 Tresca stress contours (MPa) at early configuration (analysis step 3, increment 60)..... | 84 |
| Figure 5.5 Tresca stress contours (MPa) at final configuration (analysis step 4, increment 6)..... | 84 |
| Figure 5.6 Normal stress contours (MPa) at early configuration (analysis step 2, increment 11)..... | 85 |
| Figure 5.7 Normal stress contours (MPa) at final configuration (analysis step 4, increment 6)..... | 85 |
| Figure 5.8 Strain energy density contours (MPa) at early configuration (analysis step 3, increment 60)..... | 86 |
| Figure 5.9 Strain energy density contours (MPa) at final configuration (analysis step 4, increment 6)..... | 86 |
| Figure 5.10 Undeformed configuration of the finite element mesh for a half-wedge indenter angle of 70 degrees | 87 |
| Figure 5.11 Von Mises stress contours (MPa) at an indentation depth of 0.02 mm for a half-wedge indenter angle of 70 degrees..... | 89 |
| Figure 5.12 Von Mises stress contours (MPa) at an indentation depth of 0.05 mm for a half-wedge indenter angle of 70 degrees..... | 89 |
| Figure 5.13 Tresca stress contours (MPa) at an indentation depth of 0.02 mm for a half-wedge indenter angle of 70 degrees..... | 90 |
| Figure 5.14 Tresca stress contours (MPa) at an indentation depth of 0.05 mm for a half-wedge indenter angle of 70 degrees..... | 90 |
| Figure 5.15 Tresca stress contours (MPa) within a plastic shear zone of 478 MPa at an indentation depth of 0.02 mm for a half-wedge indenter angle of 70 degrees..... | 91 |

LIST OF FIGURES (continued)

| | |
|---|-----|
| Figure 5.16 Tresca stress contours (MPa) within a plastic shear zone of 478 MPa at an indentation depth of 0.05 mm for a half-wedge indenter angle of 70 degrees..... | 91 |
| Figure 5.17 Strain energy density contours (MPa) at an indentation depth of 0.02 mm for a half-wedge indenter angle of 70 degrees..... | 92 |
| Figure 5.18 Strain energy density contours (MPa) at an indentation depth of 0.05 mm for a half-wedge indenter angle of 70 degrees..... | 92 |
| Figure 5.19 Deformed and undeformed configurations of the finite element mesh for a half-wedge angle of 80 degrees, tip edge radius of 0.00635 mm, feed of 0.0635 mm, friction coefficient of 0.60, and indentation depth of 0.10 mm..... | 97 |
| Figure 5.20 Tresca stress contours (MPa) for a half-wedge angle of 80 degrees, tip edge radius of 0.00635 mm, feed of 0.0635 mm, friction coefficient of 0.60, and indentation depth of 0.10 mm..... | 99 |
| Figure 5.21 Detailed view of Tresca stress contours (MPa) for a half-wedge angle of 80 degrees, tip edge radius of 0.00635 mm, feed of 0.0635 mm, friction coefficient of 0.60, and indentation depth of 0.10 mm..... | 99 |
| Figure 5.22 Normal stress contours (MPa) for a half-wedge angle of 80 degrees, tip edge radius of 0.00635 mm, feed of 0.0635 mm, friction coefficient of 0.60, and indentation depth of 0.10 mm..... | 100 |
| Figure 5.23 Detailed view of normal stress contours (MPa) for a half-wedge angle of 80 degrees, tip edge radius of 0.00635 mm, feed of 0.0635 mm, friction coefficient of 0.60, and indentation depth of 0.10 mm..... | 100 |
| Figure 5.24 Detailed view of maximum principal stress contours (MPa) for a half-wedge angle of 80 degrees, tip edge radius of 0.00635 mm, feed of 0.0635 mm, friction coefficient of 0.60, and indentation depth of 0.10 mm..... | 101 |
| Figure 5.25 Detailed view of strain energy density contours (MPa) for a half-wedge angle of 80 degrees, tip edge radius of 0.00635 mm, feed of 0.0635 mm, friction coefficient of 0.60, and indentation depth of 0.10 mm..... | 101 |

LIST OF FIGURES (continued)

| | |
|---|-----|
| Figure 5.26 Deformed and undeformed configurations of the finite element mesh for a half-wedge angle of 40 degrees, tip edge radius of 0.00635 mm, feed of 0.0635 mm, friction coefficient of 0.60, and indentation depth of 0.10 mm..... | 102 |
| Figure 5.27 Tresca stress contours (MPa) for a half-wedge angle of 40 degrees, tip edge radius of 0.00635 mm, feed of 0.0635 mm, friction coefficient of 0.60, and indentation depth of 0.10 mm.. | 104 |
| Figure 5.28 Detailed view of Tresca stress contours (MPa) for a half-wedge angle of 40 degrees, tip edge radius of 0.00635 mm, feed of 0.0635 mm, friction coefficient of 0.60, and indentation depth of 0.10 mm..... | 104 |
| Figure 5.29 Normal stress contours (MPa) for a half-wedge angle of 40 degrees, tip edge radius of 0.00635 mm, feed of 0.0635 mm, friction coefficient of 0.60, and indentation depth of 0.10 mm.. | 105 |
| Figure 5.30 Detailed view of normal stress contours (MPa) for a half-wedge angle of 40 degrees, tip edge radius of 0.00635 mm, feed of 0.0635 mm, friction coefficient of 0.60, and indentation depth of 0.10 mm..... | 105 |
| Figure 5.31 Detailed viewed of maximum principal stress contours (MPa) for a half-wedge angle of 40 degrees, tip edge radius of 0.00635 mm, feed of 0.0635 mm, friction coefficient of 0.60, and indentation depth of 0.10 m | 106 |
| Figure 5.32 Detailed view of strain energy density contours (MPa) for a half-wedge angle of 40 degrees, tip edge radius of 0.00635 mm, feed of 0.0635 mm, friction coefficient of 0.60, and indentation depth of 0.10 mm..... | 106 |
| Figure 5.33 Normal stress of the elastomeric workpiece area under the indenter tip for a tip edge radius of 0.00635 mm, feed of 0.0635 mm, and friction coefficient of 0.60 with various half-wedge angles.. | 108 |
| Figure 5.34 Maximum principal stress of the elastomeric workpiece area under the indenter tip for a tip edge radius of 0.00635 mm, feed of 0.0635 mm, and friction coefficient of 0.60 with various half-wedge angles | 108 |

LIST OF FIGURES (continued)

| | |
|--|-----|
| Figure 5.35 Strain energy density of the elastomeric workpiece area under the indenter tip for a tip edge radius of 0.00635 mm, feed of 0.0635 mm, and friction coefficient of 0.60 with various half-wedge angles | 109 |
| Figure 5.36 Deformed and undeformed configurations of the finite element mesh for a half-wedge angle of 40 degrees, tip edge radius of 0.01270 mm, feed of 0.0635 mm, friction coefficient of 0.60, and indentation depth of 0.10 mm..... | 110 |
| Figure 5.37 Normal stress contours (MPa) for a half-wedge angle of 40 degrees, tip edge radius of 0.01270 mm, feed of 0.0635 mm, friction coefficient of 0.60, and indentation depth of 0.10 mm... .. | 112 |
| Figure 5.38 Detailed view of normal stress contours (MPa) for a half-wedge angle of 40 degrees, tip edge radius of 0.01270 mm, feed of 0.0635 mm, friction coefficient of 0.60, and indentation depth of 0.10 mm..... | 112 |
| Figure 5.39 Detailed view of maximum principal stress contours (MPa) for a half-wedge angle of 40 degrees, tip edge radius of 0.01270 mm, feed of 0.0635 mm, friction coefficient of 0.60, and indentation depth of 0.10 mm. | 113 |
| Figure 5.40 Detailed view of strain energy density contours (MPa) for a half-wedge angle of 40 degrees, tip edge radius of 0.01270 mm, feed of 0.0635 mm, friction coefficient of 0.60, and indentation depth of 0.10 mm..... | 113 |
| Figure 5.41 Normal stress of the elastomeric workpiece area under the indenter tip for a tip edge radius of 0.01270 mm, feed of 0.0635 mm, and friction coefficient of 0.60 with various half-wedge angles | 115 |
| Figure 5.42 Strain energy density of the elastomeric workpiece area under the indenter tip for a tip edge radius of 0.01270 mm, feed of 0.0635 mm, and friction coefficient of 0.60 with various half-wedge angles..... | 115 |
| Figure 5.43 Effect of indenter tip edge radius on the strain energy density and maximum principal stress of the elastomeric workpiece area under feed of 0.0635 mm, and friction coefficient of 0.60 for various half-wedge angles at 10 mm indentation depth..... | 116 |

LIST OF FIGURES (continued)

| | |
|---|-----|
| Figure 5.44 Deformed and undeformed configurations of the finite element mesh for a half-wedge angle of 40 degrees, tip edge radius of 0.00635 mm, feed of 0.2540 mm, friction coefficient of 0.60, and indentation depth of 0.10 mm..... | 117 |
| Figure 5.45 Normal stress contours (MPa) for a half-wedge angle of 40 degrees, tip edge radius of 0.00635 mm, feed of 0.2540 mm, friction coefficient of 0.60, and indentation depth of 0.10 mm | 119 |
| Figure 5.46 Detailed view of normal stress contours (MPa) for a half-wedge angle of 40 degrees, tip edge radius of 0.00635 mm, feed of 0.2540 mm, friction coefficient of 0.60, and indentation depth of 0.10 mm..... | 110 |
| Figure 5.47 Detailed view of maximum principal stress contours (MPa) for a half-wedge angle of 40 degrees, tip edge radius of 0.00635 mm, feed of 0.2540 mm, friction coefficient of 0.60, and indentation depth of 0.10 mm | 120 |
| Figure 5.48 Detailed view of strain energy density contours (MPa) for a half-wedge angle of 40 degrees, tip edge radius of 0.00635 mm, feed of 0.2540 mm, friction coefficient of 0.60, and indentation depth of 0.10 mm.. | 120 |
| Figure 5.49 Effect of indentation feed on the strain energy density and maximum principal stress of the elastomer workpiece area under an indenter tip for a tip edge radius of 0.00635 mm, and friction coefficient of 0.60 for various half-wedge angles at 10 mm indentation depth.. | 121 |
| Figure 5.50 Deformed and undeformed configurations of the finite element mesh for a half-wedge angle of 40 degrees, tip edge radius of 0.00635 mm, feed of 0.0635 mm, friction coefficient of 1.20, and indentation depth of 0.10 mm..... | 122 |
| Figure 5.51 Normal stress contours (MPa) for a half-wedge angle of 40 degrees, tip edge radius of 0.00635 mm, feed of 0.0635 mm, friction coefficient of 1.20, and indentation depth of 0.10 mm | 124 |
| Figure 5.52 Detailed view of normal stress contours (MPa) for a half-wedge angle of 40 degrees, tip edge radius of 0.00635 mm, feed of 0.0635 mm, friction coefficient of 1.20, and indentation depth of 0.10 mm..... | 124 |

LIST OF FIGURES (continued)

| | |
|--|-----|
| Figure 5.53 Detailed view of maximum principal stress contours (MPa) for a half-wedge angle of 40 degrees, tip edge radius of 0.00635 mm, feed of 0.0635 mm, friction coefficient of 1.20, and indentation depth of 0.10 mm | 125 |
| Figure 5.54 Detailed view of strain energy density contours (MPa) for a half-wedge angle of 40 degrees, tip edge radius of 0.00635 mm, feed of 0.0635 mm, friction coefficient of 1.20, and indentation depth of 0.10 mm..... | 125 |
| Figure 5.55 Effect of friction on workpiece/indenter interface on the strain energy density and maximum principal stress of the elastomeric workpiece area under the indenter tip for a tip edge radius of 0.00635 mm, and feed of 0.0635 mm for various half-wedge angles at 10 mm indentation depth..... | 126 |
| Figure 5.56 Deformed and undeformed configurations of the finite element mesh for a half-wedge angle of 40 degrees, tip edge radius of 0.00635 mm, feed of 0.0635 mm, friction coefficient of 0.60, indentation depth of 0.10 mm and a boundary condition Type 2..... | 127 |
| Figure 5.57 Normal stress contours (MPa) for a half-wedge angle of 40 degrees, tip edge radius of 0.00635 mm, feed of 0.0635 mm, friction coefficient of 0.60, indentation depth of 0.10 mm and a boundary condition Type 2..... | 129 |
| Figure 5.58 Detailed view of normal stress contours (MPa) for a half-wedge angle of 40 degrees, tip edge radius of 0.00635 mm, feed of 0.0635 mm, friction coefficient of 0.60, indentation depth of 0.10 mm and a boundary condition Type 2..... | 129 |
| Figure 5.59 Detailed view of maximum principal stress contours (MPa) for a half-wedge angle of 40 degrees, tip edge radius of 0.00635 mm, feed of 0.0635 mm, friction coefficient of 0.60, indentation depth of 0.10 mm and a boundary condition Type 2 | 130 |
| Figure 5.60 Detailed view of strain energy density contours (MPa) for a half-wedge angle of 40 degrees, tip edge radius of 0.00635 mm, feed of 0.0635 mm, friction coefficient of 0.60, indentation depth of 0.10 mm and a boundary condition Type 2..... | 130 |

LIST OF FIGURES (continued)

| | |
|---|-----|
| Figure 5.61 Effect of fixture design of the workpiece on the strain energy density and maximum principal stress of the elastomeric workpiece area under the indenter tip for a half-wedge angle of 40 degrees, tip edge radius of 0.00635 mm, feed of 0.0635 mm, friction coefficient of 0.60, and indentation depth of 0.10 mm for various half-wedge angles at 10 mm indentation depth..... | 131 |
| Figure 5.62 Undeformed and deformed configurations of the finite element mesh..... | 133 |
| Figure 5.63 Von Mises stress contours (MPa) at the analysis step 3, increment 33..... | 135 |
| Figure 5.64 Von Mises stress contours (MPa) at the analysis step 3, increment 33 (detailed view)..... | 135 |
| Figure 5.65 Tresca stress contours (MPa) at the analysis step 3, increment 33.. | 136 |
| Figure 5.66 Tresca stress contours (MPa) at the analysis step 3, increment 33 (detailed view)..... | 136 |
| Figure 5.67 Normal stress contours (MPa) at the analysis step 3, increment 33..... | 137 |
| Figure 5.68 Normal stress contours (MPa) at the analysis step 3, increment 33 (detailed view)..... | 137 |
| Figure 5.69 Maximum principal stress contours (MPa) at the analysis step 3, increment 33..... | 138 |
| Figure 5.70 Maximum principal stress contours (MPa) at the analysis step 3, increment 33 (detailed view)..... | 138 |
| Figure 5.71 Strain energy density contours (MPa) at the analysis step 3, increment 33.. | 139 |
| Figure 5.72 Strain energy density contours (MPa) at the analysis step 3, increment 33 (detailed view)..... | 139 |

LIST OF SYMBOLS

| | |
|-----------------------------------|---|
| W | Strain energy density or free energy per unit volume |
| $\lambda_1, \lambda_2, \lambda_3$ | Principal stretch ratios along three perpendicular axes |
| N | Number of chains per unit volume |
| k | Boltzmann constant |
| T | Absolute temperature |
| G | Shear modulus or modulus of rigidity |
| C_1, C_2, C_3 | Material constants obtained from experiment |
| I_1, I_2, I_3 | Strain invariants |
| α_k | A real number |
| m | A positive integer |
| μ_k, α_k | Materials constants obtained from experiment |
| A | Area of one fracture surface of a crack |
| T_c | Critical tearing energy |
| $[M]$ | Mass matrix |
| $[C]$ | Stiffness matrix |
| $[K]$ | Damping matrix |
| \ddot{u}_{n+1} | Nodal accelerations |
| \dot{u}_{n+1} | Nodal velocities |
| u_{n+1} | Nodal displacements |
| F_{n+1}^a | Applied force at time $n+1$ |

LIST OF SYMBOLS (continued)

| | |
|--------------------|--|
| Δt | Time step |
| $\dot{\epsilon}_p$ | Effective plastic strain rate |
| σ_{ef} | Effective yield stress |
| σ_Y | Initial yield stress |
| D, p | Material constants based on empirical strain rate sensitivity |
| F | Deformation gradient |
| ϵ_i | Principal nominal strains |
| λ_i | Principal stretches |
| λ_U | Stretch in the loading direction |
| T_U | Uniaxial nominal stress |
| T_B | Equi-biaxial nominal stress |
| T_S | Nominal planar stress |
| τ_c | Critical shear stress of the chip along the chip/tool interface |
| μ | Friction coefficient |
| τ_{th} | Threshold stress related to material failure |
| p | Normal pressure at a contact point along the chip/tool interface |
| f | Critical shear function |
| σ_n | Normal tensile stress measured at a specific distance |

LIST OF SYMBOLS (continued)

| | |
|------------|--|
| σ_f | Material failure stress under tensile mode |
| τ_n | Measure shear stress measured at a specific distance |
| τ_f | Material failure stress under shear mode |
| \hat{A} | Included angle of cutting tool |

1. INTRODUCTION

Elastomers are widely used in various industries for tires, springs, shock isolators, noise and vibration absorbers, seals, corrosion and abrasion protection, and electrical and thermal insulators. Among elastomeric materials, rubber is the most well known elastomer. Rubber has been used as an engineering material since the mid 1800's (Charlton and Yang, 1994).

Some of the unique properties that make elastomers different from other conventional materials such as metals include the following:

1. Elastomers exhibit a highly non-linear stress-strain relationship as compared to metals.
2. Elastomers are able recover to an undeformed state after large deformation upon removal of the load.
3. Elastomers have no yield point in the stress-strain curve and they are highly non-linear at large strains. The elastic modulus and tensile strength of elastomers are also low compared to metals.
4. Elastomers have good fatigue resistance and high energy absorption capacity due to their high elasticity.
5. The material properties of elastomers change significantly with temperature variation.
6. Poisson's ratio of elastomers is very close to 0.50 (nearly incompressible).
7. The coefficient of friction for elastomer surfaces is relatively high compared with a metal to metal interface.
8. Elastomers are flexible, strong, leakproof, and resistant to corrosion.

9. The moldability of elastomers allows for their use in a wide range of applications such as hoses, belts, tubes, engine mounts, wiper blades, footwear, toys, and tires.

In comparison with metals, elastomers are complex because both their material and geometric behavior is non-linear. Elastomers are isotropic, highly deformable, highly elastic, and nearly incompressible. They are also hyperelastic or Green elastic, i.e., their mechanical properties can be characterized by means of a strain energy function. Elastomers have high elongation before fracture and a very low elastic modulus and relatively low thermal conductivity. In addition, the mechanical properties of elastomers are highly sensitive to strain, strain rate, strain history, temperature, composition, and manufacturing methods.

Most elastomeric parts are produced by a molding process in which a composition of raw materials and additional additives are subjected to a controlled temperature-pressure-cycle to produce the desired properties and geometry. Some elastomer applications such as tire or shoe tread patterns require a complex mold to be manufactured. The disadvantage of this method is the high cost and time-consuming process of manufacturing the mold. As an alternative, elastomer machining is proposed in this research to reduce production costs by eliminating the molding process, which would be especially useful for manufacturing prototype parts and other applications requiring a complex shape. Potential applications of machined elastomers include prototype tire and footwear tread patterns, scrap tire recycling, and specialty vibration dampers.

With the rapid advancement of computational power, numerical techniques have been developed to analyze complex engineering problems. Among available numerical methods, the Finite Element Method (FEM) is considered to be one of the most powerful, accurate and reliable computational tools. The FEM has been used extensively to analyze manufacturing processes such as machining and forming of more traditional engineering metallic materials such as steel and aluminum alloys (Strenkowski and Carroll, 1985), (Strenkowski and Moon, 1990), (Strenkowski and Lin, 1996), (Shih, 1995), (Shih, 1996). However, very little research has been undertaken to investigate the machining and chip formation process of elastomers with the finite element method.

The roughness of a machined elastomer surface is highly dependent on the type of chip produced during machining. Discontinuous chip formation is associated with a rough surface finish of the workpiece, which results in inaccuracy in the final machined workpiece dimensions. In this research, wedge indentation was investigated because indentation can be considered to be the incipient stage of chip formation in a machining process.

Very little research on elastomer machining has been performed because of the complexity of elastomers and the machining process itself. In this research, better understanding of machining of elastomers was achieved through the development of wedge indentation models and orthogonal cutting tests. The wedge indentation models were used to investigate chip formation during incipient metal cutting prior to material separation. Even though wedge indentation does not incorporate chip formation, it can lead to a better understanding of the behavior of elastomers during the initial stages of cutting.

1.1 Scope and Objective of Dissertation

The main objective of this research is to gain a better understanding of the machining conditions that result in improved machinability of elastomers. A series of half-wedge indentation models were developed and orthogonal cutting tests were conducted to achieve this objective. Simulations of half-wedge indentation in elastomers were conducted to identify machining conditions that lead to continuous chip formation and good surface finish. These results were confirmed with orthogonal cutting tests for tools with various rake angles under different feed speed conditions.

The following tasks were undertaken in this research:

1. An extensive literature review of wedge indentation and machining of elastomers was conducted. The material characteristics of elastomers and the associated constitutive equations were reviewed. The mechanics of machining for both metals and elastomers was also reviewed, as well as the use of the finite element method for simulating indentation and machining processes.
2. A series of orthogonal machining experiments of elastomers was conducted using a conventional lathe under various cutting conditions. The resulting chip morphology and machined surface finish were observed and recorded and the resulting forces were measured.

3. The effect of various machining parameters such as workpiece fixturing, tool rake angle, and feed speed on the generated chip geometry and machined surface quality of the elastomeric workpiece was investigated. These results provided useful information for identifying machining conditions that lead to continuous chip formation and a smooth surface finish.

4. Two-dimensional finite element models of half-wedge indentation of elastomers were developed using ABAQUS, a commercial finite element analysis program. These models were used to identify the initial stage of material separation which subsequently leads to incipient chip formation in machining. These models were used to characterize the workpiece material response for ultimately identifying the cutting conditions for which indentation transitions to cutting and chip formation. A preliminary model of elastomer cutting was also developed.

1.2 Overview of Dissertation

The following chapter presents a literature review of the material characteristics of elastomers and the associated constitutive equations. The review also includes past research regarding the indentation of metals and elastomers and the mechanics of the machining process. Background on the use of the finite element method for simulating cutting processes is also described. In Chapter 3, orthogonal cutting tests for an elastomer are described. The chip morphology and corresponding machining forces under various cutting conditions are discussed. The effects of various machining parameters such as the tool rake angle and feed speed on the machined surface finish are also examined in this chapter. Chapter 4 discusses the development of half-wedge indentation models for elastomers. For comparison, wedge indentation and orthogonal cutting models for AISI 4340 steel are also described. Background on the use of the non-linear finite element technique is given for simulating the indentation of elastomers. Results from the elastomer half-wedge indentation and metal cutting models are discussed in Chapter 5. Preliminary results of an elastomer orthogonal cutting simulation are also presented. Conclusions and recommendations for future work are given in Chapter 6.

2. LITERATURE REVIEW

2.1 General Description of Elastomers

An elastomer can be defined as, “a macromolecular material, which, at room temperature, is capable of recovering substantially in shape and size after removal of a deforming force.” (ASTM, 1999). Rubber is also defined by the same standard as “a material that is capable of recovering from large deformations quickly and forcibly and can be, or already modified to a state in which it is essentially insoluble (but can swell) in boiling solvent, such as benzene, methyl ethylketone, or ethanol-toluene azeotrope. A rubber in its modified state, free of diluents, retracts within one minute to less than 1.5 times its original length after being stretched at room temperature to twice its length and held for one minute before release.” Therefore, it is noted that all rubbers are elastomers; however, not all elastomers are rubbers. Some types of plastics can be also considered to be elastomers, according to this definition.

Among a variety of plants containing rubber, the rubber tropical trees (*Hevea brasiliensis*) growing mainly in Southeast Asia and Africa are the major source employed for commercial rubber. Nevertheless, any synthetic material such as neoprene, nitrile, and styrene butadiene are categorized with natural rubbers since their characteristics can be classified as rubbers (Shalaby and Schwartz, 1985).

The high elasticity of elastomers that allows for large elastic deformation is certainly one of the most remarkable characteristics. Elastomers have a very low elastic modulus and a high percent of elongation before fracture. Under cyclic loading, elastomers exhibit significant

hysteresis, which contributes to their energy absorption capability. A crosslinked strip, extended to many times of its original length when released, will return to that original length showing very little or no permanent deformation as a result of the extension. This is in contrast to the behavior of ductile metals that can undergo large deformation without fracture but do not return to their original shape upon removal of the load (Aklonis, MacKnight et al., 1972).

The deformation of elastomers can be considered to be non-linear in terms of both their material and geometric behavior. Elastomers are isotropic, highly deformable, highly elastic, nearly incompressible, hyperelastic or Green elastic, i.e., their mechanical properties can be characterized by means of a strain energy function (Ogden, 1997). In addition, the mechanical behavior of elastomers is very complex due to their sensitivity to strain, strain-rate, deformation history, temperature, and the fabrication process. Table 2.1 illustrates a comparison of the mechanical and thermal properties of elastomers with other materials.

Table 2.1 Comparison of properties of elastomers with other materials (Strenkowski, Shih et al., 2002).

| Material | Modulus of Elasticity (GPa) | Poisson's ratio | Ultimate stress (MPa) | % of elongation to fracture | Thermal conductivity (W/m K) |
|-----------------------|-----------------------------|-----------------|-----------------------|-----------------------------|------------------------------|
| Elastomers | 0.0007 – 0.004 | 0.47 – 0.5 | 7 – 20 | 100 – 800 | 0.13 – 0.16 |
| Aluminum alloy | 70 – 79 | 0.33 | 100 – 550 | 1 – 45 | 177 – 237 |
| Steel, high-strength | 190 – 210 | 0.27 – 0.3 | 550 – 1200 | 5 – 25 | 35 – 60 |
| Steel, spring | 190 – 210 | 0.27 – 0.3 | 700 – 1900 | 3 – 15 | 40 – 50 |
| Plastic, Nylon | 2.1 – 3.4 | 0.4 | 40 – 80 | 20 – 100 | 0.3 |
| Plastic, Polyethylene | 0.7 – 1.4 | 0.4 | 7 – 28 | 15 – 300 | 0.4 |

Note that the modulus of elasticity, the ultimate stress and the thermal conductivity of elastomers are very low compared to most metals. The Poisson's ratio of elastomers reaches 0.5 due to its incompressibility.

The deformation of rubbers began to receive serious attention from engineers and scientists in the 1940's. Rivlin was one of the leading researchers who worked with the British Rubber Producers' Association. His major contribution included an introduction of the theory of finite elastic strain or hyperelasticity as applied to rubber. Subsequently, several other researchers including Ogden, Valanis, and Yeoh developed various constitutive relationships for rubber materials.

In general, the elasticity of elastomers can be studied in three categories; namely, a thermodynamic approach, a statistical approach and a phenomenological treatment. The first thermodynamic treatment is only concerned with the macroscopic behavior of the material, rather than the molecular behavior. The second approach considers statistical mechanics that

underlie elastomeric molecular dynamics. The phenomenological approach, which is widely used today, provides a description of the elasticity for large deformation. As its name implies, the phenomenological approach is concerned only with observed behavior, not with the mechanism responsible for that behavior. Its primary aim is to provide a means of calculating the relationships between the state of strain in a deformed body and the applied forces. A secondary aim is to find a general description of material properties in terms of the elastic energy stored in the system (Treloar, 1958), (Aklonis, MacKnight et al., 1972). The elastic energy stored after the deformation in a system is a unique state function of strain and it is independent of the strain path. The state of strain is defined by three principal stretch ratios, denoted by λ_1 , λ_2 , and λ_3 (Ogden, 1997). The strain energy function used in the statistical and phenomenological approaches is discussed in the following section.

2.2 Analysis of the Strain Energy Function for Elastomers

2.2.1 A Statistical Approach

The statistical approach is based on the concept that vulcanized rubber is an assembly of long-chain molecules, linked together with a relatively small number of points to form an irregular three-dimensional network. Under the assumption that there is no change in the internal energy of the system during deformation, the free energy per unit volume or the strain energy density (W) can be written in the form (Treloar, 1958):

$$W = \frac{1}{2} NkT (\lambda_1^2 + \lambda_2^2 + \lambda_3^2 - 3) \quad (2.1)$$

Where $\lambda_1, \lambda_2, \lambda_3$ are the extension ratios along three mutually perpendicular axes, N is the number of chains per unit volume, k is the Boltzmann constant, and T is the absolute temperature. It is more convenient in practice to write (2.1) as:

$$W = \frac{1}{2} G (\lambda_1^2 + \lambda_2^2 + \lambda_3^2 - 3) \quad (2.2)$$

Where G is the shear modulus or modulus of rigidity, and $G = NkT$. This relation is also referred as the Neo-Hookean function.

2.2.2 A Phenomenological Approach

Based on the assumption that rubber is isotropic and incompressible, Mooney developed an expression of the strain energy function as (Mooney, 1940):

$$W = C_1 (\lambda_1^2 + \lambda_2^2 + \lambda_3^2 - 3) + C_2 (\lambda_1^{-2} + \lambda_2^{-2} + \lambda_3^{-2} - 3) \quad (2.3)$$

Where C_1 and C_2 are material constants that are experimentally determined.

Rivlin introduced an expression of all possible forms of the stored energy, W , for isotropic and incompressible materials, as a function of three quantities, I_1, I_2 , and I_3 called strain invariants which can be defined as (Rivin, 1948):

$$I_1 = \lambda_1^2 + \lambda_2^2 + \lambda_3^2 \quad (2.4)$$

$$I_2 = \lambda_1^2 \lambda_2^2 + \lambda_2^2 \lambda_3^2 + \lambda_3^2 \lambda_1^2 \quad (2.5)$$

$$I_3 = \lambda_1^2 \lambda_2^2 \lambda_3^2 \quad (2.6)$$

The assumption of incompressibility, i.e. the volume of material is constant in all states of stress, provides the relation:

$$I_3 = \lambda_1^2 \lambda_2^2 \lambda_3^2 = 1 \quad (2.7)$$

Therefore, I_3 , is not a function of strain, and it can be concluded that, for an incompressible elastic material which is isotropic, the stored energy, W , is defined as a function of two independent variables, I_1 and I_2 and it may be expressed as the sum of a series of terms as follows:

$$W = \sum_{i=0, j=0}^{\infty} C_{ij} (I_1 - 3)^i (I_2 - 3)^j \quad (2.8)$$

This equation is called the Rivlin function in general form. Note that this expression is arbitrarily written in terms of I_1 and I_2 so that W vanishes at zero strain ($I_1 = I_2 = 3$) by means of equations (2.4) – (2.5).

It can also be seen that the Mooney strain energy function in (2.3) is a special case of equation (2.8) where the first order relationship of the Rivlin function is considered, and it can be rewritten as:

$$W = C_1 (I_1 - 3) + C_2 (I_2 - 3) \quad (2.9)$$

This equation is referred as the Mooney-Rivlin strain energy function.

Yeoh also defined the strain energy function in the form of (Yeoh, 1993):

$$W = C_1 (I_1 - 3) + C_2 (I_1 - 3)^2 + C_3 (I_1 - 3)^3 \quad (2.10)$$

Valanis and Landel proposed another model which describes the strain energy function as the sum of three separate functions of the three principal stretch ratios as (Valanis and Landel, 1967):

$$W = w(\lambda_1) + w(\lambda_2) + w(\lambda_3) \quad (2.11)$$

Among the forms of the function $w(\lambda_i)$, the Ogden-Tschoegl model (Ogden, 1997), (Blatz, Sharda et al., 1974) is one of the most widely used today. It is defined as:

$$W = \sum_{k=1}^m \mu_k (\lambda_1^{\alpha_k} + \lambda_2^{\alpha_k} + \lambda_3^{\alpha_k} - 3) / \alpha_k \quad (2.12)$$

where α_k ($k = 1, \dots, m$) is a real number and m is a positive integer. Both μ_k and α_k are empirical material constants. Note that when $m = 2$, $\alpha_k = \pm 2$, and $\mu_1 = \pm 2C_k$, $k = 1, 2$, the strain energy function in equation (2.12) becomes the Mooney-Rivlin strain energy function shown in equation (2.9). When $m = 1$, $\alpha_1 = 2$, and $\mu_1 = G$, the strain energy function becomes the Neo-Hookean function shown in equation (2.2).

The Ogden-Tschoegl model has been applied to various tests. For simple tension using a 3-term function, it can describe a strain range up to 700% with small deviation compared to only 150% for the Mooney-Rivlin model (Ogden, 1997).

2.3 Analysis of a Wedge Indentation Process

The machining of metals has been successfully studied as a transition from wedge indentation. The mechanism of material separation in wedge indentation leads to incipient chip formation in metal cutting. Therefore, a review of wedge indentation of metals is given next. In addition, previous research in wedge indentation of elastomers was also surveyed.

2.3.1 Wedge Indentation of Metals

In general, plasticity solutions of wedge indentation of metals are classified into two categories (Lockett, 1963). The first category is incipient deformation. A body is subjected to a given set of boundary conditions and then the initial stress and velocity fields are calculated. Due to the time dependence of loading and boundary conditions, such solutions are only applied immediately after load application. An example of work in this category was conducted by Shield (Shield, 1955). In this work, the indentation of a semi-finite body by a rigid circular flat punch was analyzed to obtain the stress fields.

The second category is a class of problems for which plane strain conditions are assumed and the slip-line field is constructed from basic elements involving straight lines and arcs. As a result, the analytical solutions for the stress and velocity fields can be found. A theoretical solution for the deformation caused by a rigid lubricated wedge indentation of a plastic metallic material (Hill, Lee et al., 1947) was developed using this method. In this study, the metal was considered to have a distinct yield point and the rate of work-hardening was neglected. The effect of specimen size in the measurement of a hardness test using flat dies and wedges with various angles was also investigated (Hill, 1950). Hill also studied the use

of wedge indentation as a precursor to cutting. In this work, a flat strip of metal was cut in two parts using a wedged-shaped cutting tool (Hill, 1953). The width/thickness ratio of the strip was large enough so that the deformation could be treated as plane strain. As the strip was indented, the plastic zone extended to the base until the sideways force exerted by the wedge reached a value such that a plastic zone formed through the remaining thickness of material. As a result, separation of the material was initiated.

The cutting of round wires of copper and steel with flat and wedge-shaped tools has also been carried out (Johnson, 1958). Plane strain conditions were assumed in this work. Load-displacement relationships were determined. The effects of wire diameter and wedge angle on the maximum cutting required load were also determined.

Slip line theory has been used to analyze the indentation of a sharp edge punch to determine the mechanism of chip formation during incipient cutting with a negative rake angle tool (Okushima and Hitomi, 1963). Good correlation between developed expressions of tool/chip contact length, chip thickness, and cutting forces with experimental measurements was obtained

A study of incipient chip formation during orthogonal cutting of brass was carried out (Weinmann and Von Turkovich, 1971). Various cutting tools with negative, zero and positive degree rake angles were studied. A hardness and recrystallization investigation revealed that a maximum shear zone originated from the cutting edge vicinity and extended towards the free edge ahead of the cutting tool. Later, the effects of wedge geometry (half-

wedge and full-wedge configurations) and distance between the indentation point and the free edge were included in the study (Weinmann, 1977).

Wedge indentation of brass was also used to evaluate the chip separation criterion for incipient cutting (Strenkowski and Mitchum, 1987). In this work, the beginning of incipient cutting was determined to occur when the effective stress contour of the yield zone extended completely from the tool edge to the outside edge of the workpiece. At this point, the effective strain at the node adjacent to the tool edge was identified as a separation criterion for subsequent chip formation.

Using the finite element method, Bhattacharya and Nix simulated the load-depth relationship of a sub-micrometer indentation test for nickel, silicon, and aluminum with a rigid cone indenter (Bhattacharya and Nix, 1988). The hardness and the elastic modulus were obtained from the loading and unloading portions of the curve. Later, simulation of a frictionless wedge indenting a copper strip under plane strain conditions was presented (Jayadevan and Narasimhan, 1995).

Simulation of wedge indentation with various cone angles was also carried out to determine the stress-strain relationships of nickel and copper through a semi-inverse method (Dicarlo, Yang et al., 2002). In this investigation, power law hardening and the ratios of yield strength to Young's modulus were included in a finite element model of the indentation process. Results from the model were used to correlate the material properties with variations in indentation hardness for various cone angles. A comprehensive bibliography of the

application of both the finite element and boundary element methods for simulating the indentation process can be found in a paper published by Mackerle (Mackerle, 2001).

2.3.2 Wedge Indentation of Elastomers

The indentation of thin rubber sheets with various thicknesses by a rigid cylindrical indenter was carried out by Waters (Waters, 1965). Using a classical elasticity solution, relationships of the total load applied on a die, a die radius, and a sheet thickness were established. An analysis of a durometer indentation of elastomers was carried out (Briscoe and Sebastian, 1993). The theory of elasticity was used to derive relationships between the Shore hardness number and Young's modulus. A comparison of the standard indentation hardness test procedures, namely, International Rubber Hardness (IRH) and the Shore A Hardness with the corresponding elastic modulus was also developed.

Rubber indentation with various indenter geometries such as a cone, sphere, cylinder, has been examined (Briscoe, Sebastian et al., 1994). The influence of the indenter geometry on the elastic modulus of rubber was also investigated in this work. The effects of the indenter size, depth, specimen size, and rubber material properties have also been studied both empirically and numerically (Karduna, Halperin et al., 1997).

The finite element technique with adaptive meshing was employed for plain strain indentation of a nitrile rubber block using a rigid cylindrical indenter. In addition, uniaxial

tensile tests have been performed to determine material parameters used in the Mooney-Rivlin, Yeoh, and Ogden material models (Jerrams, Kaya et al., 1998).

Based on this review, the major goal of past research has been to determine the material properties of elastomers by characterizing their stress-strain behavior. In contrast, a major goal of the present research is to investigate indentation of an elastomer material to the point at which separation is likely to occur as a precursor to incipient cutting.

The failure of elastomer components has also been investigated by several researchers. The fracture mechanics approach is widely adopted to study the strength of elastomer. The concept originally proposed (Rivlin and Thomas, 1953) assumed that failure occurred locally by crack growth resulting from imperfections such as small cracks present in the material. In this work, the critical amount of energy required to advance a crack per unit area was expressed by:

$$T = -\left(\frac{\partial W}{\partial A}\right)_l \quad (2.13)$$

where

- T = strain energy release rate or tearing energy
- W = total strain energy stored in the material
- A = area of one fracture surface of the crack
- l = constant length for which the applied external force does no work.

The tearing energy concept was used as a fracture criterion to predict the critical load for crack propagation (Pidaparti and Pontula, 1995). In this work, the fracture criterion is defined by:

$$T \geq T_c \quad (2.14)$$

where T_c = critical tearing energy obtained empirically.

As previously described, the constitutive behavior of hyperelastic materials can be characterized in terms of the strain energy density. There is evidence from previous research that the strain energy is a critical parameter for predicting the rupture failure of elastomers. Therefore, in addition to several stress measures such as the maximum principal stress in the workpiece under the indenter tip, the strain energy density will be one of the variables to be studied for predicting incipient chip formation in wedge indentation of elastomers.

2.4 Analysis of a Machining Process

Machining involves the removal of layers from a workpiece in the form of a chip by action of a wedge shaped cutting tool. In general, chip formation can be categorized based on the cutting geometry and the deformation within the primary zone. For cutting geometry, the two major types of single edge cutting include orthogonal and oblique cutting.

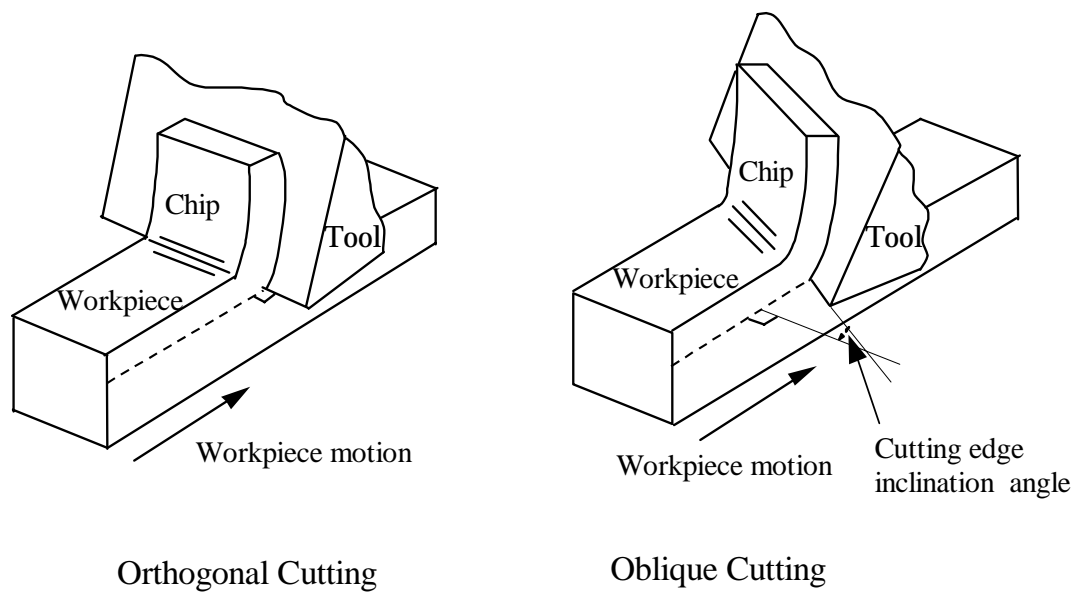


Figure 2.1 Comparison between orthogonal and oblique cutting.

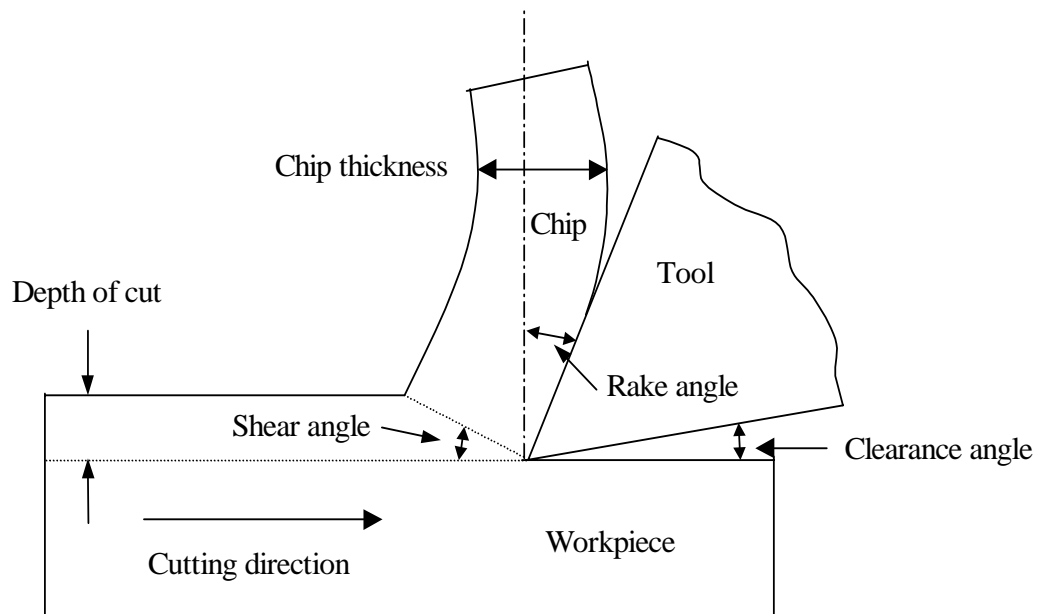


Figure 2.2 Nomenclature of orthogonal cutting.

In orthogonal cutting, the cutting edge of the tool is perpendicular to the direction of relative workpiece-tool motion and the velocity of the workpiece material is orthogonal to the tool cutting edge. Orthogonal cutting has been extensively used by several investigators to simplify the analysis of the cutting process. In practice, very few machining processes can be classified as orthogonal.

In contrast, oblique cutting refers to cutting when the cutting edge of the tool is oblique or at an angle to the movement of the relative workpiece-tool direction. The velocity of the workpiece material is inclined to the cutting edge at an inclination angle. Most machining processes such as helical end milling and drilling are classified as oblique cutting. Figure 2.1 shows both orthogonal and oblique cutting schemes, and the nomenclature of orthogonal cutting is illustrated in Figure 2.2.

Most analyses of the mechanics of cutting have been applied to a metal workpiece. Very little research has been conducted on the machining of elastomers. Kolman and Rudziejewski presented the effects of cutting parameters on the machined surface roughness in turning of rubber (Kolman and Rudziejewski, 1968). A variety of carbide end mills of various sizes and helix angles were used to mill grooves in three types of elastomers; H-NBR, Norbornone rubber, and silicone rubber at various cutting speeds (Jin and Murakawa, 1998). At high helix angle cutters and high speeds, smoother machined surfaces and lower forces were discovered. Recently, end milling and turning experiments on elastomers were conducted (Strenkowski, Shih et al., 2002). In this research, cutting tools with various diameters, materials and geometries were used in end milling for several cutting conditions with varying temperature. It was revealed that the design of the workpiece fixture, type of cutter, and

cutting conditions were major factors in achieving smooth machined surfaces. In addition, high-speed steel (HSS) tools with different rake angles were used to examine chip formation under orthogonal cutting conditions in a turning process. The results showed that both discontinuous and continuous chips occurred for the range of cutting conditions studied. Feed and tool rake angle were found to have a significant effect on the type of chips produced using turning.

End milling of elastomers has also been investigated (Shih, Lewis et al [a]., to be published), (Shih, Lewis et al [b]., to be published). In this work, the design of the workpiece fixture was found to be a critical factor in achieving good surface finish in end milling of elastomers because of the low elastic modulus. Finite element analysis was used to analyze the stiffness of the elastomer workpiece to achieve sufficient fixture rigidity. The chip morphology and cutting forces in end milling were also analyzed. Chip classification based on size and morphology was examined using Scanning Electron Microscopy (SEM) micrographs. Cutting force components were recorded using both solid carbon dioxide cooled elastomers and elastomers at room temperature. The maximum uncut chip thickness at the average peak cutting force was identified for various spindle speeds. The possibility of adiabatic shear band formation in serrated chip formation due to low thermal conductivity of elastomers was also suggested. This research provided valuable background for investigating the mechanics of elastomer machining.

Considering that there is a large percentage of elongation before failure and that the elastic modulus of elastomers is extremely small, there are many differences between the machining

of metals and elastomers. For instance, fixture design of the workpiece is very critical so that adequate structural support is provided. In addition, the cutting forces for elastomer machining are much lower than those in conventional metal cutting. These factors are important considerations when investigating the machining of elastomers.

With the advances in computational technology in recent decades, finite element analysis (FEA) has become a powerful technique in modern engineering practice. Metal cutting has been successfully analyzed using FEA with promising results. Strenkowski and Carroll developed an orthogonal cutting model using an updated-Lagrangian elasto-plastic dynamic formulation (Strenkowski and Carroll, 1985), (Strenkowski and Carroll, 1986). In this work, materials were considered to be elasto-plastic and strain rates were neglected. The tool was advanced into the workpiece from the incipient stage until steady state cutting was reached. However, the mesh was attached to the workpiece being modeled, which could cause problems due to severe deformation of the workpiece. Also, a prescribed chip separation criterion based on effective strain must be known in advance. The model was improved (Strenkowski and Mitchum, 1987); however, the accuracy was limited by the size of the elements in the vicinity of the cutting edge. Later, Strenkowski and Moon introduced an alternative Eulerian approach for simulating a flat tool. In this study, the grid was spatially fixed and the mesh was considered to be a control volume with a stationary grid that can be refined as necessary at the tool cutting edge where the stress and strain gradients are the highest (Strenkowski and Moon, 1990). The workpiece was treated as a viscoplastic material in which the material can flow through the control volume. The model included temperature prediction for heat that is generated due to plastic work and friction.

The restriction of a predefined tool-chip contact that existed in previous models was later modified (Athavale and Strenkowski, 1995). Further development of the cutting model was carried out by Hsieh (Hsieh 1998) to improve the model accuracy and capability for use in cutting tools with large negative rake angles. In this work, a three-dimensional twist drill model was developed in conjunction with an analytical single edge oblique cutting model (Usui, Shirakashi, et al. 1978). The calculated drilling forces, torque and temperature distribution in the drill body were obtained in this investigation.

A comprehensive finite element model based on an updated Lagrangian approach as formulated in ABAQUS, a commercial finite element code, was used to simulate chip formation in an orthogonal metal cutting process (Komvopoulos and Erpenbeck, 1991). The effects of interfacial friction on the chip-tool interface and tool wear geometry were investigated in this study. The development of a plane strain finite element analysis for orthogonal metal cutting simulation was also carried out by Shih (Shih, 1995), (Shih, 1996). The cutting process was analyzed using an unbalanced force reduction method and a sticking-sliding friction model. The effects of work material, viscoplasticity, temperature, strain and strain-rate were included in this study. The predicted residual stress distribution was correlated with x-ray diffraction measurements for various rake angles (Shih, 1996).

With the rapid growth of general purpose finite element programs such as ABAQUS, modeling of the cutting process can be readily achieved. The effect of sequential cuts on the residual stress in the machined layers was predicted using a thermo-elastic viscoplastic finite element cutting model developed with ABAQUS/Explicit (Liu and Guo, 2000). In this

work, chip formation, cutting forces, and temperatures were predicted for stainless steel. In another study, a detailed procedure for modeling the metal cutting process using ABAQUS/Standard was described (Shet and Deng, 2000). Predictions of the stress, strain, strain-rate fields and temperatures were obtained for various various tool rake angles and friction coefficients on the chip-tool interface. Recently, Unanue developed a cutting model using ABAQUS/Standard with chip separation based on a critical stress criterion at the cutting line (Unanue, Rubio et al., 2001).

Based on past work, it is evident that commercial finite element software such as ABAQUS offers potential for simulating the metal cutting process. In this dissertation, ABAQUS/Standard and ABAQUS/Explicit were adopted to simulate both half-wedge indentation and orthogonal cutting of AISI 4340 steel and elastomers. A preliminary ABAQUS/Standard model for simulating orthogonal cutting of elastomers was also developed.

3. ELASTOMER MACHINING EXPERIMENTS

3.1 Introduction

A series of orthogonal machining tests of elastomers on a conventional lathe was conducted to gain a better understanding of elastomer chip formation and to establish cutting conditions necessary to achieve a good surface finish. In orthogonal cutting, chips flow along the tool rake face in two-dimensional plane-strain deformation without lateral motion. Although turning is a three-dimensional cutting process in general, the orthogonality assumption greatly simplifies the geometry of the cutting process, while retaining the material response characteristics of the tool/workpiece interaction. Therefore, orthogonal machining was considered to be an appropriate assumption in this research. To obtain orthogonal machining conditions, an elastomer tube with large radius and a small thickness was used so that the cutting velocity variation along the tube thickness was negligible.

3.2 Experimental Setup

Elastomer machining experiments were conducted on a conventional lathe as shown in Figure 3.1. Rubber tubes obtained from Lord Corporation (Batch No. CS-02-003288) were used as specimens in this study. Each rubber tube had an outside diameter of 95.25 mm and a wall thickness of 11.61 mm. Great care was taken to achieve sufficiently stiff fixturing of the rubber tube. The fixture consisted of attaching the rubber tube to an aluminum mandrel of an 76.2 mm outside diameter and a 3.175 mm wall thickness. The fixture design is shown

in Figure 3.1. The aluminum mandrel provided a strong structural support that constrained the rubber workpiece against the cutting forces. In the experiments, the edge of the rubber tube overhung approximately 38 mm from the aluminum mandrel edge so that only the rubber was machined during the cutting tests. A pipe clamp was also used to secure the rubber specimen to the aluminum mandrel. The aluminum mandrel with the attached rubber specimen to the aluminum mandrel. The aluminum mandrel with the attached rubber workpiece was secured in the lathe chuck as shown in Figure 3.2.

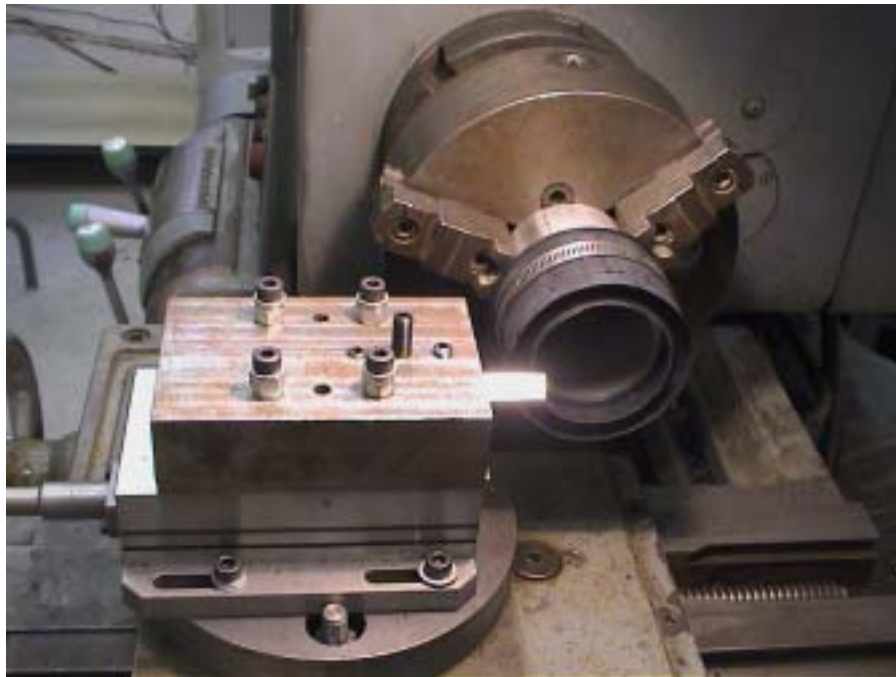


Figure 3.1 Fixture design and cutting tool setup for the elastomer machining experiments.

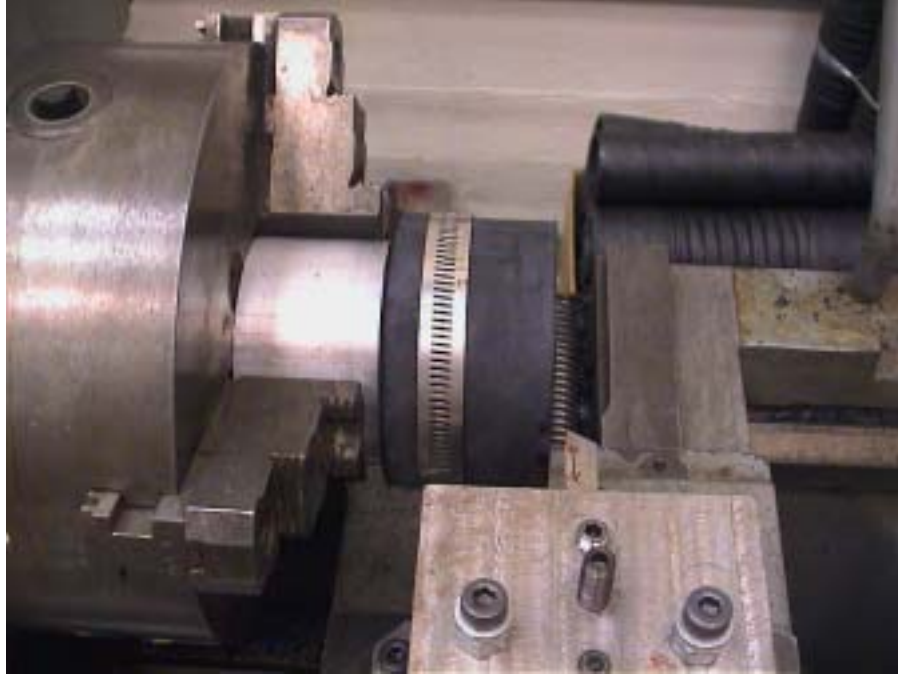


Figure 3.2 Side view of workpiece in the lathe chuck for the elastomer machining experiments.

Elastomer machining experiments were performed on a 5 horsepower Cincinnati Hydroshift lathe. Various cutting tool geometry and cutting conditions were used to study the effects on chip morphology, machined surfaces, and cutting forces. A set of 12.7 mm square solid high speed steel (HSS) cutting tool blanks were ground to a sharp edge with a clearance angle of 5 degrees and rake angles of 10, 30, and 50 degrees. The nomenclature of the cutting tool angles is shown in Figure 3.3. Two feed speeds of 0.0635 and 0.2540 mm/rev and a cutting speed of 2.50 m/s were used in these tests. The tests were conducted at room temperature under dry conditions. Elastomer chips were collected in each cutting experiment and photographs of the chips and the machined surfaces of rubber were recorded for further evaluation.

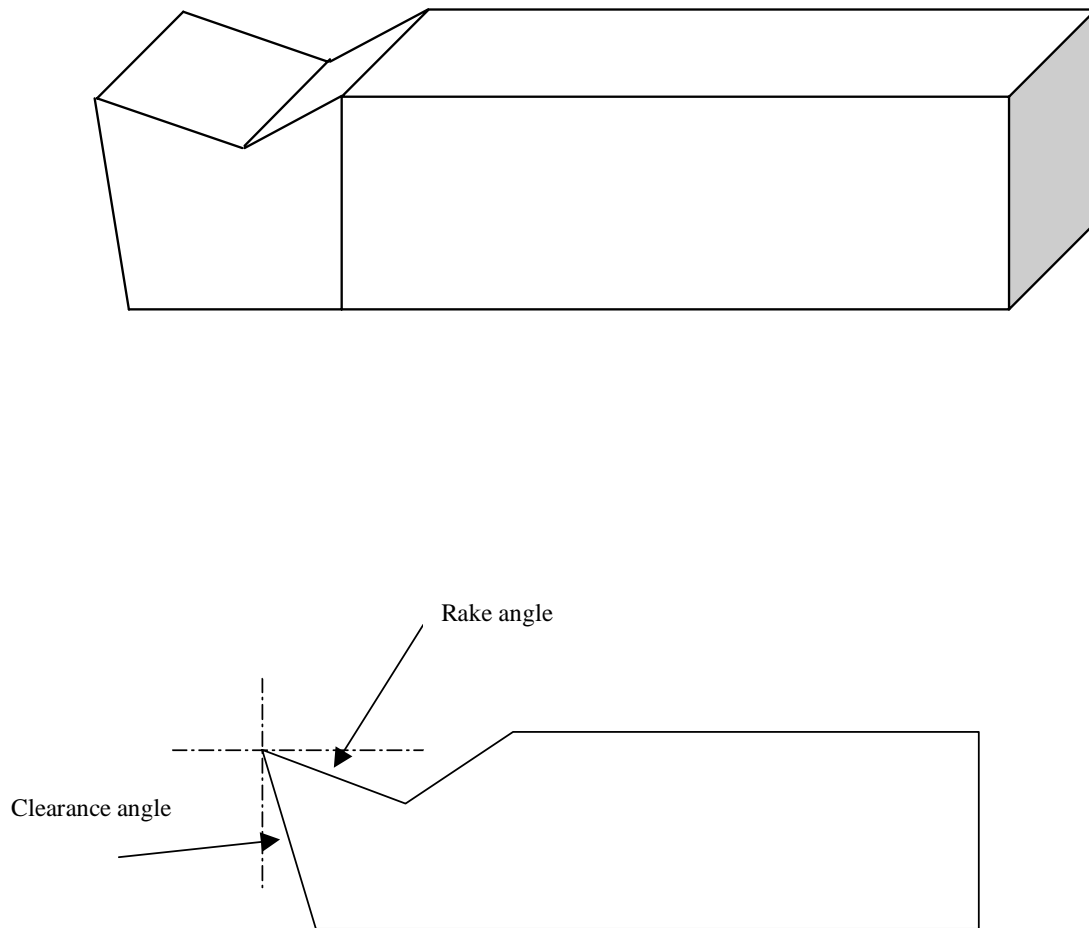


Figure 3.3 Nomenclature of cutting tool angles.

Cutting forces in three directions were measured with a data acquisition system based on LabView, a graphical data acquisition software package (National Instruments, 2001). In this setup, a three-component Kistler dynamometer (model 9257B) was used to record the force signals. For each of the force components, a proportional electrical charge was obtained and then directed into a Kistler charge amplifier (model 5001) where they were converted into proportional voltages for display and further evaluation. Data was acquired with the dynamometer in conjunction with an I/O connector block (model CB-68LP) and a multifunction data acquisition (DAQ) board NI-6024E (up to 200,000 samples/second sampling rate and 12-bit resolution), which was installed in a personal computer with LabView (version 6i). A sampling rate of 1000 samples per second was used to obtain force signals in this research.

For calibration, a force-voltage conversion factor for each measurement axis was obtained with a hanging scale and a series of known weights. The average conversion factors were found to be 11.20, 10.80, 12.00 lb/volt for the x, y, and z, axes, respectively. Before the actual force was measured, a spindle speed calibration of the lathe was performed in order to ensure accurate speeds. A Monarch Nova-Strobe (model AB) stroboscope (100-8,000 flashes/minute) was used for this purpose. Note that the lateral force was also measured and found to be approximately zero, thus confirming the orthogonality condition.

3.3 Experimental Results and Discussion

Chip shape and form provide useful information of the deformation characteristics of elastomers during machining. Figure 3.4 shows various chip types corresponding to cutting tools with rake angles of 10, 30 and 50 degrees and two feed speeds for a constant cutting speed of 2.50 m/s. The type of chip formed is highly dependent on rake angle and feed speed. In general, discontinuous chips occur for the smaller rake angle of 10 degrees and at the lower feed speed of 0.0635 mm/rev. As the rake angle and feed speed are increased, rubber chips become more continuous.

The elastomer machining experiments also provide useful information for identifying machining conditions that lead to continuous chip formation and a smooth machined surface finish. The type of chip produced during machining is important because discontinuous chip formation is associated with a rough surface finish. Conversely, continuous chips are an indication of a smooth machined surface finish. In the cutting experiments, a surface finish during orthogonal cutting was observed for a range of feed speeds and tool rake angles. Figure 3.5 shows the surface finishes for six different cases corresponding to three tool rake angles and two feed speeds for a constant cutting speed of 2.5 m/s. Clearly, it can be seen that the roughest surface occurs for the smallest rake angle of 10 degrees and the lower feed of 0.0635 mm/rev. As expected, the larger feed of 0.2540 mm/rev and the largest rake angle of 50 degrees produce the smoothest surface finish. This corresponds to the continuous chips shown in the upper right portion of Figure 3.4.

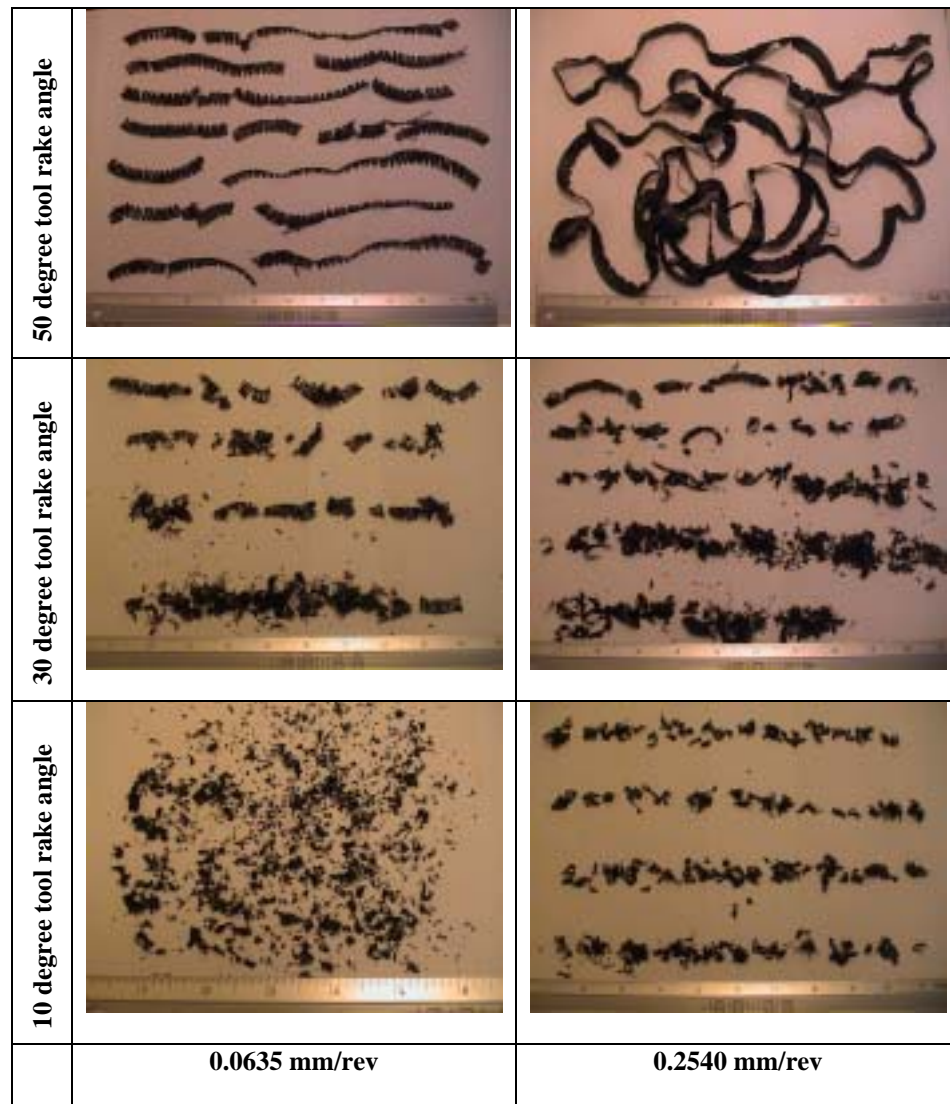


Figure 3.4 Chip types for various tool rake angles and feed speeds for a cutting speed of 2.50 m/s.

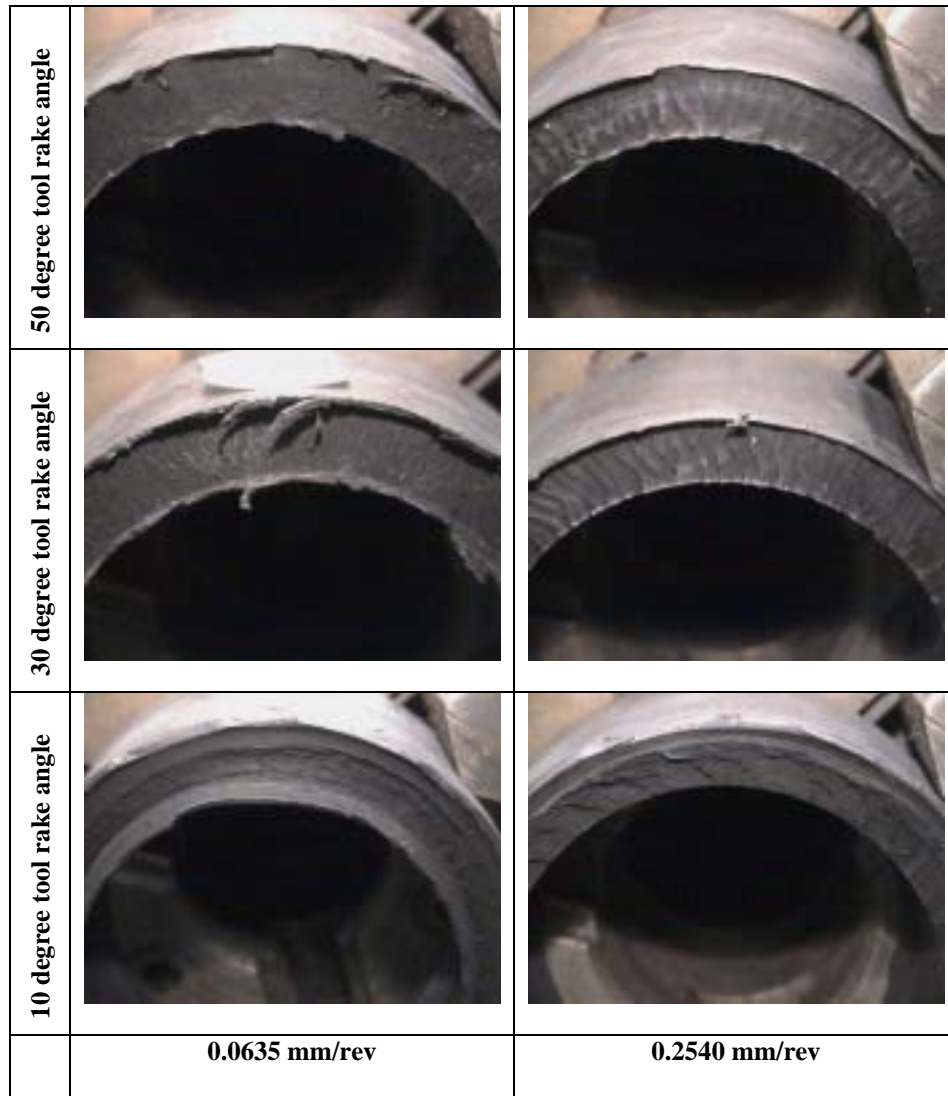


Figure 3.5 Photographs of machined surfaces for a cutting speed of 2.50 m/s for three tool rake angles and two feed speeds.

Machining forces in all three axes were also recorded. The sample force traces are shown in Figures 3.6 and 3.7. Cutting and thrust forces were recorded as well as the transverse force to confirm that it was approximately zero, as required for orthogonality. Fluctuation of all measured forces occurred as a result of the flexibility of rubber. Also it can be seen that a higher uniform fluctuation of the measured machining forces occurred for the discontinuous chips for a 10 degree rake angle and a feed speed of 0.0635 mm as shown in Figure 3.6. In contrast, a cutting tool with a large rake angle and high feed speed produced less force fluctuation as shown in Figure 3.7. Recall that this corresponded to continuous chip formation and a smooth surface finish.

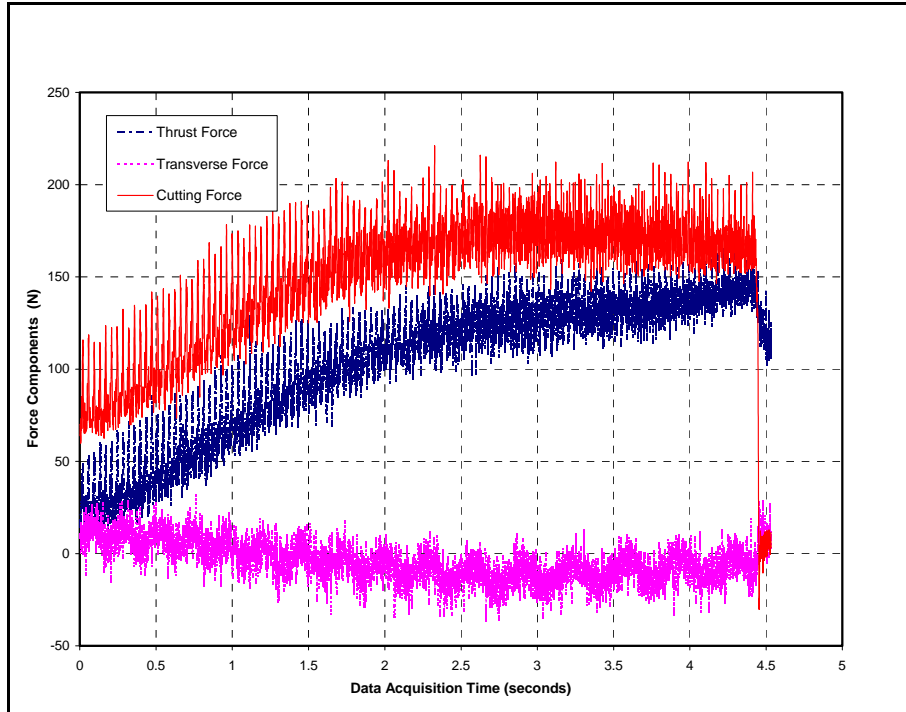


Figure 3.6 Typical measured machining forces in three axes (cutting, thrust, and transverse components) for a sharp cutting tool with a rake angle of 10 degrees, feed speed of 0.0635 mm, and cutting speed of 2.50 m/s.

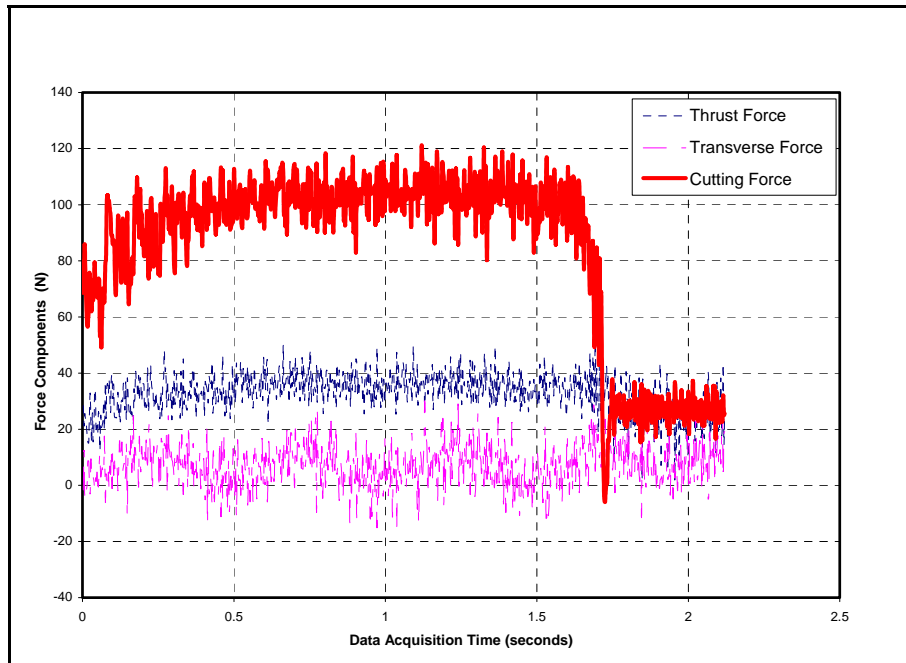


Figure 3.7 Typical measured machining forces in three axes (cutting, thrust, and transverse components) for a sharp cutting tool with a rake angle of 50 degrees, feed speed of 0.2540 mm, and cutting speed of 2.50 m/s.

The average values of cutting force and thrust forces were plotted over a range of tool rake angles at two different feed speeds as shown in Figures 3.8 and 3.9. As expected, the average cutting force is larger than the average thrust force for both feed speeds used in the study. Figure 3.10 shows a comparison of the average cutting force for various rake angles and feed speeds. A similar comparison of the average thrust force is shown in Figure 3.11. As expected, both the average cutting and thrust forces decrease as the tool rake angle increases.

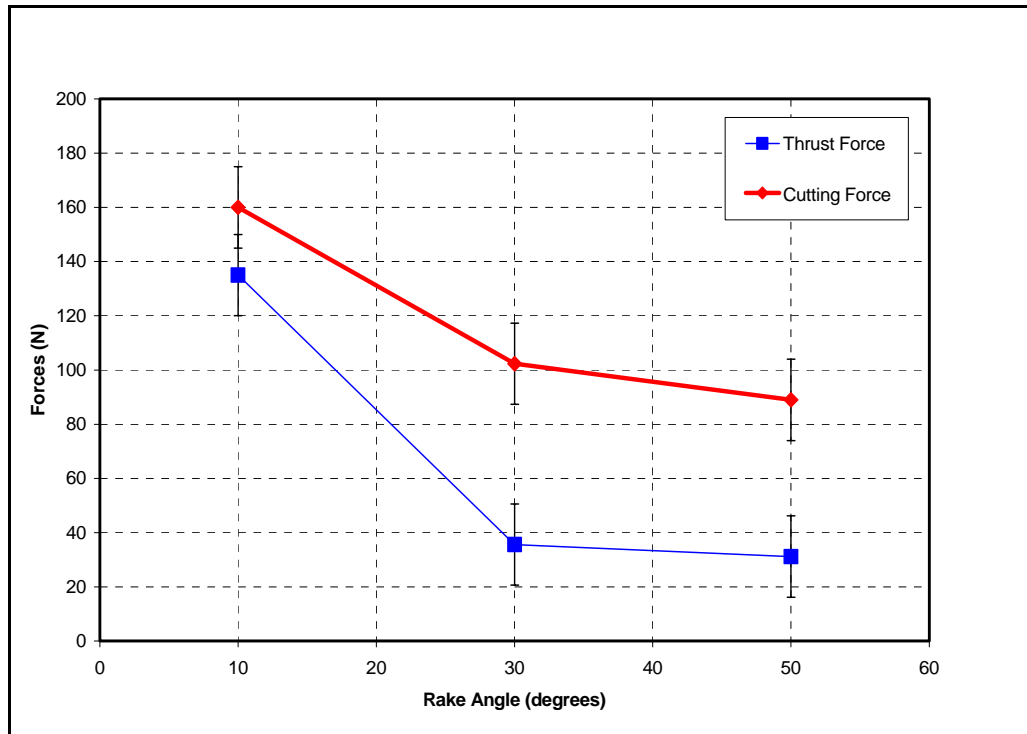


Figure 3.8 Measured force components for a sharp cutting tool with various tool rake angles, a feed speed of 0.0635 mm and a cutting speed of 2.50 m/s.

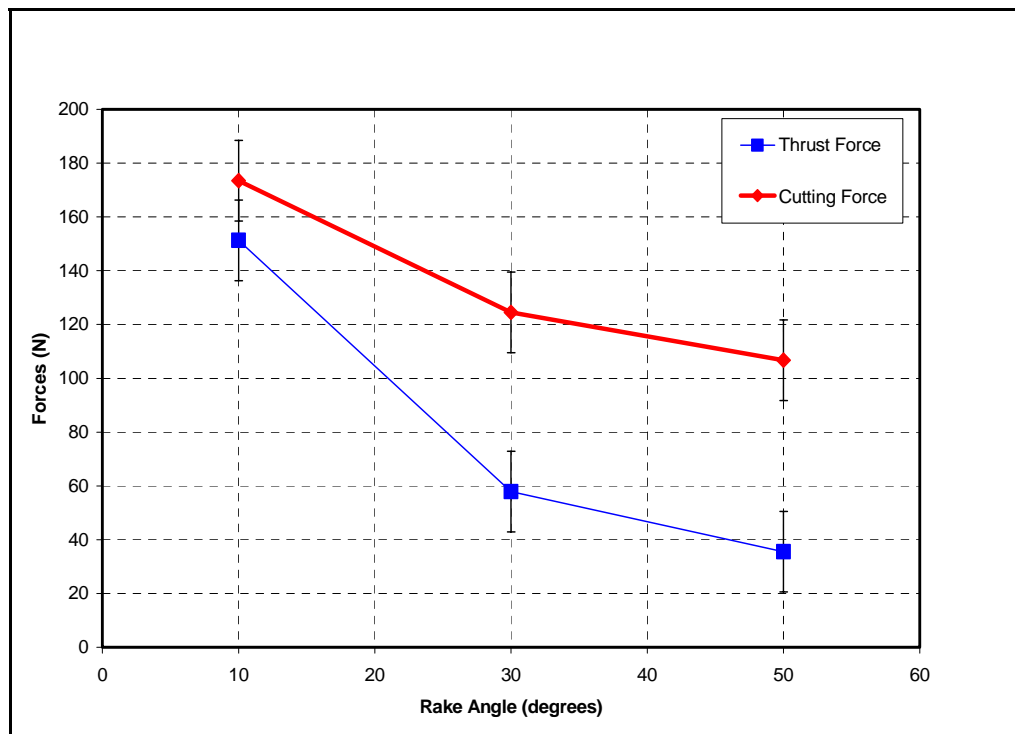


Figure 3.9 Measured force components for a sharp cutting tool with various tool rake angles, a feed speed of 0.2540 mm and a cutting speed of 2.50 m/s.

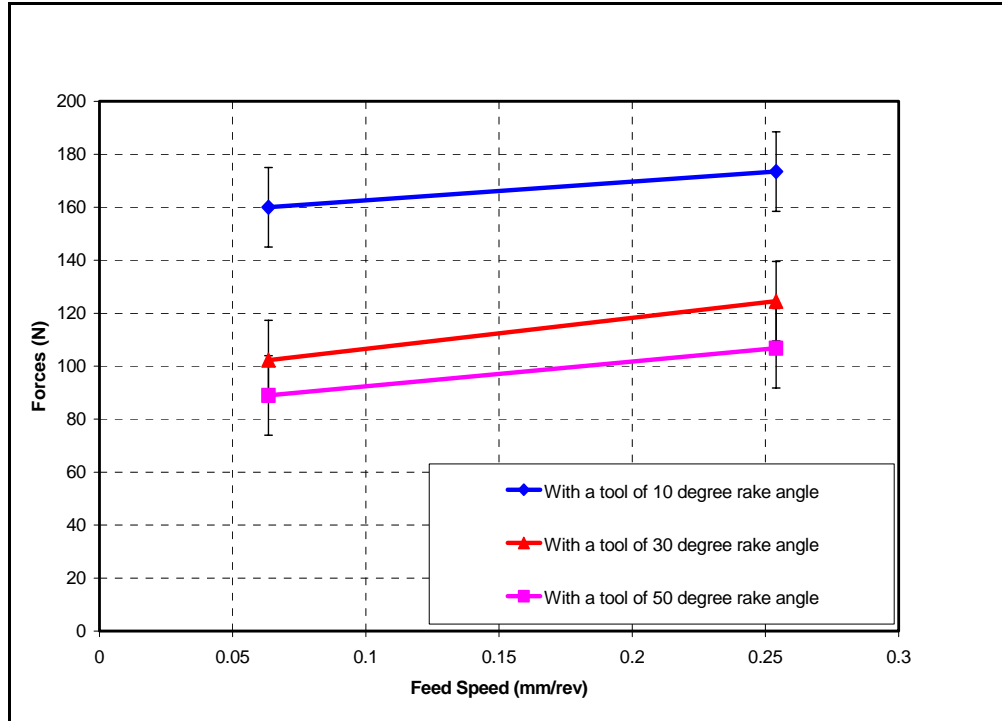


Figure 3.10 Comparison of measured cutting forces for cutting tools with various rake angles and feed speeds for a cutting speed of 2.50 m/s.

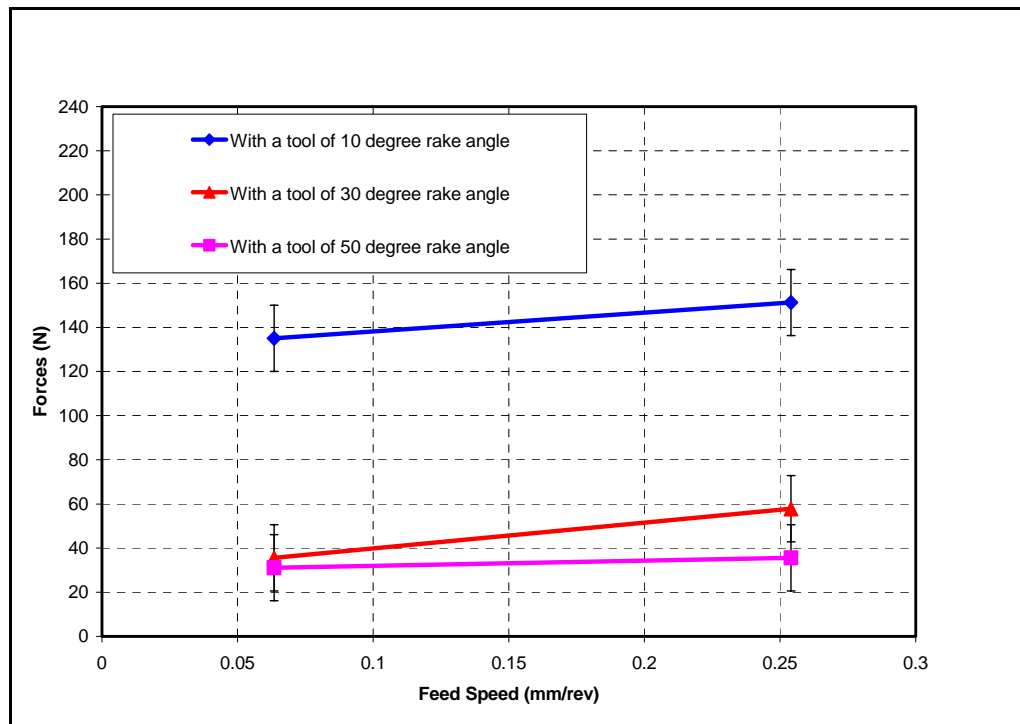


Figure 3.11 Comparison of measured thrust forces for cutting tools with various rake angles and feed speeds for a cutting speed of 2.50 m/s.

In addition, the sharpness of the cutting edge was measured off-line using a portable Keyence optical microscope model VH-6100 and a lens model VH-1001 (1000x) with a lighting system shown in Figure 3.12. The nose width of the cutting edge was measured and then used to calculate the tool edge radius. Figure 3.13 shows the schematic diagram used to obtain the tool edge radius.



Figure 3.12 Apparatus for measuring the cutting edge sharpness.

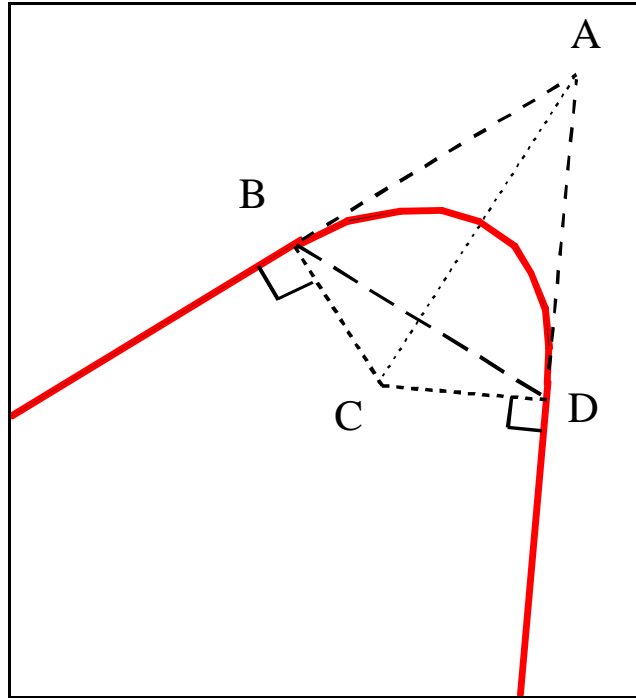


Figure 3.13 Schematic diagram to determine the tool edge radius (Hsieh 1998).

With an assumption of a circular tool nose, the tool edge radius (length BC or CD) can be determined from length BD and angle A. The length BD is the measured nose width. The angle A is called the included angle and it can be determined once the tool rake and clearance angles are known. As shown in Figure 3.13, the tool edge radius can be found as (Hsieh 1998):

$$\text{Tool edge radius (length CB or CD)} = \frac{\left(\frac{\overline{BD}}{2}\right)}{\cos\left(\frac{\hat{A}}{2}\right)} \quad (3.1)$$

where \overline{BD} = Measured nose width of the cutting edge

\hat{A} = Included tool angle which is equal to 90° - tool rake angle – tool clearance angle.

Measured nose widths of the cutting edge for a 10 degree rake angle tool are shown in Figures 3.14 and 3.15. Nose widths of 10 microns were found for both the unused and used tools. Due to the short cutting time used in the cutting experiments, nose widths of the tool remained unchanged after cutting.

Using equation (3.1), the tool edge radius for both conditions can be determined as follows.

For an unused 10 degree rake angle tool, \overline{BD} = 10 micron, $\hat{A} = 90 - 10 - 5 = 75$ degrees;

$$\text{Tool edge radius} = \frac{\left(\frac{10}{2}\right)}{\cos\left(\frac{75}{2}\right)} = 0.0063 \text{ mm}$$

Similar results for nose width measurements for unused and used 30 degree and 50 degree rake angle tools are shown in Figures 3.16 and 3.17, and Figures 3.18 and 3.19, respectively. The nose width for these tools was also found to be 10 microns. Using equation (3.1), the tool edge radii for the 30 degree and 50 degree rake angle tools were also calculated to be 0.0056 and 0.0052 mm, respectively. Note that more light reflection occurred for the tools with the smaller rake angles, as shown in Figures 3.14 – 3.19.

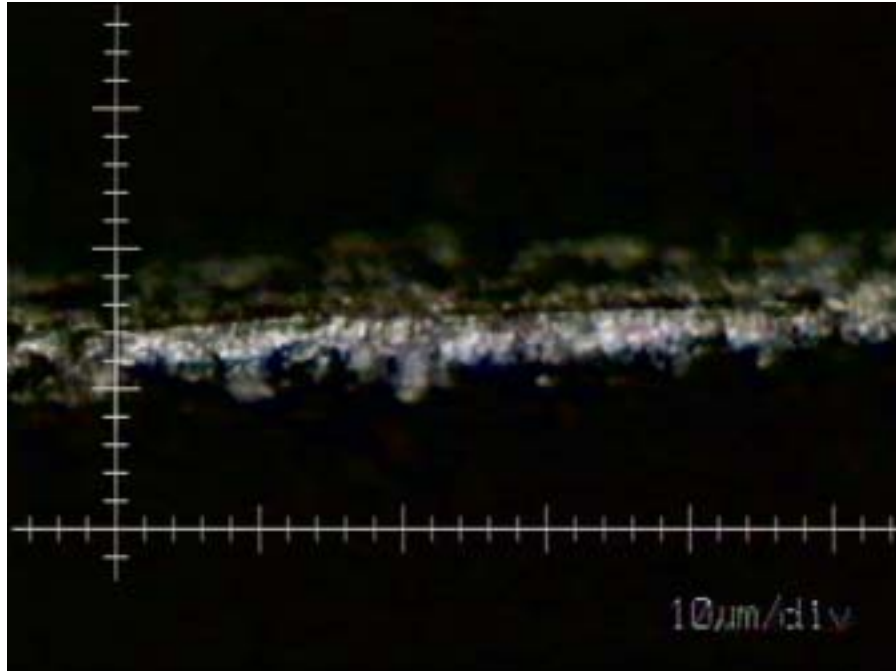


Figure 3.14 Unused tool edge with a nose width of 10 microns (10 degree rake angle, 5 degree clearance angle).

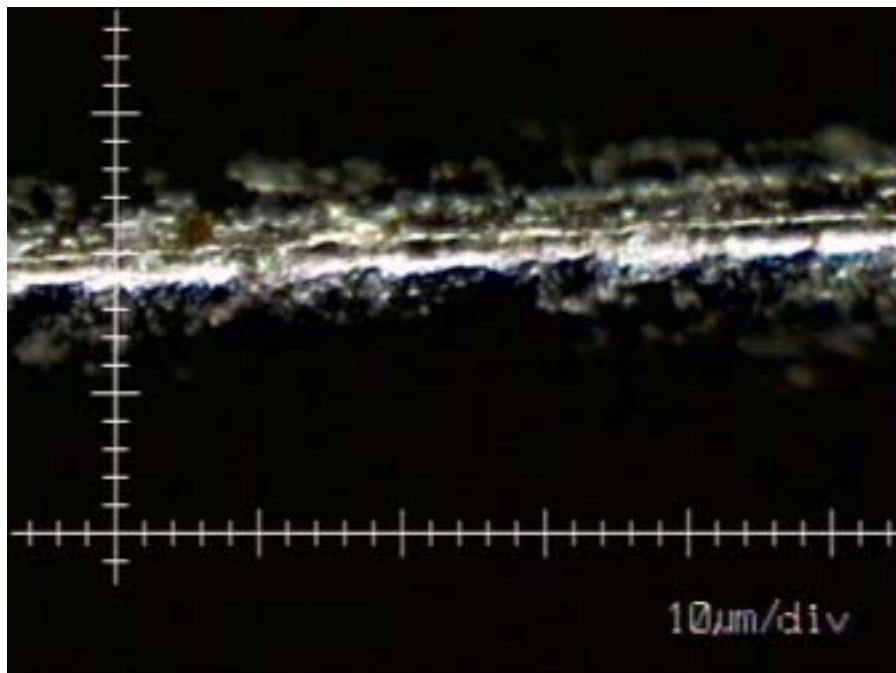


Figure 3.15 Used tool edge with nose a width of 10 microns (10 degree rake angle, 5 degree clearance angle).

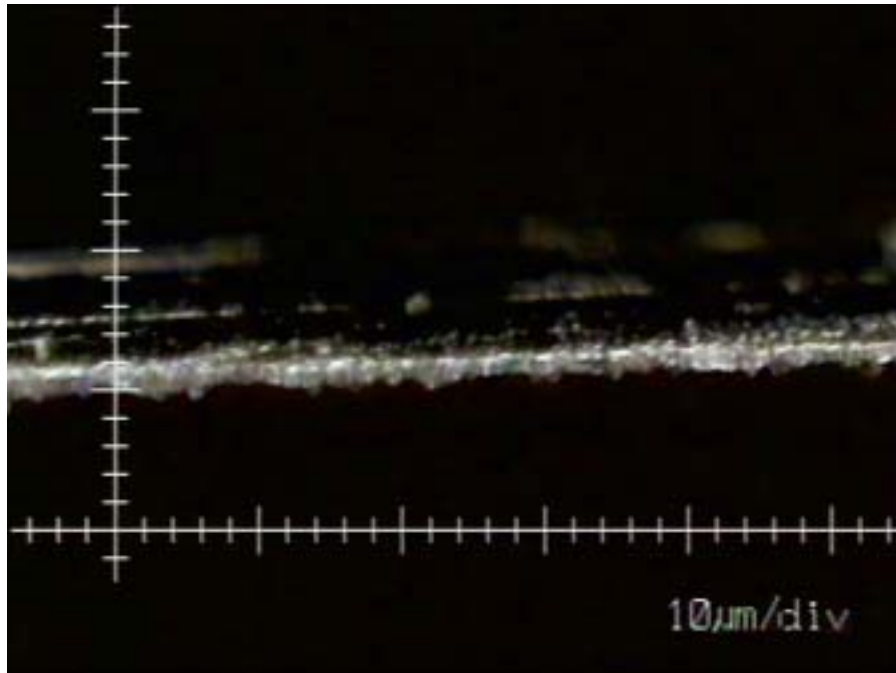


Figure 3.16 Unused tool edge with a nose width of 10 microns (30 degree rake angle, 5 degree clearance angle).

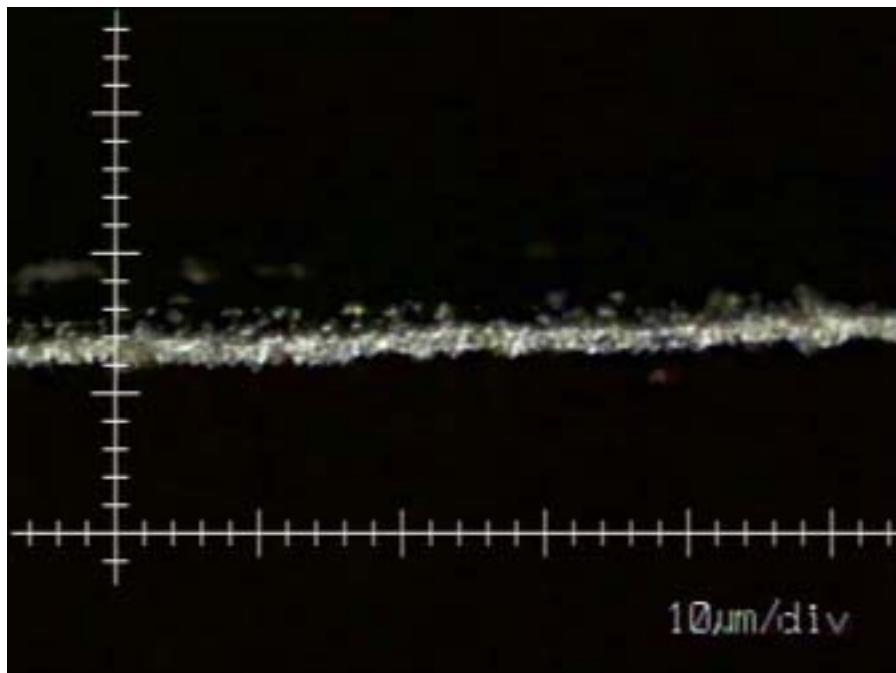


Figure 3.17 Used tool edge with a nose width of 10 microns (30 degree rake angle, 5 degree clearance angle).

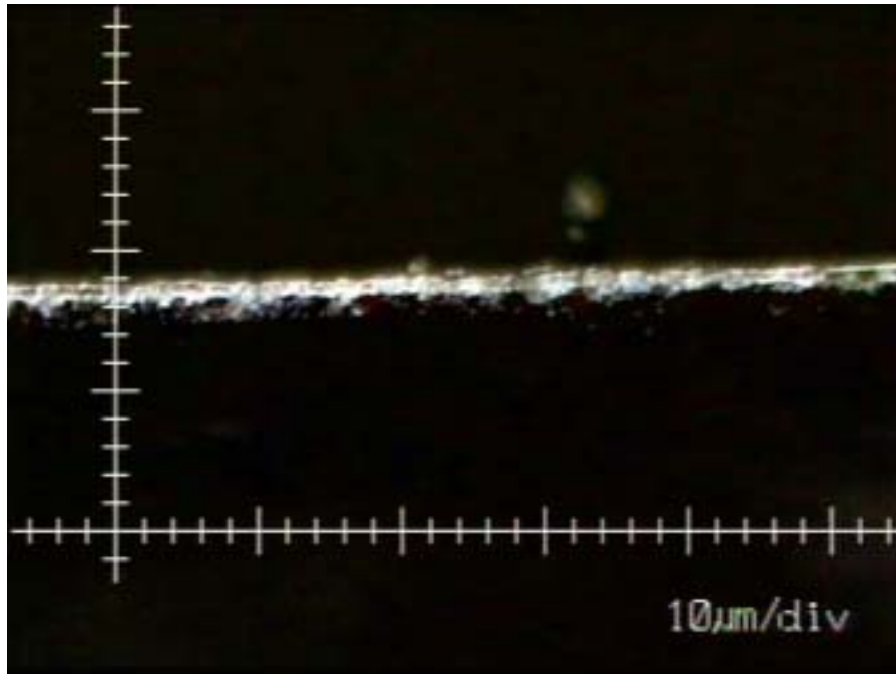


Figure 3.18 Unused tool edge with a nose width of 10 microns (50 degree rake angle, 5 degree clearance angle).

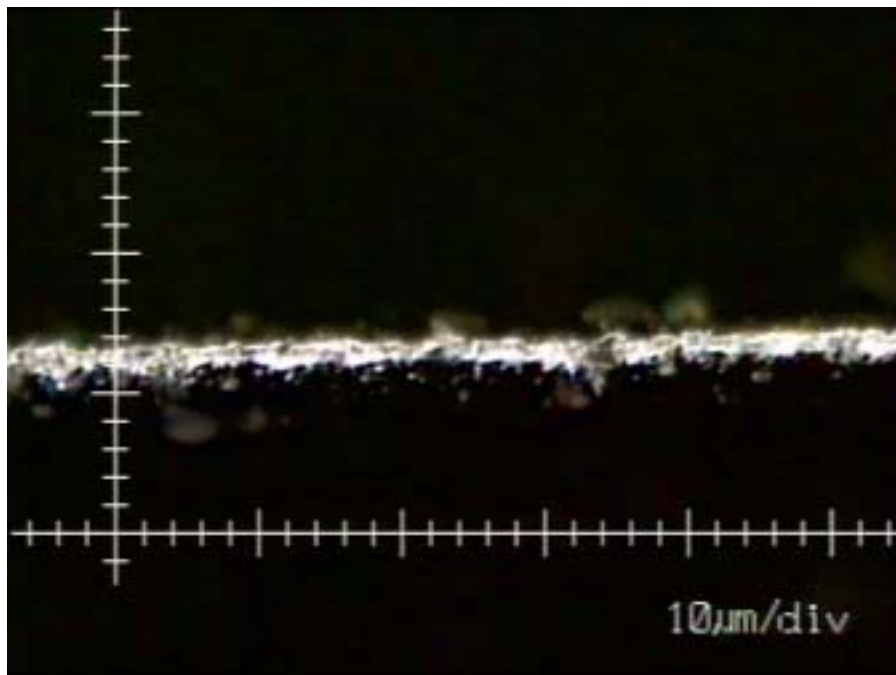


Figure 3.19 Used tool edge with a nose width of 10 micron (50 degree tool rake angle, and 5 degree clearance angle).

4. DESCRIPTION OF MODEL DEVELOPMENT

Two-dimensional finite element models of half-wedge indentation of elastomers and AISI 4340 steel were developed in this dissertation using ABAQUS/Explicit (ABAQUS/Explicit software, 2001). In addition, ABAQUS/Standard (ABAQUS/Standard software, 2001) was used to model the cutting of AISI 4340 steel for verification of modeling output parameters selected in the wedge indentation analysis. A preliminary elastomer cutting model was also developed using ABAQUS/Standard. A brief background of the ABAQUS software and its applicability for simulating indentation and cutting processes is described in the following sections.

4.1 A General Description of the ABAQUS Software

ABAQUS is a collection of engineering simulation programs, based on the finite element method, which can be used to solve highly non-linear problems. A wide range of typical engineering materials such as metals, rubber, polymers, composites, reinforced concrete, crushable and resilient foams, and geotechnical materials is included in the material model library in ABAQUS. In a typical simulation, engineering data such as geometry of the structure, material behavior, boundary conditions, and applied loads are provided by the user. For a non-linear analysis, the appropriate load increments are automatically determined and the convergence tolerances are continually adjusted by ABAQUS to ensure that an accurate and efficient solution is obtained (ABAQUS/Standard User's Manual, 2001).

The two major analysis modules of ABAQUS are ABAQUS/Standard and ABAQUS/Explicit. Other modules such as ABAQUS/CAE and ABAQUS/Viewer are used for preprocessing and postprocessing analyses. ABAQUS/CAE is the complete ABAQUS environment that includes capabilities for creating ABAQUS models, interactively submitting and monitoring ABAQUS jobs, and evaluating results. ABAQUS/Viewer is a subset of ABAQUS/CAE that includes only the postprocessing capability. The ABAQUS modules are shown in Figure 4.1.

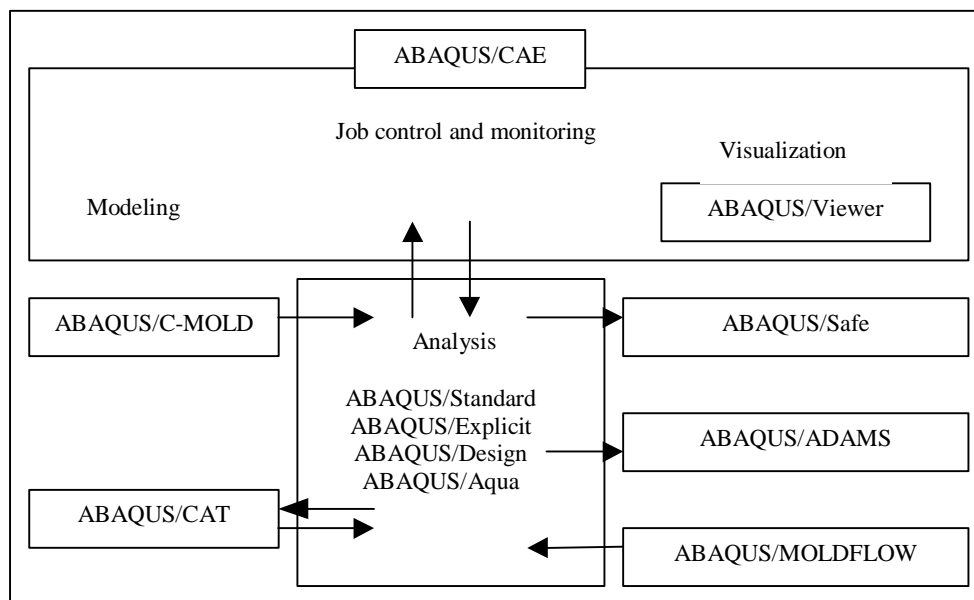


Figure 4.1 ABAQUS modules (Getting Started with ABAQUS/Standard Manual, 2001).

The specific details for each analysis stage in ABAQUS are as follows:

1. Preprocessing (ABAQUS/CAE)

In this stage, the model of the physical problem is defined and an input file can be graphically created through ABAQUS/CAE or it can be directly entered using a text editor.

2. Simulation (ABAQUS/Standard and ABAQUS/Explicit):

In this stage, ABAQUS/Standard or ABAQUS/Explicit solves the numerical problem as defined in an input file. Output from a typical stress analysis includes displacement and stresses, which are stored in files for postprocessing. Solution times can vary significantly depending on the complexity of the analysis and the available computational power.

3. Postprocessing (ABAQUS/Viewer)

When the simulation has been completed, the results can be evaluated interactively using ABAQUS/Viewer. A variety of options for displaying the results including deformed shape plots, contour plots, x-y plots, and animations are provided.

4.1.1 ABAQUS/Standard

ABAQUS/Standard is a general-purpose analysis module that can solve both linear and non-linear problems including static, dynamic, and thermal analyses. Linear equation solution is achieved using a direct Gauss elimination method. This is usually the most time-consuming part of the analysis especially for large models, and storage of the equations occupies the

largest part of the disk during the calculations. For non-linear problems, the Newton method is used to solve the non-linear equations. Other activities include determination of convergence, load as a function of time, and automatically choosing suitable time increments (ABAQUS/Standard User's Manual, 2001).

4.1.2 ABAQUS/Explicit

ABAQUS/Explicit is an explicit dynamics finite element module that utilizes an explicit dynamic finite element formulation. It is more suitable for modeling transient dynamic events such as impact problems. It is also very efficient for highly non-linear problems involving changing contact conditions such as metal forming processes. Contact conditions are readily formulated in the explicit formulation and can be enforced on a node-by node basis without any iteration. The nodal accelerations are adjusted to balance the external and internal forces during contact. One of the most attractive features of the explicit method is that a global tangent stiffness matrix is not required as with implicit methods. In summary, the distinguishing characteristic of the explicit method is that it requires a small time increment size that depends solely on the highest natural frequencies of the model and is independent of the type and duration of loading.

Simulations with an explicit approach normally take on the order of 10,000 to 1,000,000 increments, but the computational cost per increment is relatively small. In comparison, the implicit method does not have any limitation on the time increment size, and increment size is generally determined from accuracy and convergence considerations. Implicit simulations

typically require fewer increments than explicit simulations. However, the cost per increment of an implicit method is much greater than that of an explicit method since a global set of equations must be solved for each increment.

4.2 Finite Element Implicit and Explicit Time Integration

As mentioned previously, implicit time integration techniques are suitable for solving linear static problems, while explicit methods are more effective for solving highly non-linear dynamic problems such as simulating manufacturing processes. In an implicit time integration scheme, the forward difference solution with constant average accelerations is used. The governing equations of the implicit method are as follows (Lovell, Bhattacharya et al., 1998):

At time t_{n+1} :

$$[M]\{\ddot{u}_{n+1}\} + [C]\{\dot{u}_{n+1}\} + [K]\{u_{n+1}\} = \{F_{n+1}^a\} \quad (4.1)$$

Where $[M]$ = mass matrix

$[C]$ = stiffness matrix

$[K]$ = damping matrix

\ddot{u}_{n+1} = nodal accelerations

\dot{u}_{n+1} = nodal velocities

u_{n+1} = nodal displacements

F_{n+1}^a = applied force at time $n+1$.

With the assumption of constant average acceleration, the velocity and acceleration equations can be written as:

$$\ddot{u}_{n+1} = \frac{4}{(\Delta t)^2}(u_{n+1} - u_n) - \frac{4}{\Delta t}\dot{u}_n - \ddot{u}_n \quad (4.2)$$

$$\dot{u}_{n+1} = \dot{u}_n + \frac{2}{\Delta t}\ddot{u}_n + \frac{2}{\Delta t}\ddot{u}_{n+1} \quad (4.3)$$

Where Δt is the time step.

Substituting equations (4.2) and (4.3) in equation (4.1), the displacement equation can be expressed as:

$$\left(\frac{4}{(\Delta t)^2}[M] + \frac{2}{\Delta t}[C] + [K] \right) \{u_{n+1}\} = \{F_{n+1}^a\} + [M] \left(\frac{4}{(\Delta t)^2}\{u_n\} + \frac{4}{\Delta t}\{\dot{u}_n\} + \{\ddot{u}_n\} \right) + [C] \left(\frac{2}{\Delta t}\{u_n\} + \{\dot{u}_n\} \right) \quad (4.4)$$

It is noted that a system of simultaneous equations at every time step must be solved. When $[M]$, $[C]$, $[K]$ matrices are constant which is the case for linear static problems, the solution at a time step is uniform and unconditionally stable throughout the analysis solution. Nevertheless, for highly non-linear problems such as a forming process, the stiffness matrix changes at each time step due to non-linearities in material, geometry, and contact. This

causes the solution with an implicit method to be much more difficult because the mass, stiffness, and damping matrices must be inverted and a new set of simultaneous equations must be solved at each time step. It also involves some iterative technique such as a Newton-Raphson method which tends to cause convergence problems while requiring small time steps to obtain an accurate solution.

To avoid the problems described above, an explicit time integration will be used. In this method, a linear change in displacement is assumed and the central difference method is utilized. The governing equations of the explicit method are as follows:

At time t_n :

$$[M]\{\ddot{u}_n\} + [C]\{\dot{u}_n\} + [K]\{u_n\} = \{F_n^a\} \quad (4.5)$$

The nodal velocity and acceleration equations are also written as:

$$\ddot{u}_n = \frac{1}{(\Delta t)^2} (u_{n+1} - 2u_n + u_{n-1}) \quad (4.6)$$

$$\dot{u}_n = \frac{1}{2(\Delta t)} (u_{n+1} - u_{n-1}) \quad (4.7)$$

Substituting equations (4.6) and (4.7) in equation (4.5), the unknown displacement equation can be found as:

$$\left(\frac{1}{(\Delta t)^2} [M] + \frac{2}{\Delta t} [C] \right) \{u_{n+1}\} = \{F_n^a\} - \left([K] - \frac{2}{(\Delta t)^2} [M] \right) \{u_n\} - \left(\frac{1}{(\Delta t)^2} [M] - \frac{1}{2\Delta t} [C] \right) \{u_{n-1}\} \quad (4.8)$$

It can be seen that the displacement equation is uncoupled and an inverted stiffness matrix is not needed. As a result, these equations can be solved explicitly, which requires less memory and less solution time for each iteration as compared to an implicit method.

4.3 Contact and Interaction Concepts in Wedge Indentation and Orthogonal Cutting Models

In general, contact stress is transmitted when two solid deformable bodies are in contact. In addition, if friction is included, a shear stress is also generated. One of the attractive features of ABAQUS is the contact and interaction algorithm. Contact can be treated as a severely discontinuous non-linearity. In ABAQUS, either surfaces or contact elements can be used for contact interaction problems. In this dissertation, the surface-based element was utilized to simulate the contact interaction for both wedge indentation and orthogonal cutting. This contact can be categorized as contact between two deformable bodies. In addition, contact between a rigid surface and a deformable body can also be considered but care must be taken when modeling sharp edges such as at the tip of the indenter.

Three steps are necessary to define surface-based contact. First, the surfaces of the bodies that could possibly be in contact are defined, and these surfaces are called a contact pair. In this research, the element-based surfaces were used. The next step is to specify contact

between surfaces which interact with each other during analysis. The final step is to define the mechanical behavior, such as friction that might occur between surfaces in contact.

For each node on the first or slave surface, the contact algorithm in ABAQUS attempts to find the nearest point on the second or master surface of the contact pair where the master surface's normal passes through the node on the slave surface. The interaction is then discretized between the point on the master surface and the slave node as shown in Figure 4.2. To achieve accuracy, the slave surfaces should consist of a finer mesh than the master surface.

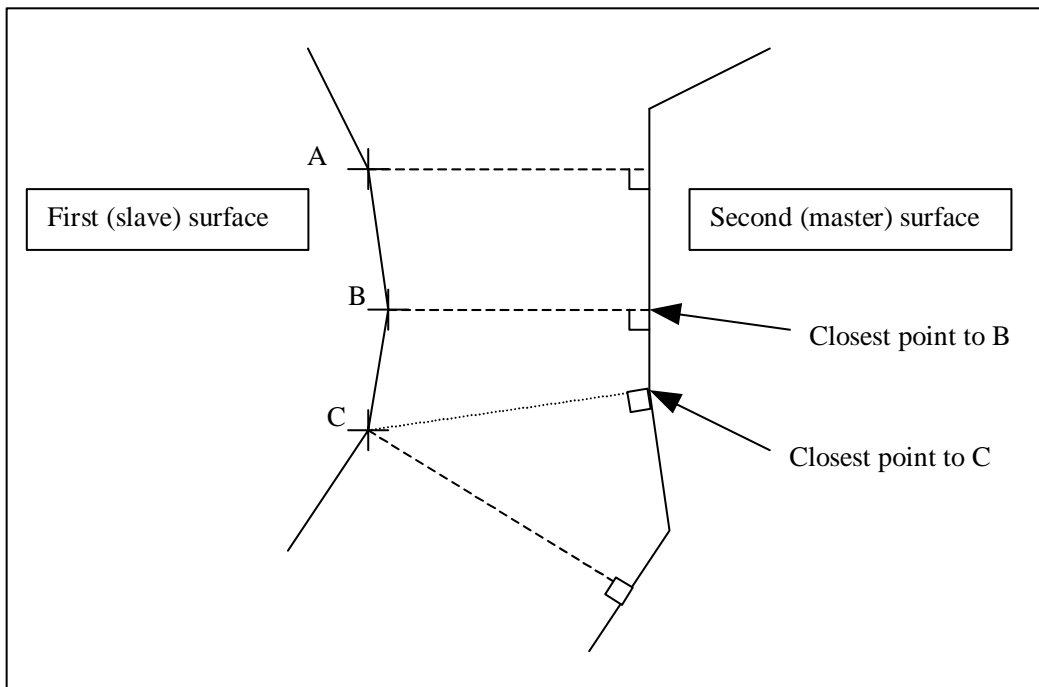


Figure 4.2 Contact and interaction discretization (ABAQUS/Standard User's Manual, 2001).

ABAQUS uses a master-slave terminology to describe the interaction between contact surfaces. In general, when both surfaces in a contact pair are deformable, the master surface is chosen as the surface of the stiffer body or as the surface with the coarser mesh if the two surfaces are on structures with comparable stiffness.

In the models developed in this research, the finite sliding characteristic was implemented. For finite sliding of deformable bodies, arbitrarily large sliding as well as large rotations and deformations of the surfaces are allowed. This is different than the small sliding characteristic in which nodes on the slave surfaces cannot slide or move more than a small distance from a point on the master surface.

Note that there are several differences in the contact algorithms in ABAQUS/Standard and ABAQUS/Explicit. One of the major differences involves the master-slave formulation. In ABAQUS/Standard, a strict master-slave formulation is used to impose contact constraints. Nodes on the slave surface are constrained not to penetrate into the master surface whereas nodes of the master surface can penetrate into the slave surface. However, in ABAQUS/Explicit, a balanced master-slave formulation is used. With this formulation the contact calculations are carried out twice with the reversion of the role of the master and slave surfaces. Then, the contact constraint is applied as a weighted average of the two master-slave constraints.

4.4 Description of Indentation and Orthogonal Cutting Models

With advanced capabilities such as contact and explicit algorithms available in commercial finite element codes such as ABAQUS, wedge indentation can be successfully simulated with the proper selection of functions and options. In this research, a half-wedge indenter was used as a cutting tool to simulate incipient cutting of metal and elastomers. Models were developed for half-wedge indentation of metal and elastomers using ABAQUS/Explicit. Post-processing analysis was performed using ABAQUS/CAE and ABAQUS/Viewer. A plane strain assumption was assumed in all the models. The models are described in the following sections.

As previously described, half-wedge indentation can be regarded as a prelude to incipient cutting. The mechanism of material separation in half-wedge indentation also leads to incipient chip formation for machining of metals. A similar concept can be applied to elastomers. Therefore, half-wedge indentation models for both metal and elastomers were also developed to investigate incipient chip formation. In this research, AISI 4340 steel was chosen since it has been used in a wide range of applications.

4.4.1 Modeling of Indentation of AISI 4340 Steel

An ABAQUS/Explicit model consists of the workpiece and a half-wedge indenter. The workpiece height and width were chosen to be 2.85 and 1.07 mm, respectively. A half-wedge indenter with various angles was used. The indenter tip was assumed to be perfectly sharp, so that the tip edge radius is zero. The initial mesh for the workpiece and indenter is shown in Figures 4.3 and 4.4.

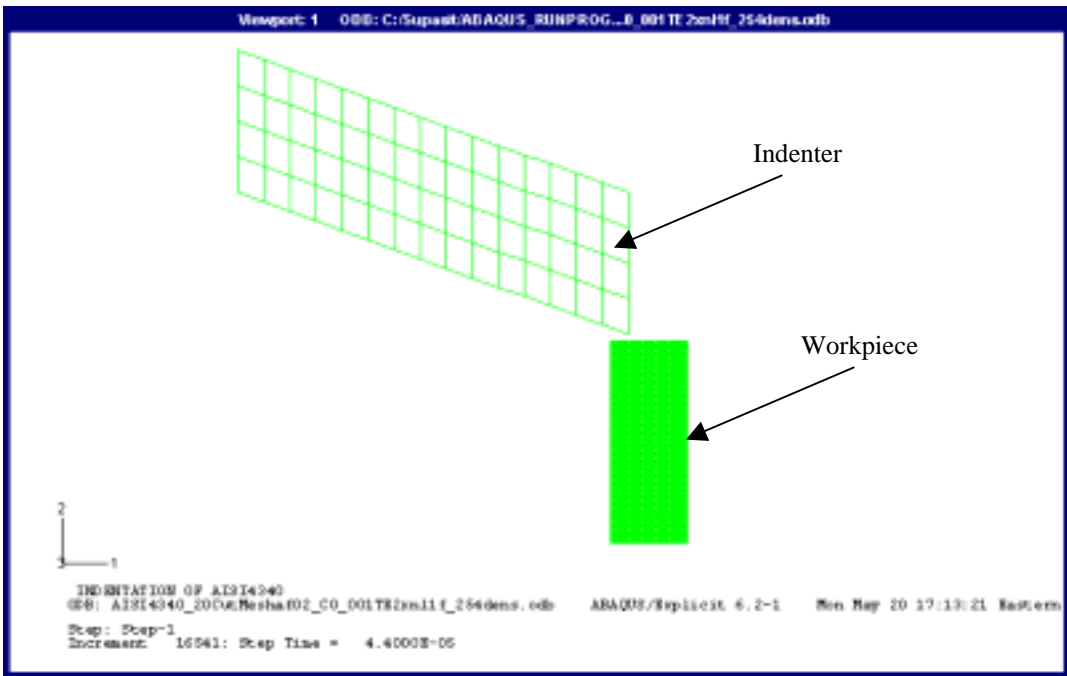


Figure 4.3 Initial mesh of a half-wedge indentation model of AISI 4340 steel.

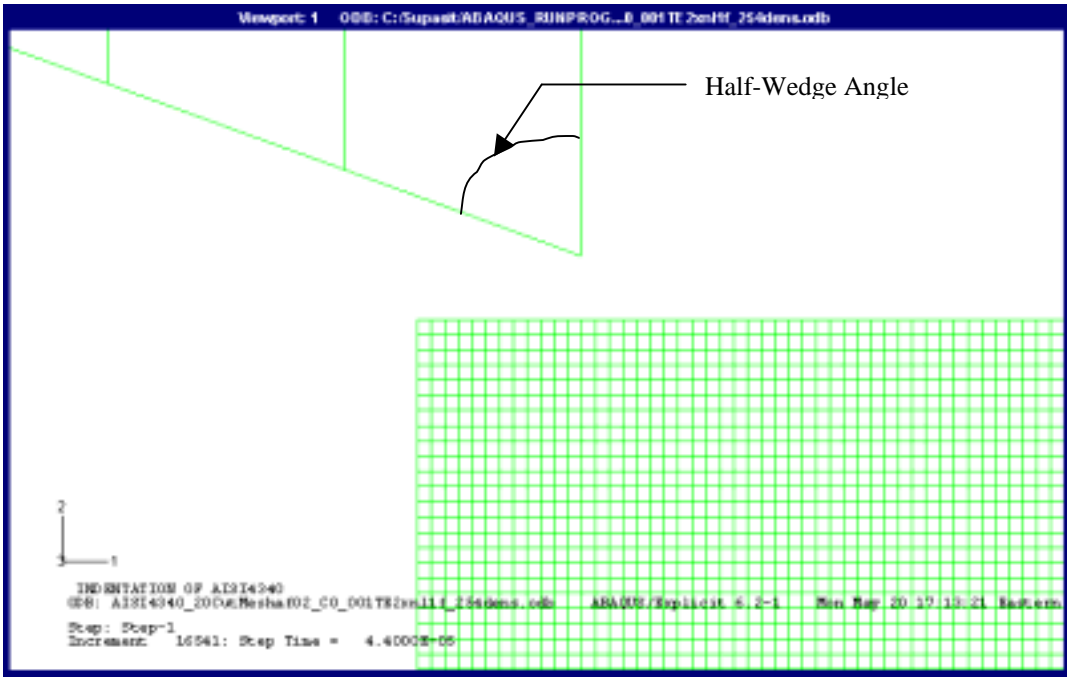


Figure 4.4 Initial mesh of a half-wedge indentation model of AISI 4340 steel (detailed view).

The AISI 4340 steel workpiece contained a total of 6171 nodes and 6000 elements. The element was a two-dimensional, 4-node bilinear plane strain element with reduced integration (CPE4R). Reduced integration means that an integration scheme of one order less than the full scheme is used to integrate the element's internal forces and stiffness. The advantage of using reduced integration elements is that the strains and stresses are determined at the locations that provide optimal accuracy. As a result, reduced-integration elements are very tolerant of distortion. Another advantage is that the scheme decreases the CPU running time and storage requirements.

Using the same element type, the indenter consisted of 80 nodes and 60 elements. The high speed steel (HSS) indenter was modeled with a modulus of elasticity of 2×10^5 MPa. AISI 4340 was chosen as the workpiece material. Material properties at room temperature (20°C) with elastic-plastic behavior and isotropic hardening was used in this research. Table 4.1 shows a summary of the material and thermal properties.

Table 4.1 A summary of the material properties of AISI 4340 steel (Shet and Deng, 2000).

| Thermal expansion coefficients of AISI 4340 steel at 20°C | | |
|---|---|------------------------|
| Temperature (°C) | Thermal expansion coefficients (µm/m K) | |
| 20 | 12.3 | |
| Elastic properties of AISI 4340 steel at 20°C | | |
| Temperature (°C) | Elastic of modulus (GPa) | Poisson's ratio |
| 20 | 207 | 0.3 |
| Elastic-plastic properties of AISI 4340 steel at 20°C | | |
| Temperature (°C) | Flow stress (MPa) | Plastic strain (mm/mm) |
| 20 | 414 | 0.00 |
| 20 | 517 | 0.01 |
| 20 | 759 | 0.09 |
| 20 | 1100 | 0.90 |

The strain-rate property of the material is governed by the constitutive power law relationship (Komvopoulos and Erpenbeck, 1991):

$$\dot{\epsilon}_p = D \left(\frac{\sigma_{ef}}{\sigma_Y} - 1 \right)^p \quad \text{for} \quad \sigma_{ef} \geq \sigma_Y \quad (4.9)$$

where $\dot{\epsilon}_p$ = effective plastic strain rate

σ_{ef} = effective yield stress

σ_Y = initial yield stress

D, p are material constants based on empirical strain-rate sensitivity.

The value of D of $2.21 \times 10^5 \text{ s}^{-1}$ and p of 2.87 was adopted for the material model of AISI 4340 steel in this research. A mass density of 7800 kg/m^3 and specific heat of 502 J/kg K were also input to complete the material model.

The right and the bottom boundaries of the workpiece shown in Figure 4.3 were constrained in all three translational degrees of freedom. The indenter was constrained to move vertically downward with a constant speed of 2.5 m/s. In the model, the indenter/workpiece was defined as one master/slave contact pair. A coulomb friction coefficient of 0.20 was assumed on the contact surface. In the analysis procedure in ABAQUS/Explicit, a dynamic load condition was used with non-linear analysis. The amplitude curve of indenter displacement and time was provided in the loading step.

4.4.2 Modeling of Orthogonal Cutting of AISI 4340 Steel

ABAQUS/Standard was used to model orthogonal metal cutting. The workpiece length was chosen to be 2.85 mm. The workpiece model has two sections; the chip and the remaining uncut sections. The depth of cut or feed was 0.2540 mm. An out-of-plane thickness of the

workpiece and tool of 10 mm was assumed in conjunction with the plane strain assumption in the model. A sharp cutting tool with a 20 degree rake angle and a 5 degree clearance angle was used as shown in Figure 4.5. An initial chip was selected to avoid possible numerical problems in ABAQUS due to mesh distortion that might occur during subsequent chip formation.

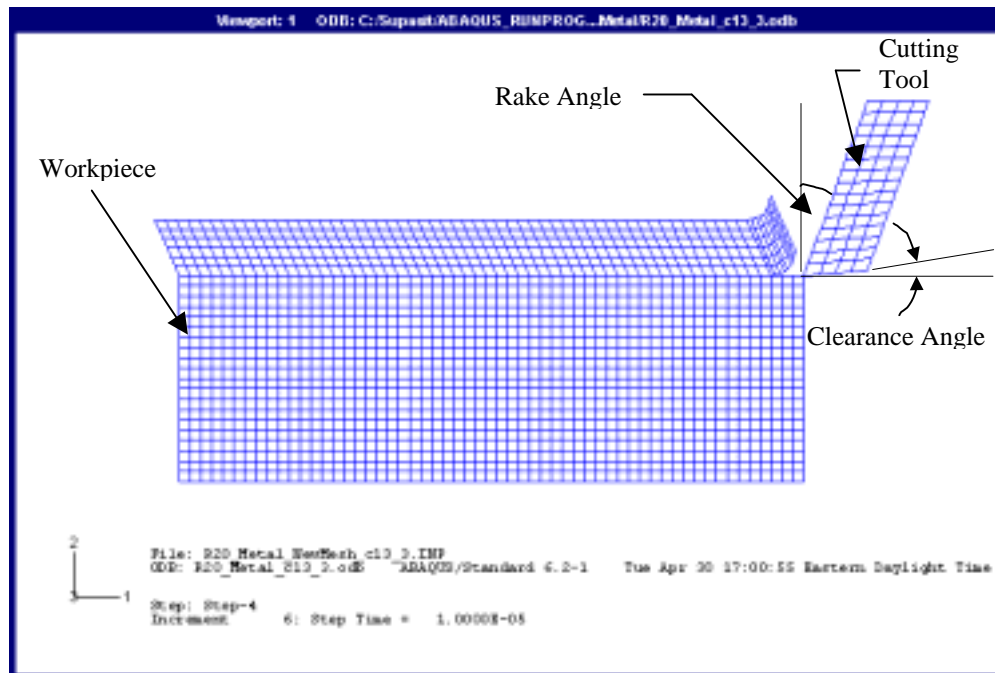


Figure 4.5 Initial mesh for the orthogonal cutting model of AISI 4340 steel.

The workpiece model contained a total of 1659 nodes and 1512 elements. The element was a two-dimensional, 4-node bilinear plane strain thermally coupled quadrilateral (CPE4T), which is a first-order, fully integrated element.

Using the same element type for the workpiece, the cutting tool consisted of 80 nodes and 60 elements. The high speed steel (HSS) tool was modeled with a modulus of elasticity of

2×10^{15} MPa. AISI 4340 steel was chosen as the workpiece material. A material model with temperature-dependent elastic-plastic behavior and isotropic hardening was used as shown in Tables 4.2 – 4.4. For the cutting model, the strain-rate property of AISI 4340 was assumed to be governed by the constitutive power law relationship described previously in equation (4.9).

Table 4.2 Temperature-dependent thermal expansion coefficients for AISI 4340 steel (Shet and Deng, 2000).

| Temperature (°C) | Thermal expansion coefficients ($\mu\text{m/m K}$) |
|------------------|--|
| 20 | 12.3 |
| 200 | 12.7 |
| 400 | 13.7 |
| 600 | 14.5 |

Table 4.3 Temperature-dependent elastic properties of AISI 4340 steel (Shet and Deng, 2000).

| Temperature (°C) | Elastic of Modulus (GPa) | Poisson's ratio |
|------------------|--------------------------|-----------------|
| 20 | 207 | 0.3 |
| 100 | 200 | 0.3 |
| 150 | 190 | 0.3 |
| 200 | 105 | 0.3 |
| 250 | 70 | 0.3 |
| 300 | 50 | 0.3 |
| 350 | 30 | 0.3 |

Table 4.4 Temperature-dependent elastic-plastic properties of AISI 4340 steel (Shet and Deng, 2000).

| Temperature (°C) | Flow stress (MPa) | Plastic strain (mm/mm) |
|------------------|-------------------|------------------------|
| 20 | 414 | 0.00 |
| 20 | 517 | 0.01 |
| 20 | 759 | 0.09 |
| 20 | 1100 | 0.90 |
| 100 | 409 | 0.00 |
| 100 | 512 | 0.01 |
| 100 | 754 | 0.09 |
| 100 | 1005 | 0.90 |
| 150 | 309 | 0.00 |
| 150 | 412 | 0.01 |
| 150 | 654 | 0.09 |
| 150 | 905 | 0.90 |
| 200 | 259 | 0.00 |
| 200 | 362 | 0.01 |
| 200 | 604 | 0.09 |
| 200 | 885 | 0.90 |
| 250 | 209 | 0.00 |
| 250 | 312 | 0.01 |
| 250 | 554 | 0.09 |
| 250 | 835 | 0.19 |
| 300 | 159 | 0.00 |
| 300 | 262 | 0.01 |
| 300 | 504 | 0.09 |
| 300 | 785 | 0.90 |

The left, right, and bottom surface boundaries of the workpiece shown in Figure 4.5 were constrained in all three translational degrees of freedom. In addition, the initial temperature was set to 20°C. The cutting tool was constrained to move horizontally to the left with a constant speed of 2.50 m/s. In the model, three slave/master contact pairs were defined; i.e., chip/workpiece, chip/tool, and workpiece/tool. A modified Coulomb friction coefficient of 0.20 was used along the chip/tool interface. When the shear stress of the chip at a contact point along the surface reaches the critical stress, then relative motion occurs. In contrast, a stick contact point condition is obtained when the shear stress value is less than the critical shear stress. The critical shear stress can be determined by (Hsieh, 1998):

$$\tau_c = \min(\mu p, \tau_{th}) \quad (4.10)$$

where τ_c = critical shear stress of the chip at a contact point along the chip/tool interface

μ = friction coefficient (in this model, $\mu = 0.20$)

τ_{th} = threshold stress related to material failure

(for AISI 4340 steel, $\tau_{th} = 549$ MPa)

p = normal pressure at a contact point along the chip/tool interface.

In the analysis procedure in ABAQUS/Standard, a static load condition was assumed in which the inertial forces were neglected. In metal machining, heat is generated in the primary and secondary shear zones. Friction along the chip/tool interface also generates

additional heating. A sufficient cutting distance was specified so that steady state cutting conditions were achieved.

Chip separation in the cutting model was accomplished with node debonding and a failure criterion option available in ABAQUS/Standard. To achieve this goal, initially bonded nodes were constructed along the chip/workpiece interface and the projected chip separation line. A critical stress criterion was used to determine when debonding of these nodes occurred, which was based on the value of a critical stress function at a specific distance ahead of the cutting tool. The critical stress function is given by (ABAQUS/Standard manual, 2001):

$$f = \sqrt{\left(\left(\frac{\sigma_n}{\sigma_f}\right)^2 + \left(\frac{\tau_n}{\tau_f}\right)^2\right)} \quad (4.11)$$

Where f = the critical stress function

σ_n = normal tensile stress (for compression, σ_n is zero) measured at a specific distance in front of the tool

σ_f = material failure stress under tensile mode

τ_n = shear stress measured at a specific distance

τ_f = material failure stress under shear mode.

When the value of f at a specific distance reaches the value of 1.00, the nodes along the separation line are released. In this research, a specific distance ranging from 0.05 to 0.08 mm was used. Note that the element length in the workpiece model was 0.05 mm. In addition, the failure stresses in tension and shear for AISI 4340 steel were assumed to be 948 and 548 MPa, respectively (Shet and Deng, 2000).

4.4.3 Modeling of Indentation of Elastomers

Using ABAQUS/Explicit, half-wedge indenters with a 5 degree clearance angle and varying tip edge radii and half-wedge angles were used to simulate indentation of elastomers. The initial finite element mesh of the workpiece and the indenter is shown in Figures 4.6 and 4.7. The workpiece height and width were chosen to be 2.85 and 1.07 mm, respectively. The workpiece model contained a total of 24341 nodes and 24000 elements. Element size was approximately 0.0107 mm. A two-dimensional, 4-node bilinear plane strain element with reduced integration (CPE4R) was used. The high speed steel (HSS) indenter was modeled with a modulus of elasticity of 2×10^5 MPa. The indenter was modeled as a rigid surface. The indenter was constrained to move vertically downward with a constant speed of 2.50 m/s. The right end and lower boundaries of the workpiece were constrained in all three translational degrees of freedom. A coulomb friction coefficient of 0.60 and 1.20 were used between the tool and the workpiece.

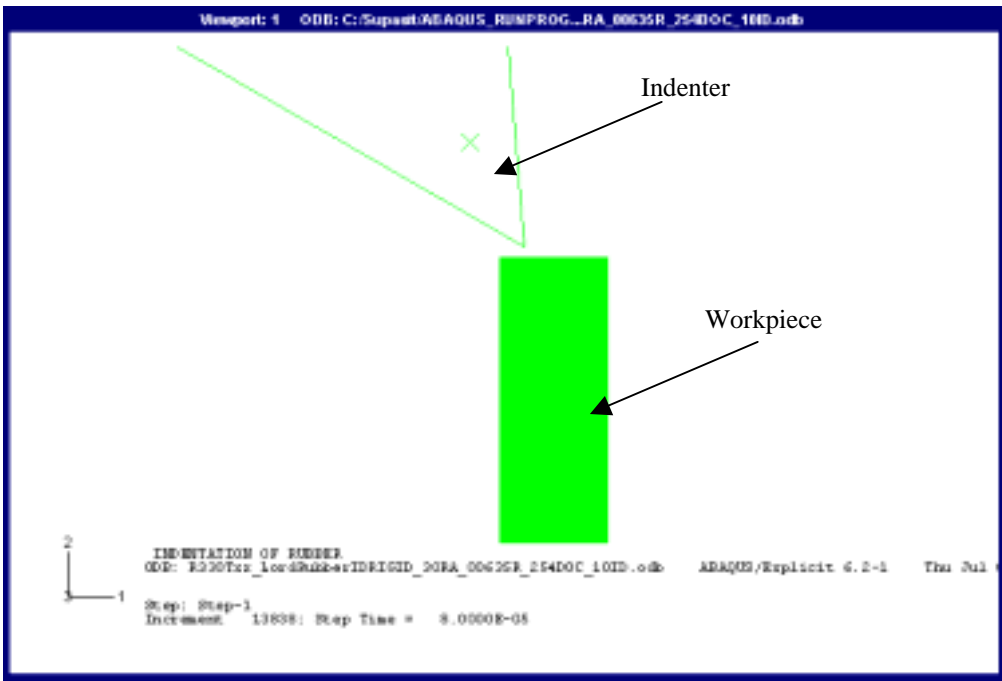


Figure 4.6 Initial mesh for half-wedge indentation model of elastomers.

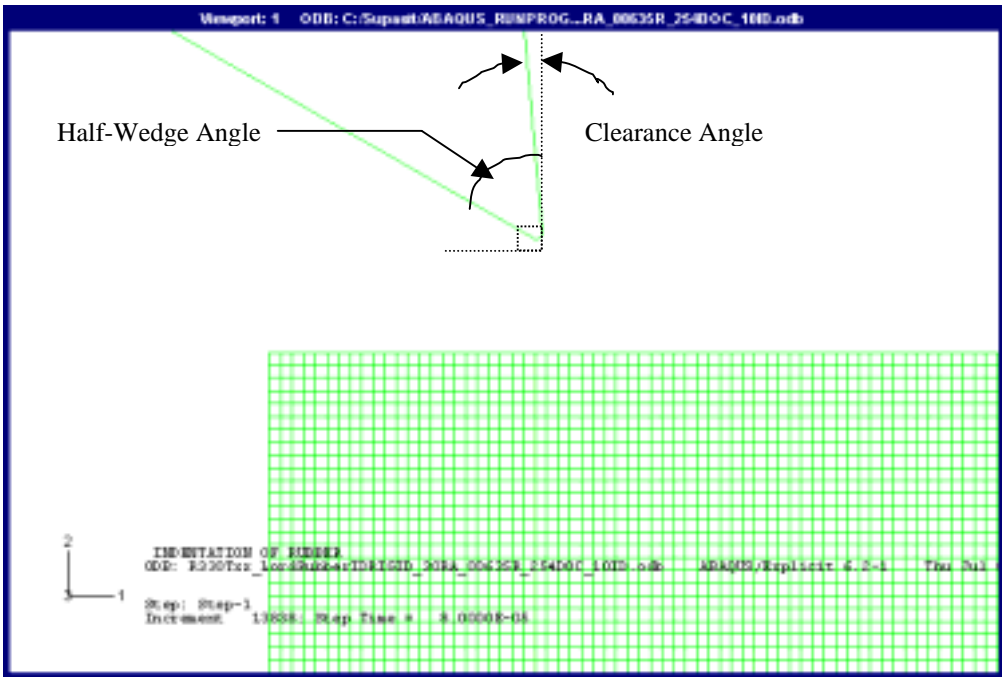


Figure 4.7 Initial mesh for half-wedge indentation model of elastomers (detailed view).

The elastomeric material used in this research was obtained from Lord Corporation (Compound A225P, Batch No. CS-02-003288). The uniaxial tensile stress – strain curve for the elastomer is shown in Figure 4.8. A mass density of 1104 kg/m^3 was used for the elastomer. The Ogden hyperelastic material model was used to simulate the elastomer workpiece.

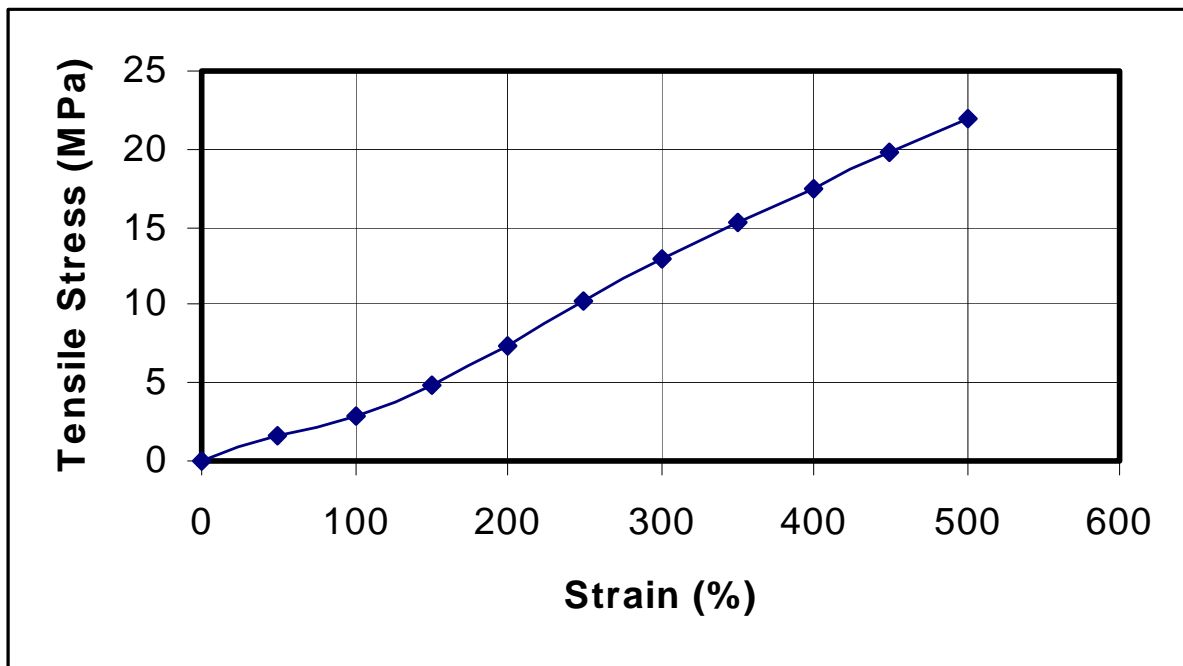


Figure 4.8 Uniaxial tensile stress-strain relationship for elastomer used in the wedge indentation model.

There are two methods to simulate a hyperelastic material model in ABAQUS. In the first, the coefficients for any strain energy density form can be entered directly. In the second method, stress-strain data can be input in tabular form and then a regression analysis is automatically performed in ABAQUS to determine the coefficients of the model. For an elastomer, three tests are usually conducted; i.e., uniaxial tension (and/or compression), equibiaxial (and/or compression), and planar tension or pure shear (and/or compression).

Schematics of these deformation modes for a hyperelastic material model are shown in Figures 4.9 – 4.11. Data corresponding to these three tests is recommended to obtain good characterization of hyperelastic material behavior. In addition, a volumetric tension (and/or compression) test is also recommended if the elastomer exhibits some compressibility.

The stress-strain relationships for three different tests can be developed using derivatives of the strain energy function with respect to the strain invariants (ABAQUS/Standard User's Manual, 2001). These relationships are defined in terms of the nominal stress (the force divided by the original undeformed area) and the nominal, or engineering strain. The deformation gradient, F , can be described in the principal directions of stretch as:

$$F = \begin{vmatrix} \lambda_1 & 0 & 0 \\ 0 & \lambda_2 & 0 \\ 0 & 0 & \lambda_3 \end{vmatrix} \quad (4.12)$$

where λ_1, λ_2 and λ_3 are the principal stretches (the ratios of current length to length in the original configuration in the principal directions of the material). The principal stretches, λ_i , are related to the principal nominal strains, ε_i , by:

$$\lambda_i = 1 + \varepsilon_i \quad (4.13)$$

Assuming incompressibility, $J = \det(F) = 1$; therefore, $\lambda_1 \lambda_2 \lambda_3 = 1$. The deviatoric strain invariants in terms of the principal stretches are given by:

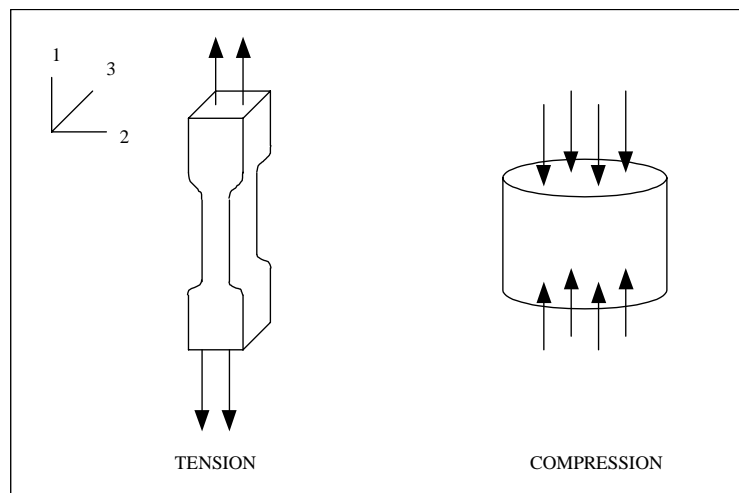


Figure 4.9 Schematic of the uniaxial deformation mode (ABAQUS/Standard User's Manual, 2001).

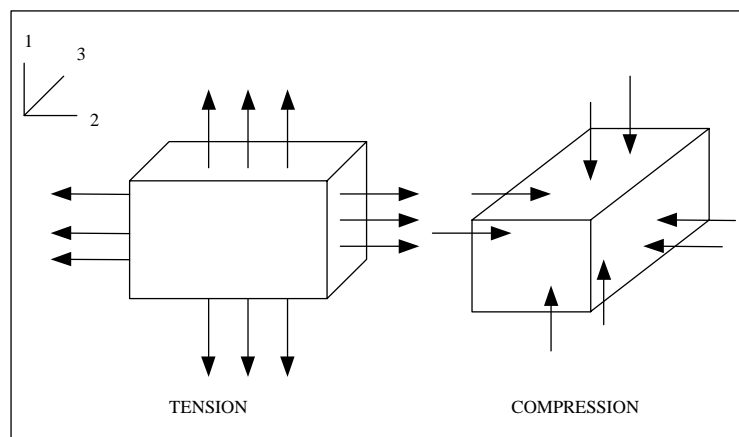


Figure 4.10 Schematic of the equi-biaxial deformation mode (ABAQUS/Standard User's Manual, 2001).

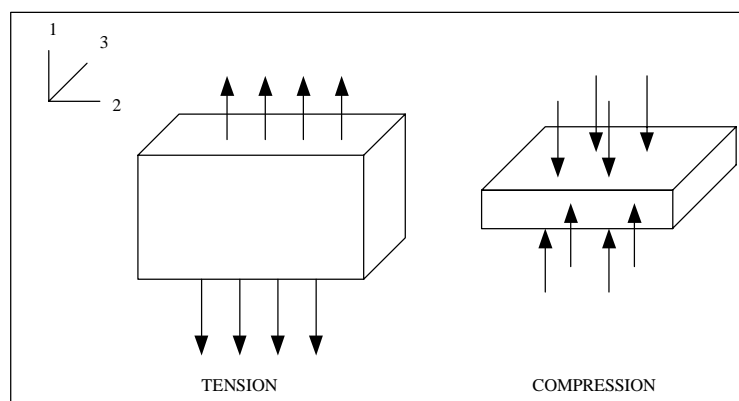


Figure 4.11 Schematic of the planar deformation mode (ABAQUS/Standard User's Manual, 2001).

$$I_1 = \lambda_1^2 + \lambda_2^2 + \lambda_3^2 \quad (4.14)$$

and

$$I_2 = \lambda_1^{-2} + \lambda_2^{-2} + \lambda_3^{-2} \quad (4.15)$$

The uniaxial deformation mode (Figure 4.9) is identified in terms of the principal stretches, λ_i , as:

$$\lambda_1 = \lambda_U \quad (4.16)$$

and

$$\lambda_2 = \lambda_3 = \frac{1}{\sqrt{\lambda_U}} \quad (4.17)$$

where λ_U is the stretch in the loading direction. The nominal strain is also defined by:

$$\varepsilon_U = \lambda_U - 1 \quad (4.18)$$

The principle of virtual work is used in order to derive the uniaxial nominal stress, T_U :

$$\delta U = T_U \delta \lambda_U \quad (4.19)$$

$$T_U = \frac{\partial U}{\partial \lambda_U} = 2(1 - \lambda_U^{-3}) \left(\lambda_U \frac{\partial U}{\partial I_1} + \frac{\partial U}{\partial I_2} \right) \quad (4.20)$$

The uniaxial tension test is the most common of all tests. A uniaxial compression test can be performed by loading a compression button between lubricated surfaces so any barreling in the button that could cause deviations from a homogeneous uniaxial compression stress-strain state can be avoided.

In the equi-biaxial test, the deformation mode (Figure 4.10) is characterized in terms of the principal stretches, λ_i , by:

$$\lambda_1 = \lambda_2 = \lambda_B \quad (4.21)$$

and

$$\lambda_3 = \frac{1}{\lambda_B^2} \quad (4.22)$$

where λ_B is the stretch in the two perpendicular loading directions. The nominal strain is also defined as:

$$\varepsilon_B = \lambda_B - 1 \quad (4.23)$$

Similarly, the principle of virtual work is used to determine the equi-biaxial nominal stress,

T_B :

$$\delta U = 2T_B \delta \lambda_B \quad (4.24)$$

$$T_B = \frac{1}{2} \frac{\partial U}{\partial \lambda_B} = 2(\lambda_B - \lambda_B^{-5}) \left(\frac{\partial U}{\partial I_1} + \lambda_B^2 \frac{\partial U}{\partial I_2} \right) \quad (4.25)$$

Typically, the equi-biaxial compression test is not often performed due to difficulties in the experimental setup. In contrast, an equi-biaxial tension test is usually conducted. In this test, a stress state with two equal tensile stresses and zero shear stress is applied. This state is usually achieved by pulling a square sheet in a biaxial testing machine.

Next, the planar deformation mode (Figure 4.11) is characterized in terms of the principal stretches, λ_i , as:

$$\lambda_1 = \lambda_s \quad (4.26)$$

and $\lambda_2 = 1 \quad (4.27)$

and $\lambda_3 = \frac{1}{\lambda_s} \quad (4.28)$

where λ_s is the stretch in the loading direction. Then, the nominal strain in the loading direction is:

$$\varepsilon_s = \lambda_s - 1 \quad (4.29)$$

This test is normally called a "pure shear" test since, in terms of logarithmic strains:

$$\varepsilon_1 = \ln \lambda_1 = -\ln \lambda_3 = -\varepsilon_3 \quad (4.30)$$

and $\varepsilon_2 = \ln \lambda_2 = 0 \quad (4.31)$

which corresponds to a state of pure shear at an angle of 45° to the loading direction.

The nominal planar stress, T_s , is found using the principle of virtual work:

$$\delta U = T_s \delta \lambda_s \quad (4.32)$$

$$T_s = \frac{\partial U}{\partial \lambda_s} = 2(\lambda_s - \lambda_s^{-3}) \left(\frac{\partial U}{\partial I_1} + \frac{\partial U}{\partial I_2} \right) \quad (4.33)$$

Note that the planar test data for determining material properties must be accompanied by the uniaxial and/or biaxial test data due to the non-uniqueness of its stress solution.

Note that if compressibility is introduced in the material model, D_i must be introduced for some hyperelastic models such as the Ogden model. It can be determined from a pure volumetric compression test of a specimen since volumetric tension tests are more difficult to conduct. In a pure volumetric test $\lambda_1 = \lambda_2 = \lambda_3 = \lambda_v$; therefore, $I_1 = I_2 = 3$ and $J = \lambda_v^3 = V/V_0$ (the volume ratio). Using the polynomial form of the strain energy potential, the total pressure stress on the specimen can then be obtained as:

$$p = -\left(\frac{\sigma_1 + \sigma_2 + \sigma_3}{3}\right) = -\sum_{i=1}^N 2i \frac{1}{D_i} (\lambda_v^3 - 1)^{2i-1} \quad (4.34)$$

4.4.4 Modeling of Orthogonal Cutting of Elastomers

ABAQUS/Standard was used to model orthogonal cutting of elastomers. The workpiece length was chosen to be 2.85 mm. The workpiece model has two sections; the chip and the remaining uncut sections. The depth of cut or feed was 0.1270 mm. The out-of-plane thickness of the workpiece and tool was assumed to be 10 mm in conjunction with the plane strain assumption. A sharp cutting tool with a 30 degree rake angle and 5 degree clearance angle was used as shown in Figure 4.12. Similar to the orthogonal metal cutting model, an initial chip was introduced to avoid possible numerical problems in ABAQUS due to mesh distortion that might occur during chip formation.

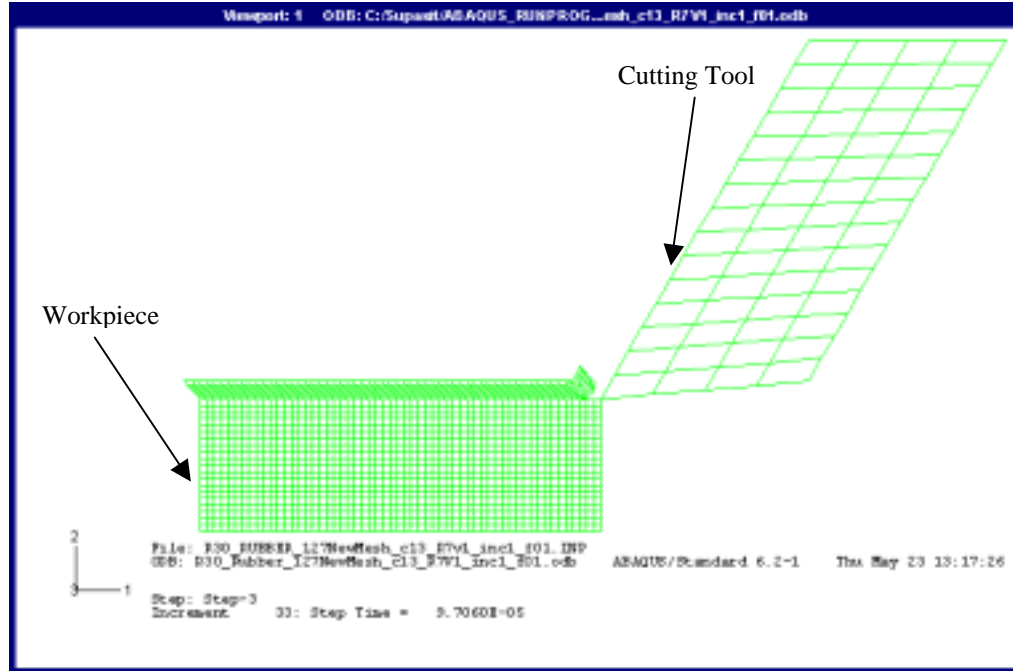


Figure 4.12 Initial mesh for the orthogonal cutting model of elastomers.

The workpiece model contained a total of 1659 nodes and 1512 elements. The element was a two-dimensional, 4-node bilinear plane strain thermally coupled quadrilateral (CPE4HT), which is a first-order, fully integrated element.

The cutting tool consisted of 80 nodes and 60 elements. The high speed steel (HSS) tool was modeled with a modulus of elasticity of 2×10^{15} MPa. The elastomer was modeled with Ogden's strain energy density function where the associated material parameters were adopted as follows (Finney and Kumar, 1988).

$$W = \sum_{i=1}^3 \sum_{j=1}^N \frac{c_j \left(\lambda_i^{b_j} - 1 \right)}{b_j} \quad (4.35)$$

Where

- W = the strain energy function
- λ = the extension ratio
- N = number of polynomial term used
- b_j, c_j = material constants.

Based on empirical data (Finney and Kumar, 1988), the following values for the material constants were used:

- $b_1 = 0.008966$ MPa
- $b_2 = 0.034483$ MPa
- $b_3 = -0.013793$ MPa
- $c_1 = 0.618069$ MPa
- $c_2 = 0.001177$ MPa
- $c_3 = -0.009811$ MPa.

The relationship between the uniaxial tensile stress and the extension ratio used in their investigation for Ogden's strain energy density function is shown in Figure 4.13. A mass density of 1104 kg/m^3 was used.

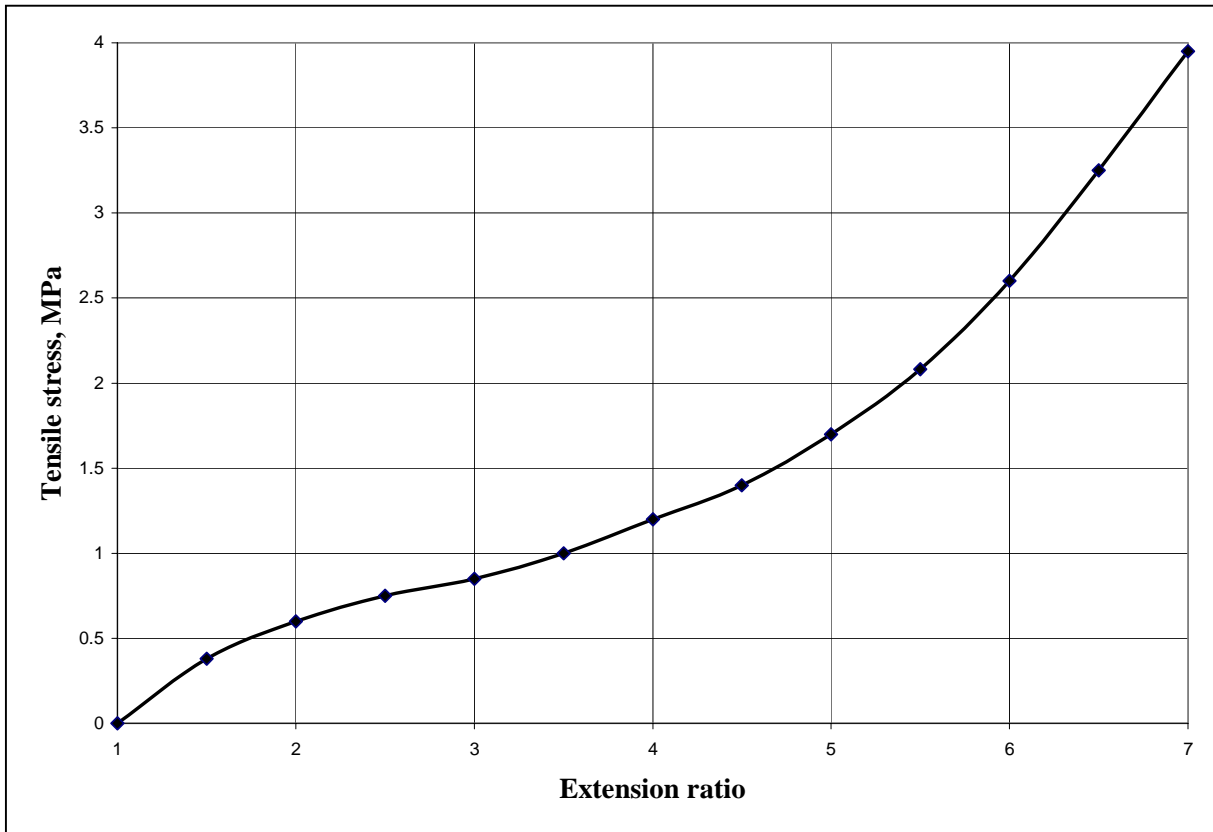


Figure 4.13 Uniaxial tensile stress - extension ratio relationship used in orthogonal cutting model of elastomers (Finney and Kumar, 1988).

The left, right, and bottom boundaries of the workpiece shown in Figure 4.12 were constrained in all three translational degrees of freedom. The initial temperature was set as 20°C. Similar to the metal cutting model, the cutting tool was constrained to move horizontally to the left with a constant speed of 2.50 m/s. Similarly, three slave/master contact pairs were defined. A modified Coulomb friction coefficient of 0.10 was used along the chip/tool interface. When the shear stress of the chip at the tip of the tool reaches the critical stress, as determined by equation (4.10), relative motion occurs. Debonding of the nodes occurs when the value of f at a specific distance reaches 1.00 along the separation line.

For the elastomer workpiece, a specific distance of 0.001 mm was used, and the failure stresses in tension and shear were assumed to be 1.0 and 0.577 MPa, respectively.

5. SIMULATIONS OF ORTHOGONAL CUTTING AND WEDGE INDENTATION

As described in Chapter 4, half-wedge indentation models for both AISI 4340 steel and elastomers have been developed in this research. In addition, an orthogonal metal cutting model was developed for AISI 4340 steel to demonstrate the transition of incipient chip formation in indentation. In this chapter, these simulation results are discussed.

5.1 Simulations of AISI 4340 Steel

5.1.1 Orthogonal Cutting Simulation

An orthogonal cutting simulation of AISI 4340 steel with a sharp cutting tool with a 20 degree rake angle and 5 degree clearance angle was conducted. Simulations were performed for a 0.2540 mm depth of cut and a cutting speed of 2.50 m/s. Figure 5.1 shows the finite element mesh of the initial and final configurations of the cutting tool. The workpiece contained a total of 1659 nodes and 1512 elements which were two-dimensional four-node bilinear plane strain elements.

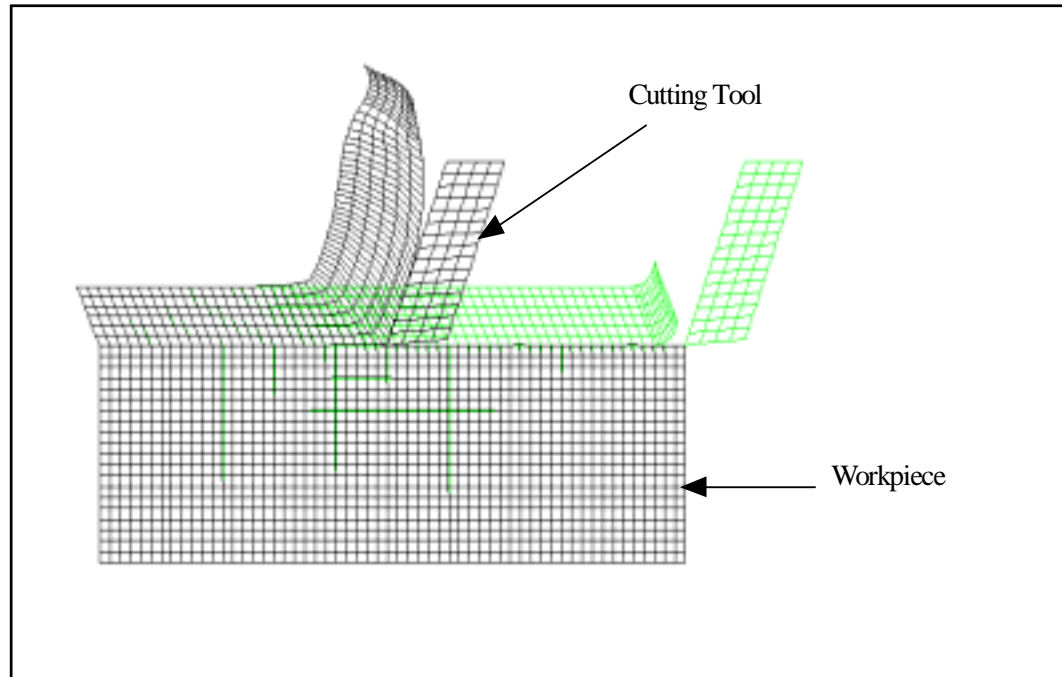


Figure 5.1 Undeformed and deformed configurations of the finite element mesh.

Von Mises stress contours at the early and final stages of the cutting simulation are shown in Figures 5.2 and 5.3. It can be seen that as the cutting tool moves into the workpiece, the maximum von Mises stresses extend continuously from the point of initial chip separation to the free surface of the chip along the shear plane. Figures 5.4 and 5.5 show Tresca stress contours from an early to final stage in which the chip is fully formed. Note that Tresca stress is defined as twice the maximum shear stress. Therefore, the contours of maximum shear stress shown in these figures demonstrate that chip formation is due to shear deformation that occurs in the primary shear zone.

Normal stress is defined as the stress perpendicular to the tool movement. Figures 5.6 and 5.7 show the normal stress contours in the vicinity of a tool tip. These figures demonstrate that although chip formation is primarily a shear deformation process, a tensile stress is

necessary for chip separation to occur. The strain energy density is defined as the amount of energy stored elastically at a given state of strain. As previously mentioned in Chapter 2, the strain energy density has been used to determine the various modes of fracture of elastomers such as tearing. Figures 5.8 and 5.9 show the strain energy density at the integration point with respect to the current volume of each element at the beginning and final stages of the simulation. Note that the SI units for strain energy density are Joules/cubic meter (J/m^3 or $\text{N}\cdot\text{m/m}^3$). This is equivalent to the Pascal unit of N/m^2 which will be used throughout this dissertation so that strain energy density can be plotted with the same units as stress. These figures show that there are two areas for which the strain energy density is large. Recall that the strain energy density is a function of the stress and strain. Therefore, the maximum strain energy density occurs in the primary and secondary shear zones where the shear stress and strain are greatest due to shear deformation in forming the chip and friction along the tool/chip interface.

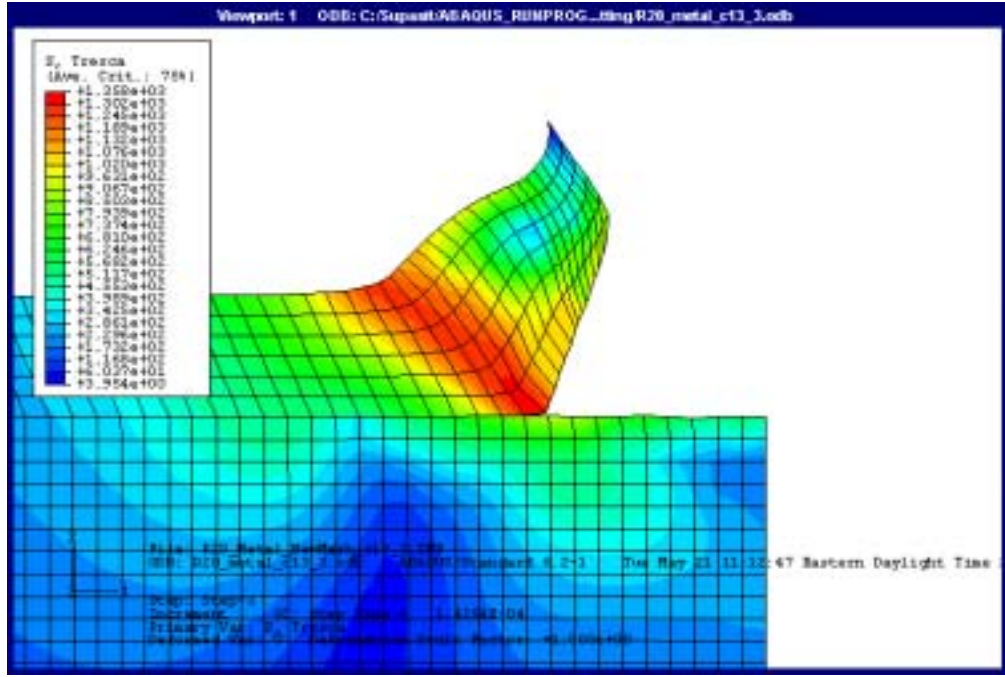


Figure 5.4 Tresca stress contours (MPa) at early configuration (analysis step 3, increment 60).

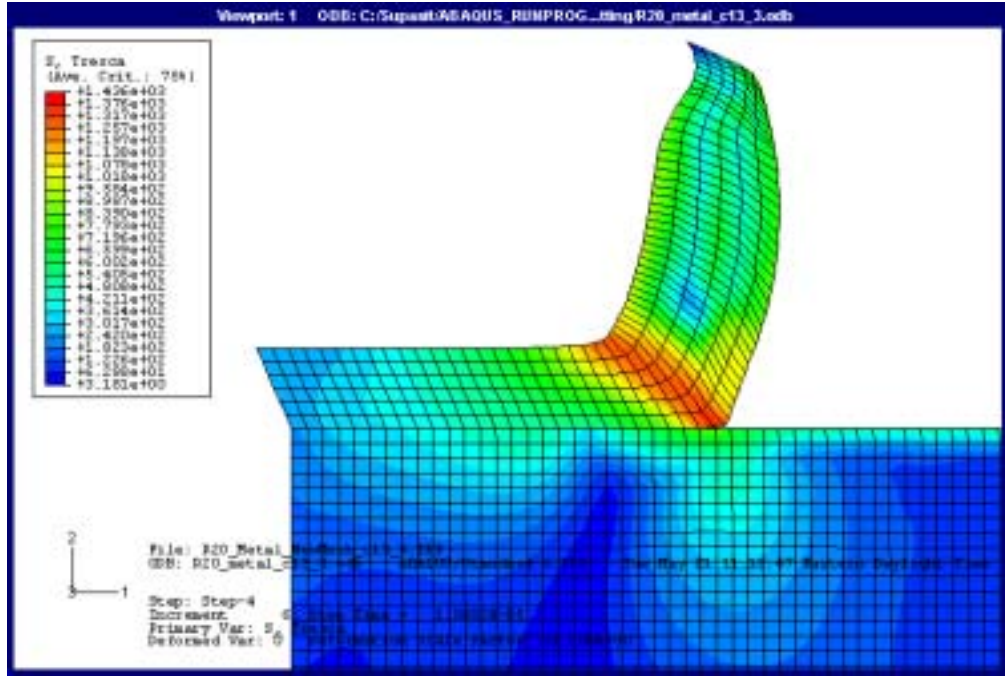


Figure 5.5 Tresca stress contours (MPa) at final configuration (analysis step 4, increment 6).

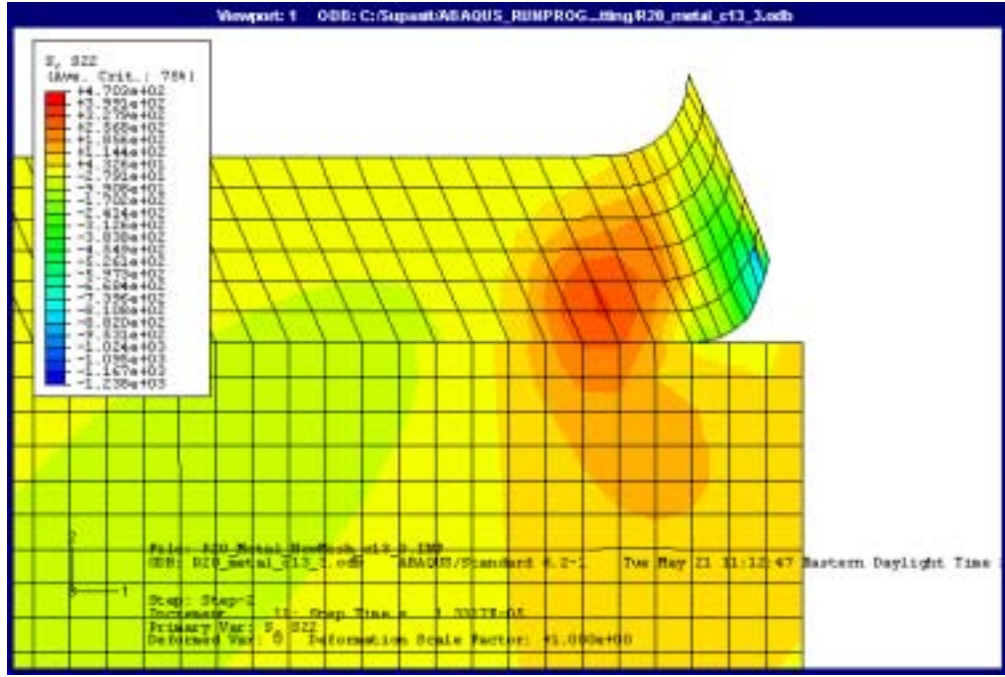


Figure 5.6 Normal stress contours (MPa) at early configuration (analysis step 2, increment 11).

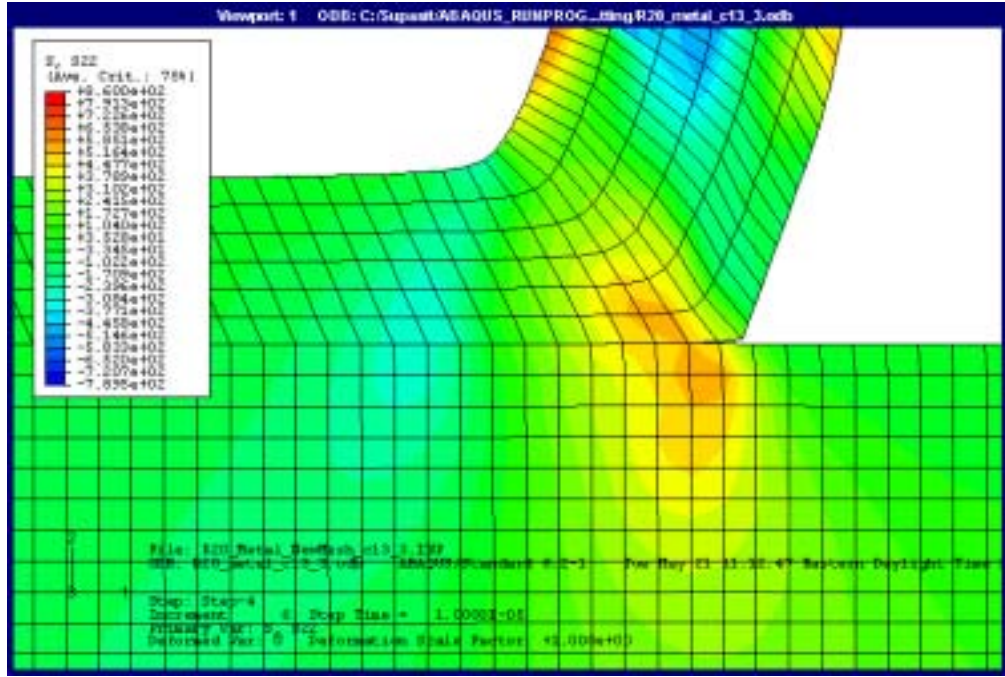


Figure 5.7 Normal stress contours (MPa) at final configuration (analysis step 4, increment 6).

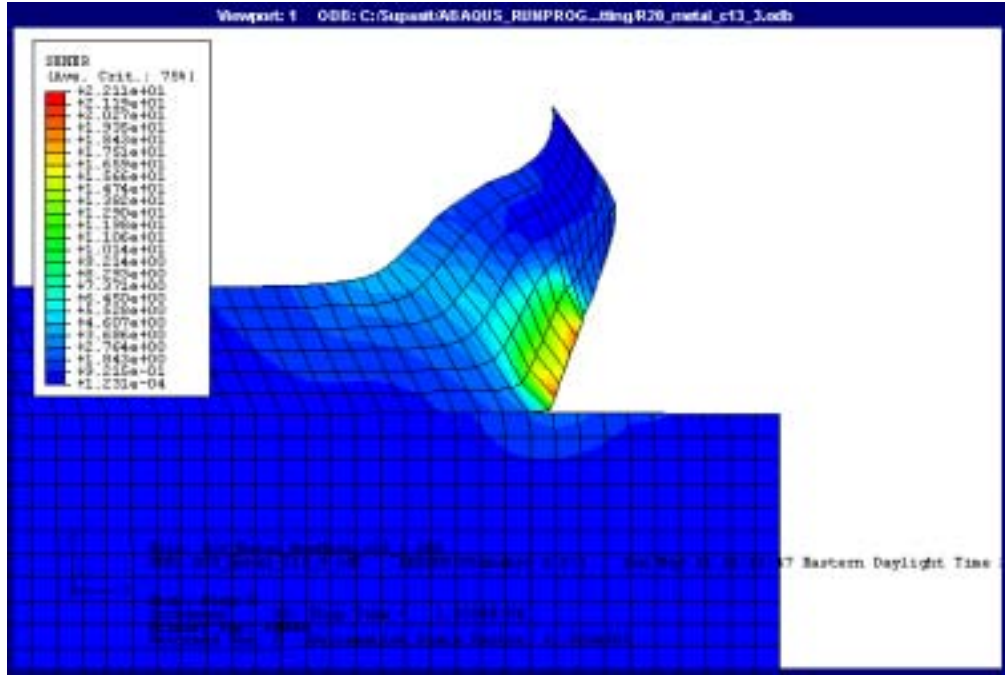


Figure 5.8 Strain energy density contours (MPa) at early configuration (analysis step 3, increment 60).

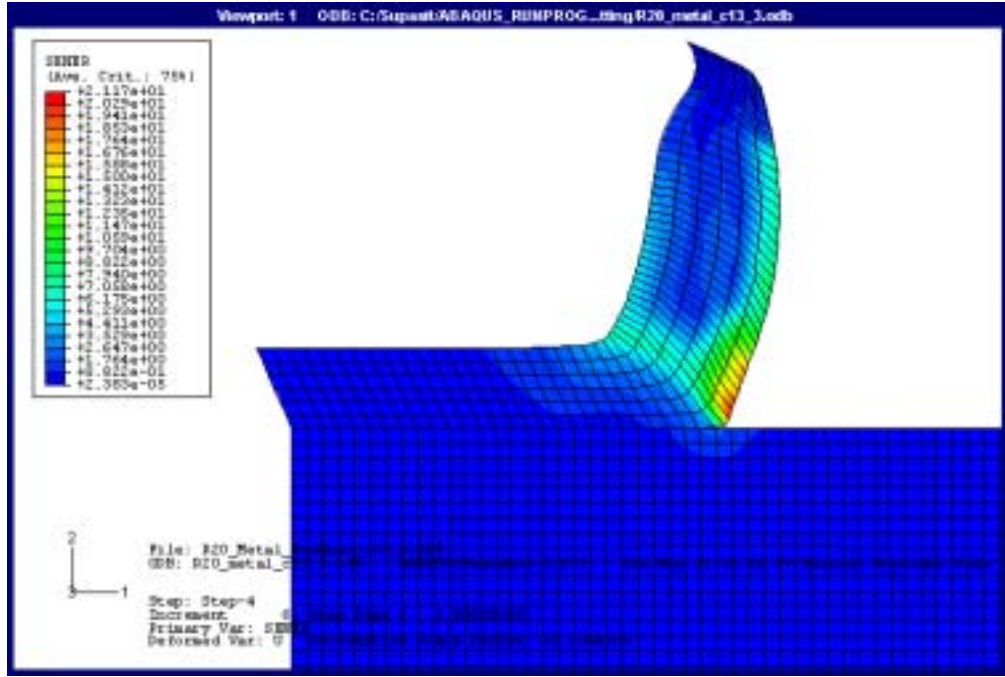


Figure 5.9 Strain energy density contours (MPa) at final configuration (analysis step 4, increment 6).

5.1.2 Wedge Indentation Simulation with a 70 degree Half-Wedge Angle

A wedge indentation simulation of AISI 4340 steel with a sharp indenter with a 70 degree half-wedge angle, 0.2540 mm depth of cut and downward vertical speed of 2.50 m/s was conducted. A detailed description of the model was presented in Chapter 4. Figure 5.10 shows the initial finite element mesh of the model. The workpiece contained a total of 6171 nodes and 6000 elements. Two-dimensional, four-node bilinear plane strain elements were used for the workpiece.

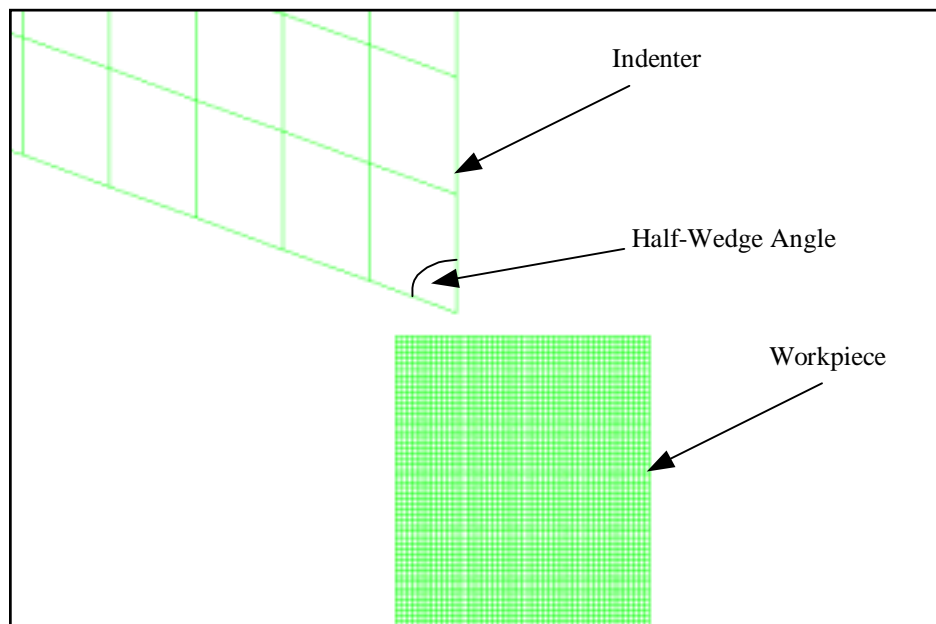


Figure 5.10 Undeformed configuration of the finite element mesh for a half-wedge indenter angle of 70 degrees.

As the indenter is advanced into the workpiece from 0.02 mm to 0.05 mm, a distinct zone develops under the indenter tip to the free edge of the workpiece as shown in Figures 5.11 and 5.12. Figures 5.13 and 5.14 show Tresca stress contours for both indentation depths of 0.02 and 0.05 mm. The gray zone shown in Figures 5.15 and 5.16 represents a Tresca stress of 478 MPa or greater. Recall that the Tresca stress is defined as twice the maximum shear stress. Note that the yield strength of AISI 4340 steel is 414 MPa so the shear strength is 239 MPa. Therefore, these figures show that a plastic shear zone extends from the indenter tip to the free surface of the workpiece. This correlates well with the cutting simulation results in section 5.1.1 in which shear deformation is the primary mechanism for chip formation.

Figures 5.17 and 5.18 show the strain energy density contours in the workpiece. In contrast to the von Mises and Tresca stresses, the maximum strain energy density contours do not show a distinct deformation zone, but rather a concentrated area under the indenter tip. The strain energy density distribution shown in this section will be used to compare with the strain energy density for wedge indentation of elastomers in the following section.

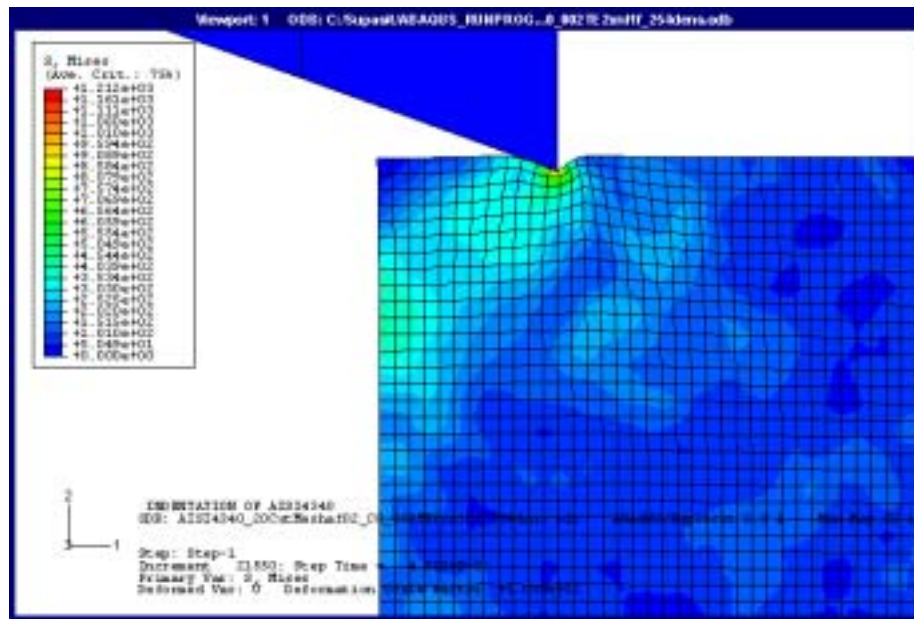


Figure 5.11 Von Mises stress contours (MPa) at an indentation depth of 0.02 mm for a half-wedge indenter angle of 70 degrees.

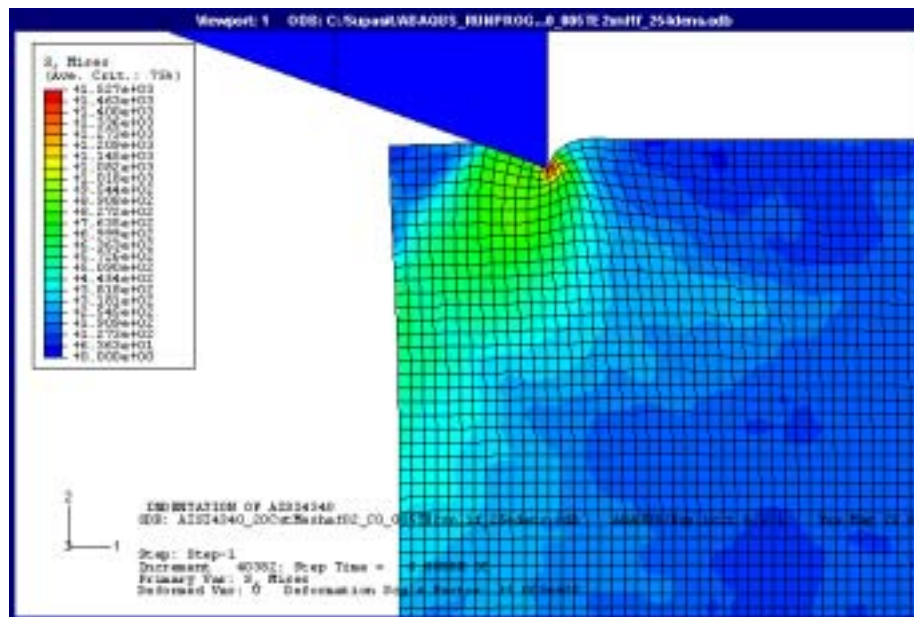


Figure 5.12 Von Mises stress contours (MPa) at an indentation depth of 0.05 mm for a half-wedge indenter angle of 70 degrees.

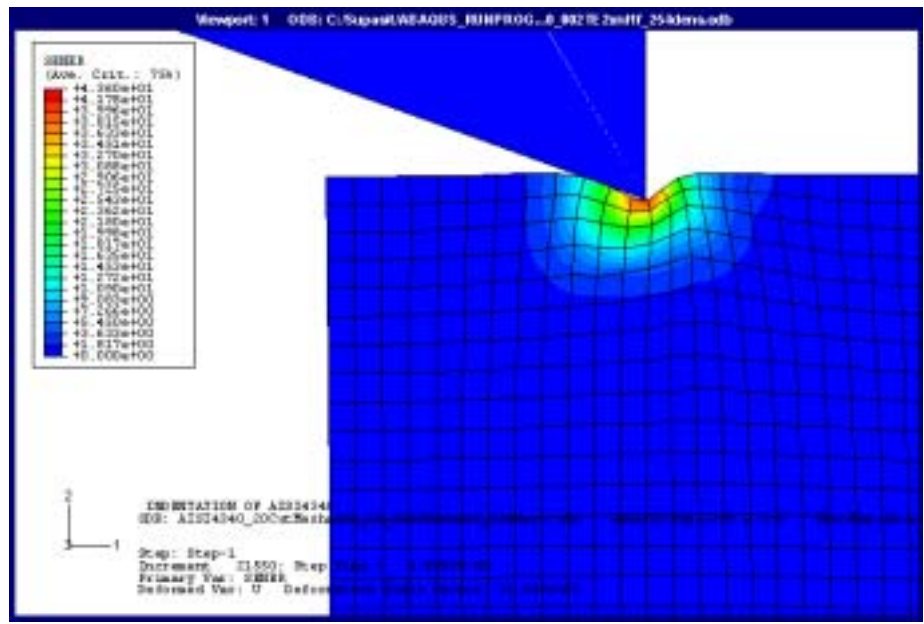


Figure 5.17 Strain energy density contours (MPa) at an indentation depth of 0.02 mm for a half-wedge indenter angle of 70 degrees.

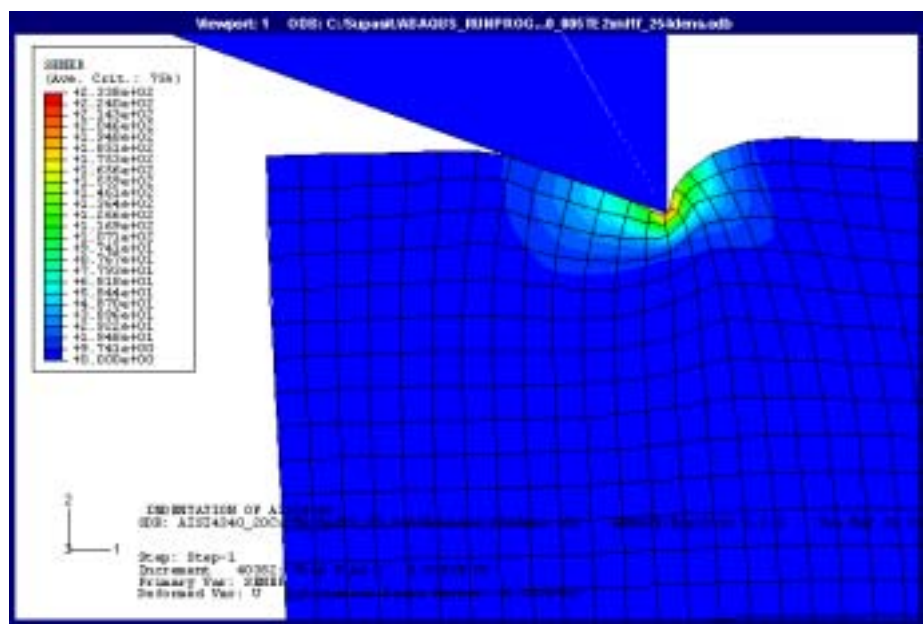


Figure 5.18 Strain energy density contours (MPa) at an indentation depth of 0.05 mm for a half-wedge indenter angle of 70 degrees.

5.2 Simulations of Indentation of Elastomers

Simulations of wedge indentation of elastomers were performed to determine the conditions for which incipient chip formation occurs. The effects of various indentation parameters on the deformation of elastomers were investigated. These include the indenter half-wedge angle, edge radius of the indenter, distance to the free edge of the workpiece, friction coefficient between the indenter and workpiece, boundary conditions within the workpiece, and the indentation depth. Note that the elastomeric workpiece used in these indentation simulations consisted of 24231 nodes and 24000 elements, which were two-dimensional, four-node bilinear elements. Because a typical friction coefficient between rubber and steel is in the range from 0.50 to 1.30 (Advanced Elastomer Systems, 1998), a friction coefficient of 0.60 and 1.20 was used in this research. Table 5.1 summarizes the operating conditions.

In addition, it has been shown that fixture design can influence the resulting machined surface finish for end milling of elastomers (Shih, Lewis et al. to be published). To study this effect for turning, various boundary conditions were imposed within the workpiece. For a boundary condition Type 1, the right and lower ends of the workpiece were constrained in all translational degrees of freedom. For a boundary condition Type 2, additional zero horizontal displacement constraints were applied to the workpiece at a distance of 0.0635 mm to the right of the indenter tip. This corresponds to the smaller feed. This boundary condition simulates the effect of a more rigid fixture as compared to the Type 1 boundary condition.

Table 5.1 Summary of operating conditions for wedge indentation simulations of elastomers.

| | |
|---|---------------------|
| Half-wedge angle | 40, 60, 80 degrees |
| Clearance angle | 5 degrees |
| Edge radius of indenter tip | 0.00635, 0.01270 mm |
| Feed (distance between indented tip and free edge of workpiece) | 0.0635, 0.2540 mm |
| Friction coefficient between workpiece and indenter | 0.60, 1.20 |
| Downward vertical speed of indenter | 2.5 m/s |
| Indentation depth | 0.10, 0.20 mm |
| Boundary condition type specified on workpiece | Types 1 and 2 |

As previously discussed in Chapter 2, various output variables of stress, strain, and strain energy density were carefully considered as possible indicators of the machinability of elastomers. Using these variables, operating conditions required to achieve a smooth elastomer surface can be identified.

Based on the indentation simulations of AISI 4340 steel in the previous chapter, it was shown that a high tensile normal stress in the vicinity of the separation point is required for chip formation to occur. In addition, the maximum principal stress must occur at a point that will allow the chip to cleanly separate from the machined workpiece surface. It has been found that in metal cutting, the chip separation point is approximately located at a distance of half

the edge radius from the tool clearance edge. Using this concept for elastomers, chip separation must occur at this point if a chip is to be cleanly removed from the workpiece to produce a smooth machined surface. In addition, a sufficiently large concentration of strain energy density must occur at the tip of the indenter. Note that the strain energy density is defined at the integration point at the center of each element with respect to the element volume.

In the following sections, the effects of the parameters shown in Table 5.1 on the machinability of elastomers are discussed. Table 5.2 summarizes six cases that were investigated. In this discussion, the normal stress perpendicular to the indenter movement, and the maximum principal stress were used to characterize the material response in the vicinity of the indenter tip. In addition, the strain energy density was also used because, as mentioned in Chapter 2, the strain energy density (equation 2.13) is used to characterize rubber for various failure modes such as tearing. Therefore, it was also considered to be an important parameter for characterizing incipient chip formation in indentation of elastomers.

Table 5.2 Summary of operating conditions for evaluating various effects on elastomer machinability.

| Case No. | Indenter half-wedge angle (degrees) | Indenter tip edge radius (mm) | Feed (mm) | Friction Coefficient | Indentation Depth (mm) | Boundary conditions specified for workpiece |
|----------|-------------------------------------|-------------------------------|-----------|----------------------|------------------------|---|
| 1 | 80 | 0.00635 | 0.0635 | 0.60 | 0.10 | Type 1 |
| 2 | 40 | 0.00635 | 0.0635 | 0.60 | 0.10 | Type 1 |
| 3 | 40 | 0.01270 | 0.0635 | 0.60 | 0.10 | Type 1 |
| 4 | 40 | 0.00635 | 0.2540 | 0.60 | 0.10 | Type 1 |
| 5 | 40 | 0.00635 | 0.0635 | 1.20 | 0.10 | Type 1 |
| 6 | 40 | 0.00635 | 0.0635 | 0.60 | 0.10 | Type 2 |

5.2.1 Wedge Indentation for a 80 degree Half-Wedge Indenter (Case 1)

Figure 5.19 shows the finite element mesh for both the undeformed and deformed configurations for an indenter with a half-wedge angle of 80 degrees. This indenter has a tip edge radius of 0.00635 mm. The distance from the tip to the free edge is 0.0635 mm, which corresponds to a feed of 0.0635 mm. A friction coefficient of 0.60 was applied along the indenter/workpiece interface, and the indenter was indented to a depth of 0.10 mm.

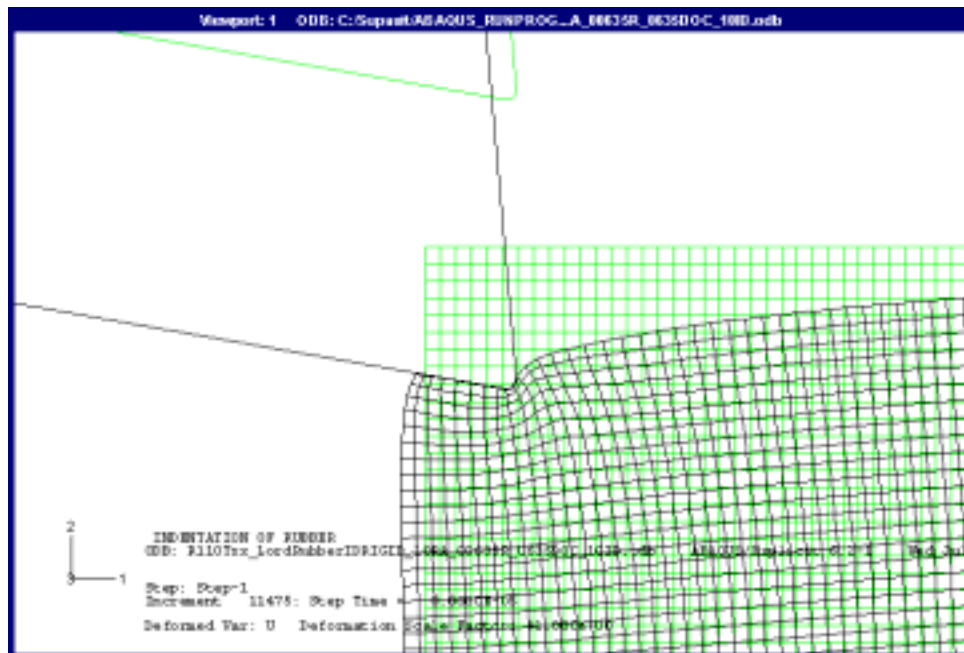


Figure 5.19 Deformed and undeformed configurations of the finite element mesh for a half-wedge angle of 80 degrees, tip edge radius of 0.00635 mm, feed of 0.0635 mm, friction coefficient of 0.60, and indentation depth of 0.10 mm.

As shown in Figure 5.19, there is significant lateral expansion of the workpiece of approximately two elements. Figures 5.20 and 5.21 show Tresca stress contours under the indenter tip. Note that the Tresca stress represents twice the maximum shear stress. It can be seen that the maximum Tresca stress contour does not extend to the free edge, but it rather expands vertically downward under the indenter tip. Therefore, in contrast to metal indentation, shear deformation is not the primary mechanism for incipient chip formation of elastomers. Figures 5.22 and 5.23 show normal stress contours and maximum principal stress contours are shown in Figure 5.24. Both the normal and maximum principal stresses are compressive in the vicinity of the separation point. The negative stresses are in element numbers 23908 and 23909. Figure 5.25 shows the strain energy density contours under the indenter tip. The maximum strain energy density of 2 MPa occurs at the workpiece under the indenter tip (element number 23909). Therefore, a chip will not cleanly separate from the workpiece because a compressive normal stress occurs at the separation point. Instead, widespread deformation of the workpiece occurs resulting in tearing and a rough surface finish. This result is consistent with the orthogonal cutting tests described in Chapter 3. Recall that it was shown that a rough surface finish and corresponding discontinuous chips occurred for a tool with a rake angle of 10 degrees and a feed of 0.0635 mm. The chips are shown in Figure 3.4 and the corresponding surface finishes are shown in Figure 3.5. Note that an indenter with a half-wedge angle of 80 degrees is equivalent to a cutting tool with a rake angle of 10 degrees.

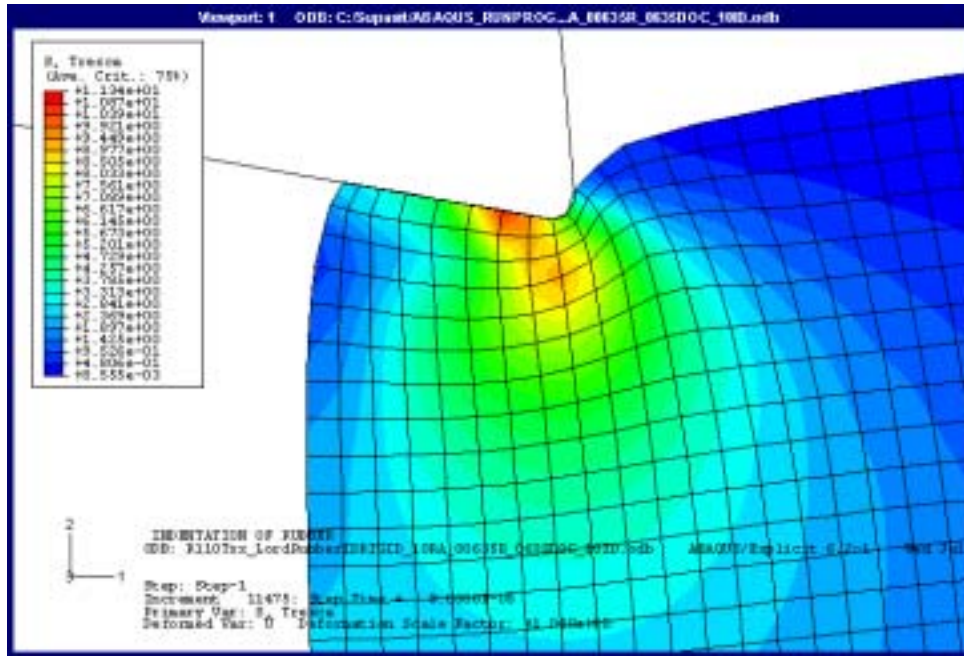


Figure 5.20 Tresca stress contours (MPa) for a half-wedge angle of 80 degrees, tip edge radius of 0.00635 mm, feed of 0.0635 mm, friction coefficient of 0.60, and indentation depth of 0.10 mm.

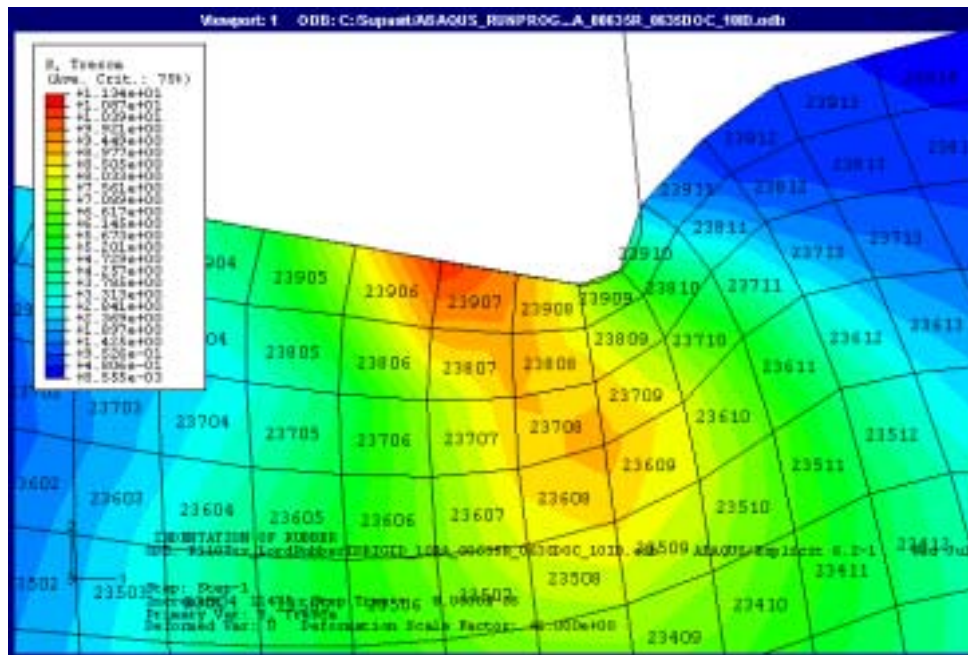


Figure 5.21 Detailed view of Tresca stress contours (MPa) for a half-wedge angle of 80 degrees, tip edge radius of 0.00635 mm, feed of 0.0635 mm, friction coefficient of 0.60, and indentation depth of 0.10 mm.

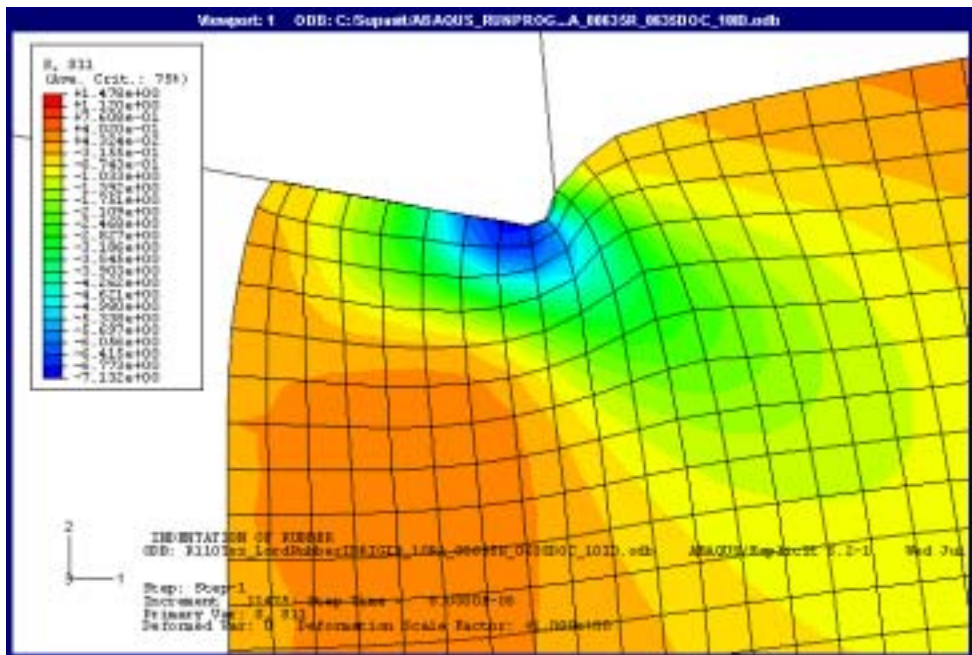


Figure 5.22 Normal stress contours (MPa) for a half-wedge angle of 80 degrees, tip edge radius of 0.00635 mm, feed of 0.0635 mm, friction coefficient of 0.60, and indentation depth of 0.10 mm.

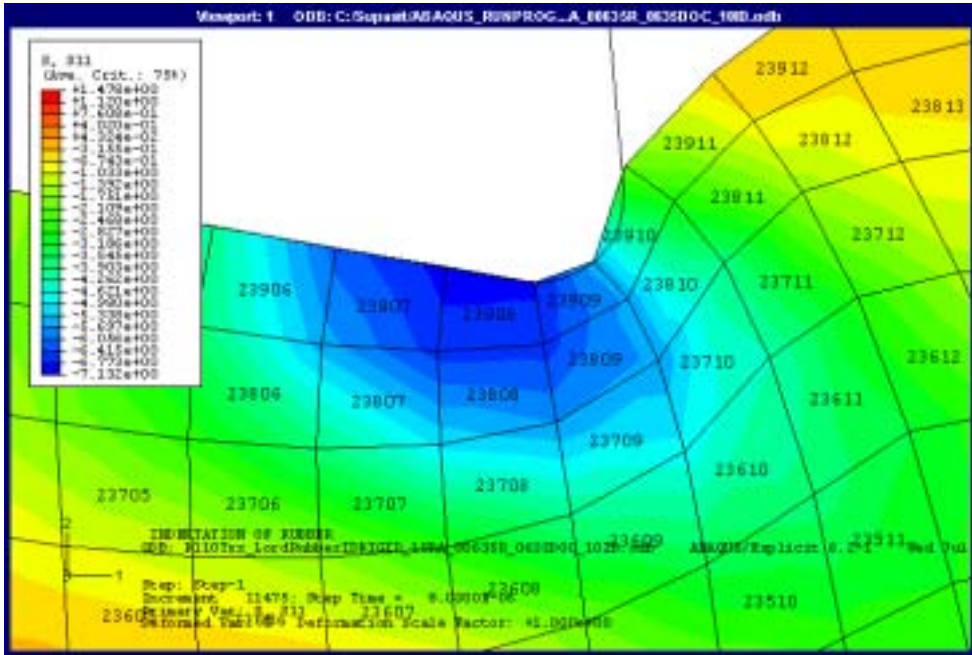


Figure 5.23 Detailed view of normal stress contours (MPa) for a half-wedge angle of 80 degrees, tip edge radius of 0.00635 mm, feed of 0.0635 mm, friction coefficient of 0.60, and indentation depth of 0.10 mm.

5.2.2 Wedge Indentation for a 40 degree Half-Wedge Indenter (Case 2)

The effect of the indenter half-wedge angle on the machinability of elastomers was investigated in this research. Figure 5.26 shows the finite element mesh for both the undeformed and deformed configurations for an indenter with a half-wedge angle of 40 degrees. An indenter tip edge radius of 0.00635 mm was used with a feed of 0.0635 mm and a friction coefficient of 0.60 for an indentation depth of 0.10 mm.

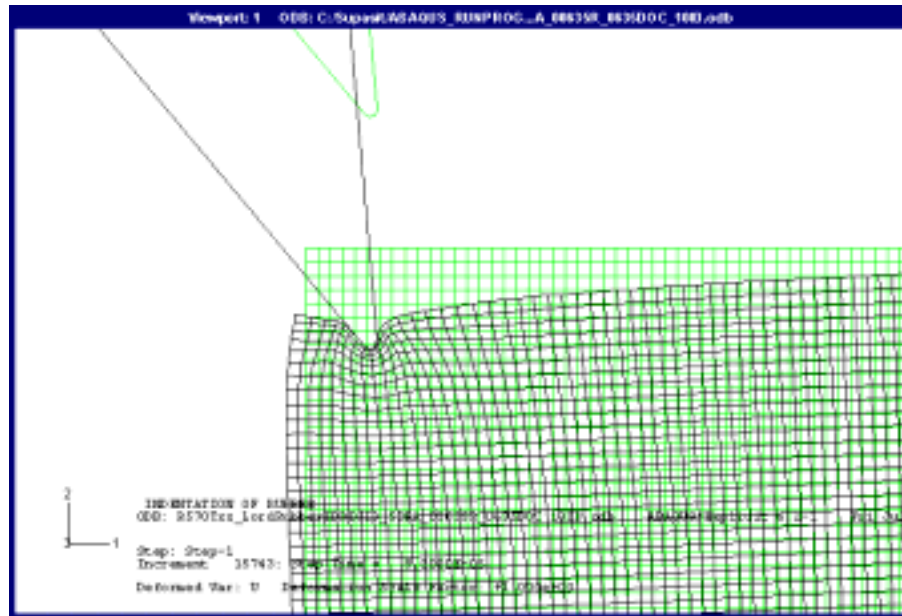


Figure 5.26 Deformed and undeformed configurations of the finite element mesh for a half-wedge angle of 40 degrees, tip edge radius of 0.00635 mm, feed of 0.0635 mm, friction coefficient of 0.60, and indentation depth of 0.10 mm.

Due to the small included angle of the indenter, the workpiece was highly deformed in the direction of the indenter movement. As a result, the 40 degree indenter produced less lateral expansion as compared to the 80 degree half-wedge indenter shown in Figure 5.19. The Tresca stress contours are shown in Figures 5.27 and 5.28. This distribution is similar to that for the 80 degree half-wedge angle. The Tresca stress did not extend to the free edge of the workpiece, but it expanded vertically downward under the indenter tip. Because the Tresca stress is twice the maximum shear stress, this demonstrates that shear deformation is not the primary mechanism of incipient chip formation.

The normal stress for the 40 degree indenter is shown in Figures 5.29 and 5.30. In contrast to the previous case, the maximum tensile normal stress occurred at approximately half of the tip edge radius from the clearance face. Figure 5.31 shows a similar result for the maximum principal stress. The resulting maximum strain energy density exceeds 8 MPa and it is located near the indenter tip where chip separation is likely to occur as shown in Figure 5.32. Based on the conditions described for chip formation, the chip should cleanly separate from the workpiece. These results correlate well with the orthogonal cutting tests conducted in Chapter 3. A relatively smooth surface finish and corresponding continuous chips were produced for a tool with a rake angle of 50 degrees and a feed of 0.0635 mm. The chips are shown in Figure 3.4 and the corresponding surface finish is shown in Figure 3.5. Note that an indenter with a half-wedge angle of 40 degrees is equivalent to a cutting tool with a rake angle of 50 degrees.

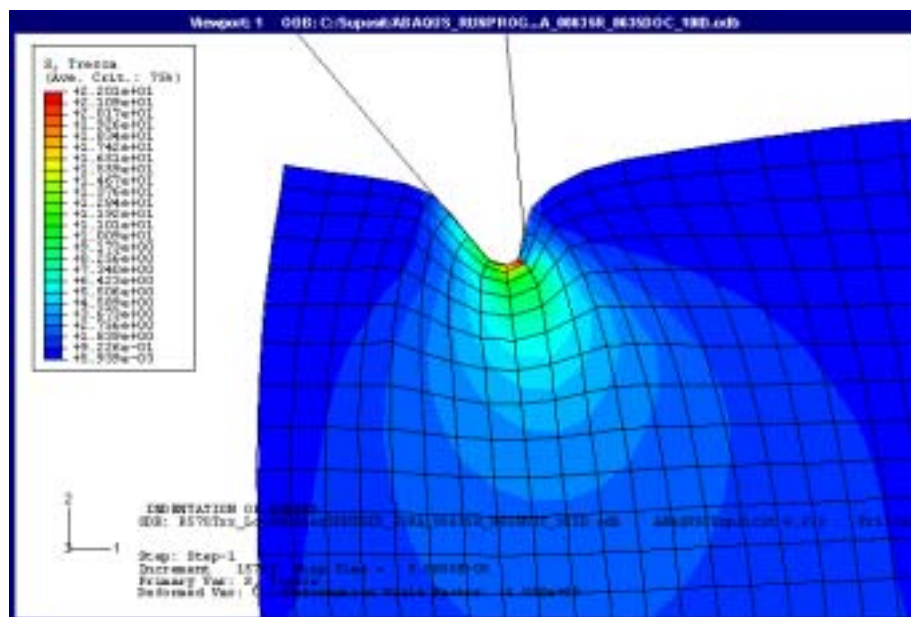


Figure 5.27 Tresca stress contours (MPa) for a half-wedge angle of 40 degrees, tip edge radius of 0.00635 mm, feed of 0.0635 mm, friction coefficient of 0.60, and indentation depth of 0.10 mm.

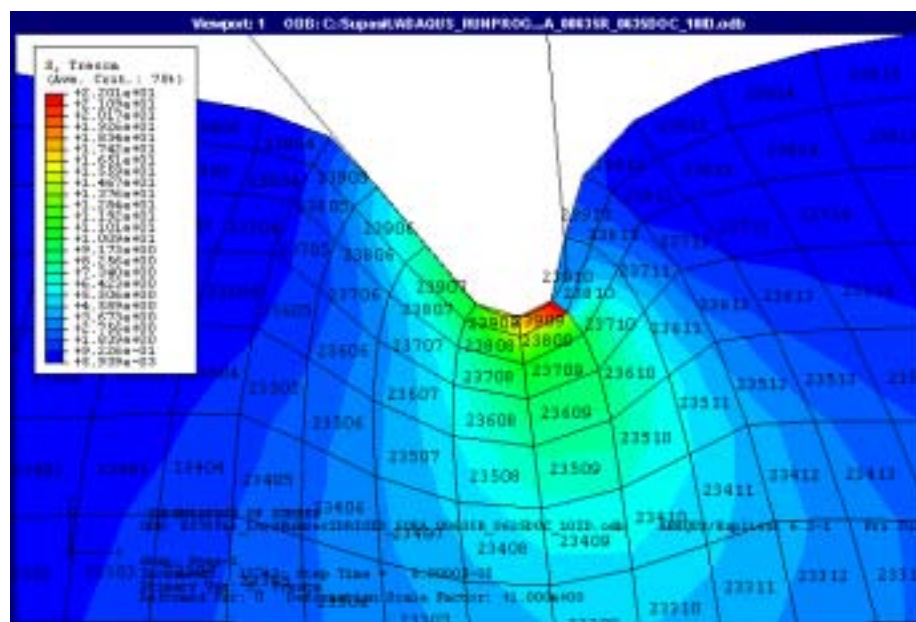


Figure 5.28 Detailed view of Tresca stress contours (MPa) for a half-wedge angle of 40 degrees, tip edge radius of 0.00635 mm, feed of 0.0635 mm, friction coefficient of 0.60, and indentation depth of 0.10 mm.

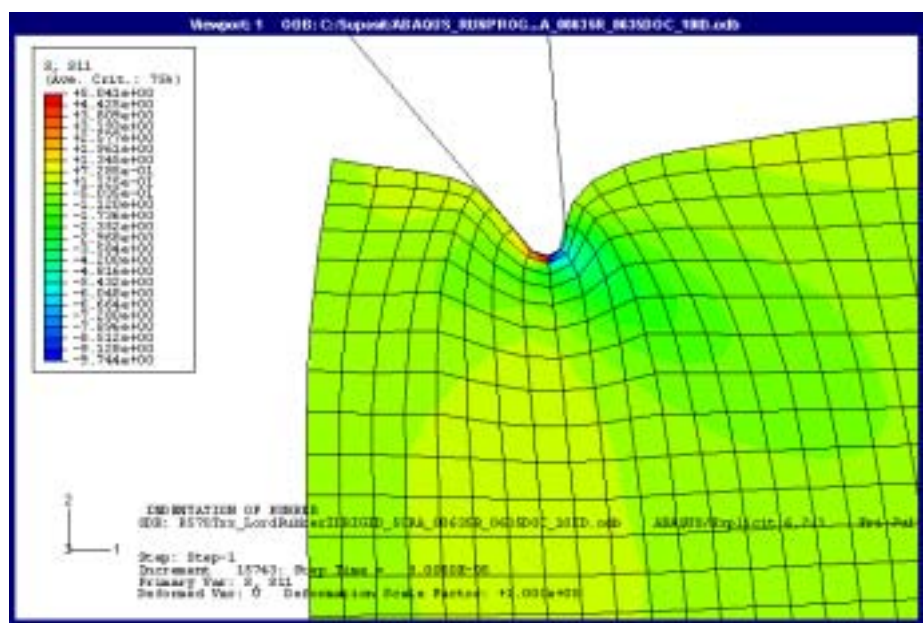


Figure 5.29 Normal stress contours (MPa) for a half-wedge angle of 40 degrees, tip edge radius of 0.00635 mm, feed of 0.0635 mm, friction coefficient of 0.60, and indentation depth of 0.10 mm.

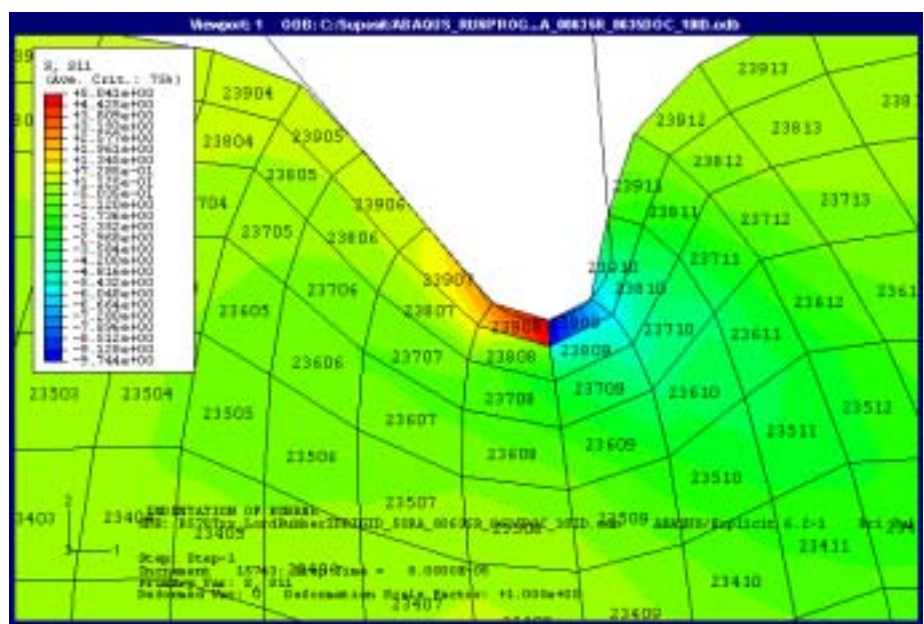


Figure 5.30 Detailed view of normal stress contours (MPa) for a half-wedge angle of 40 degrees, tip edge radius of 0.00635 mm, feed of 0.0635 mm, friction coefficient of 0.60, and indentation depth of 0.10 mm.

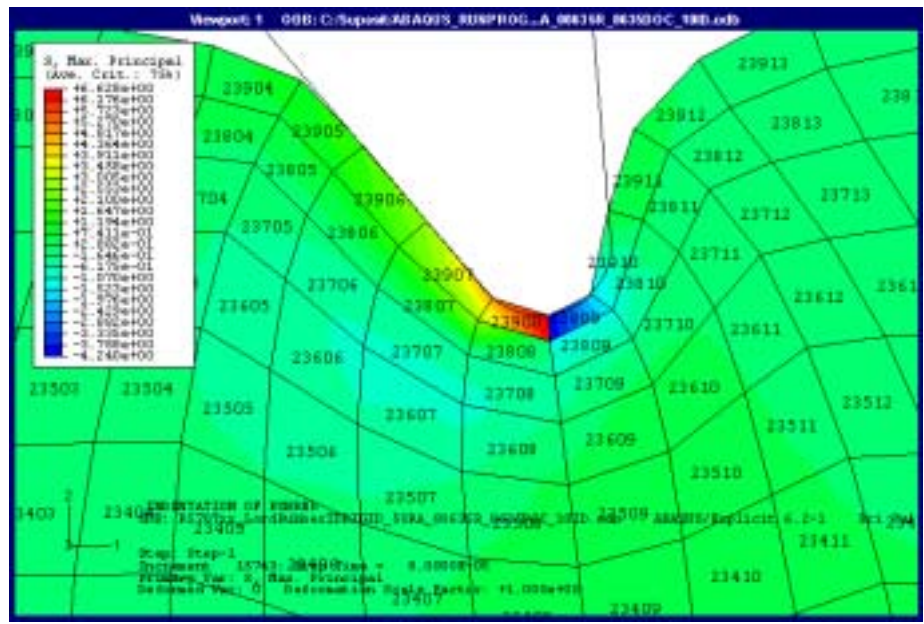


Figure 5.31 Detailed view of maximum principal stress contours (MPa) for a half-wedge angle of 40 degrees, tip edge radius of 0.00635 mm, feed of 0.0635 mm, friction coefficient of 0.60, and indentation depth of 0.10 mm.

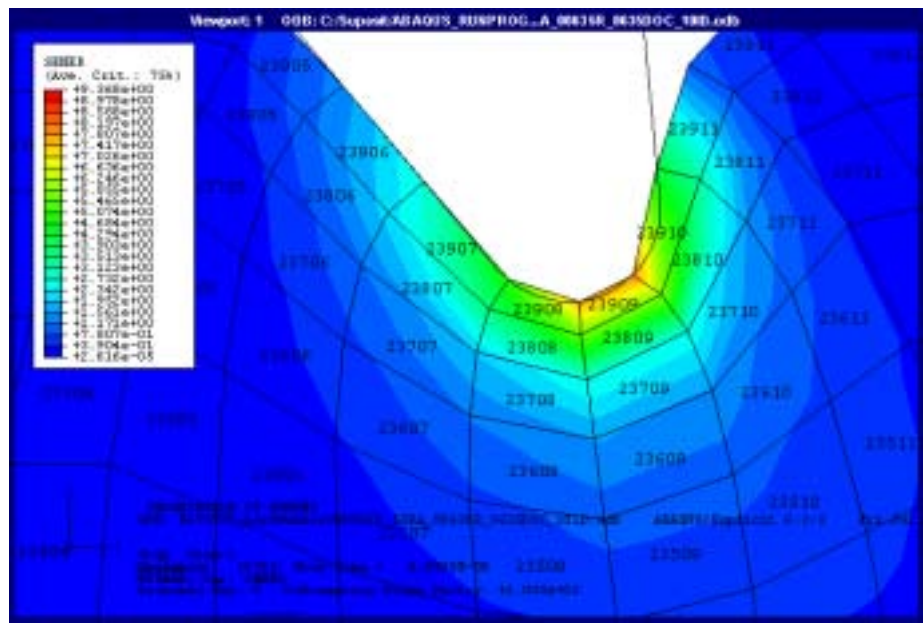


Figure 5.32 Detailed view of strain energy density contours (MPa) for a half-wedge angle of 40 degrees, tip edge radius of 0.00635 mm, feed of 0.0635 mm, friction coefficient of 0.60, and indentation depth of 0.10 mm.

As discussed in Chapter 3, it was observed from the orthogonal cutting tests of elastomers that the tool rake angle had a significant effect on the type of chip produced and the resulting machined surface finish. Figure 5.33 shows the relationship between the normal stress under the indenter tip and various half-wedge indenter angles. A similar trend for the maximum principal stress can also be seen in Figure 5.34. Both the normal stress and maximum principal stress become more tensile as the half-wedge angle is decreased. For instance, for a 10 mm indentation depth, a tensile stress occurs for half-wedge angles of 65 degrees or less. Therefore, a tensile stress occurs for a 40 degree indenter, while a 80 degree indenter produced a compressive stress. As discussed previously, a tensile normal stress is essential for incipient chip separation to occur. This result is consistent with the cutting tests that demonstrated that a good surface finish was produced for the 50 degree rake angle tool (40 degree indenter), while the 10 degree rake angle tool (80 degree indenter) produced a roughened surface.

Note that two indentation depths were employed in this study. The simulations indicated that as the indentation depth was increased, the normal stress became more compressive. Therefore, chip separation will more likely occur at the smaller indentation depth for which the normal stress is more highly tensile.

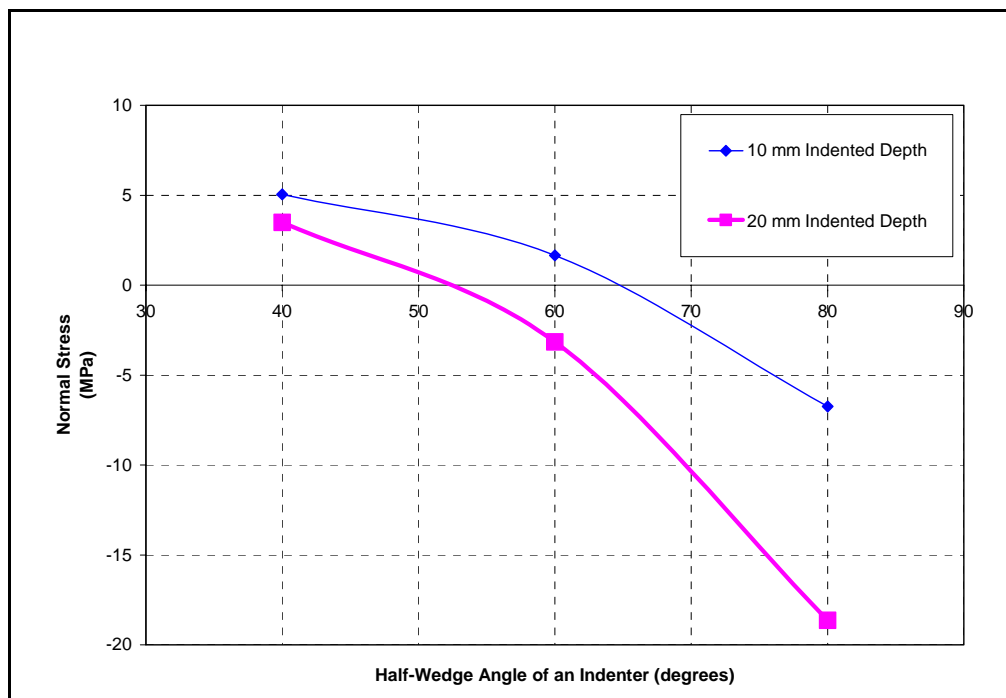


Figure 5.33 Normal stress of the elastomeric workpiece area under the indenter tip for a tip edge radius of 0.00635 mm, feed of 0.0635 mm, and friction coefficient of 0.60 with various half-wedge angles.

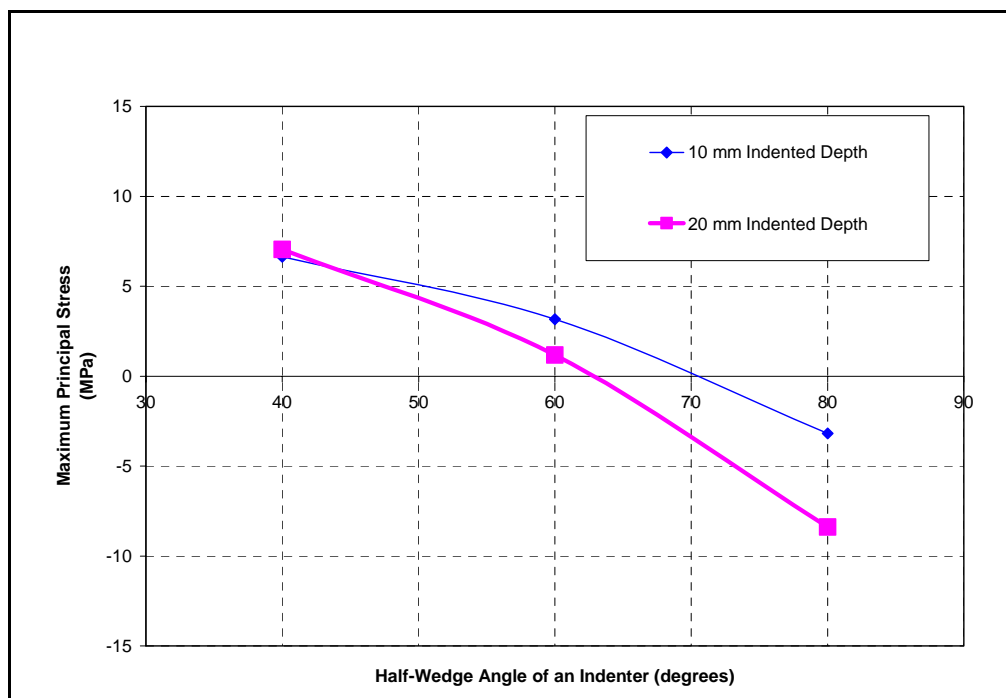


Figure 5.34 Maximum principal stress of the elastomeric workpiece area under the indenter tip for a tip edge radius of 0.00635 mm, feed of 0.0635 mm, and friction coefficient of 0.60 with various half-wedge angles.

Figure 5.35 shows the relationship between the strain energy density under the indenter tip and the indenter angle. It was found that a 40 degree half-wedge indenter produced higher strain energy density than a 80 degree half-wedge indenter angle. Higher strain energy density leads to higher tearing energy, as defined previously in equation (2.13). This would tend to cleanly separate the chip from the workpiece and produce a smooth machined surface finish.

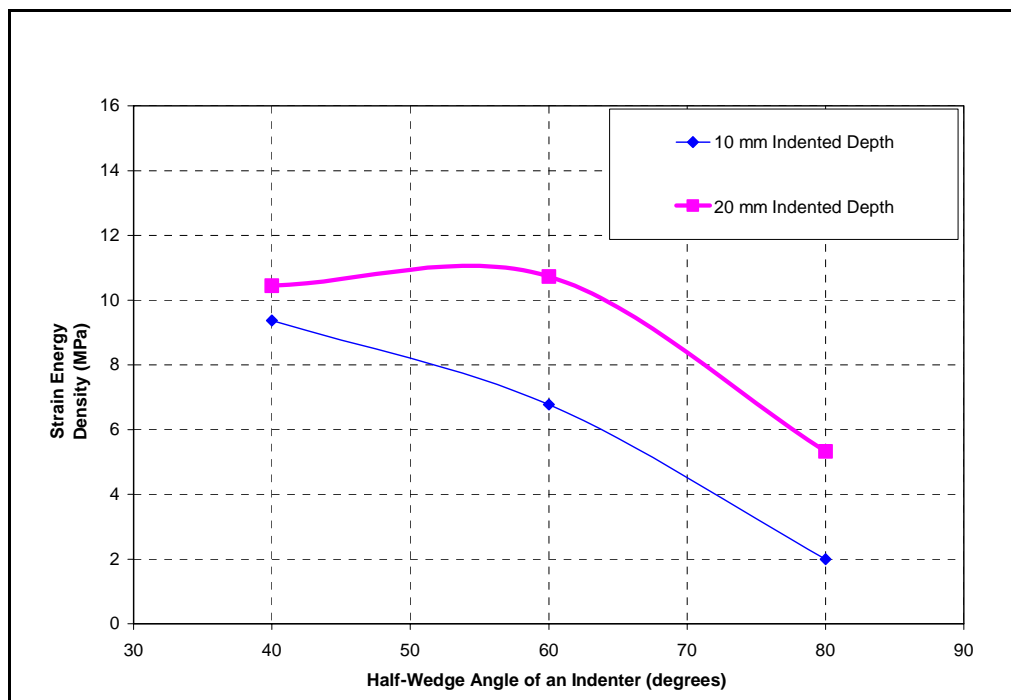


Figure 5.35 Strain energy density of the elastomeric workpiece area under the indenter tip for a tip edge radius of 0.00635 mm, feed of 0.0635 mm, and friction coefficient of 0.60 with various half-wedge angles.

5.2.3 Wedge Indentation for a 40 degree Half-Wedge Indenter and Tip Edge Radius of 0.01270 mm (Case 3)

The effect of the tip edge radius on the machinability of elastomers was investigated. Figure 5.36 shows the finite element mesh for both the undeformed and deformed configurations for an indenter with a half-wedge angle of 40 degrees and a large tip edge radius of 0.0127 mm. A feed of 0.0635 mm and a friction coefficient of 0.60 were applied for an indentation depth of 0.10 mm.

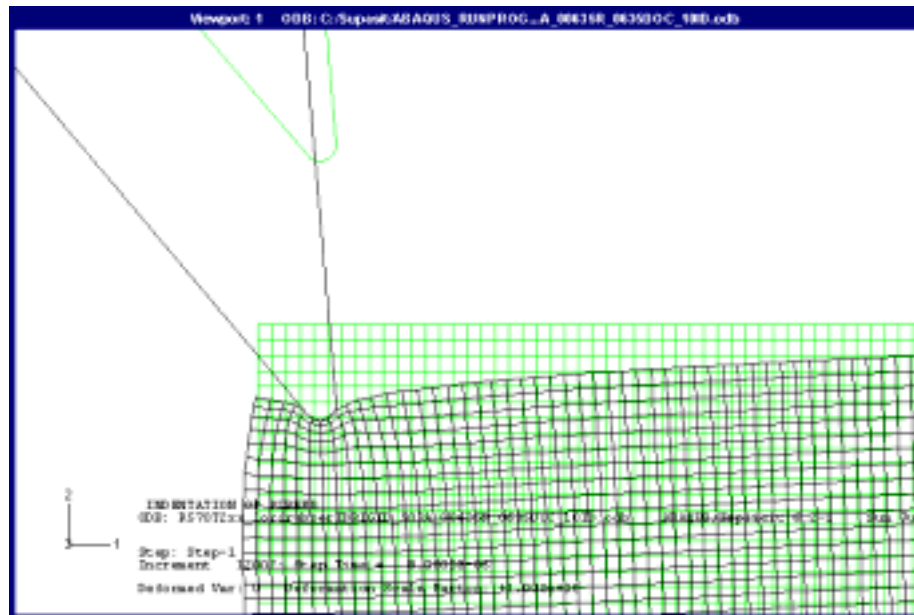


Figure 5.36 Deformed and undeformed configurations of the finite element mesh for a half-wedge angle of 40 degrees, tip edge radius of 0.01270 mm, feed of 0.0635 mm, friction coefficient of 0.60, and indentation depth of 0.10 mm.

Compared to an indenter with a smaller tip radius of 0.00635 mm, indentation with the larger tip radius results in a compressive normal stress and maximum principal stress in the vicinity of the separation point as shown in Figures 5.37–5.39. As pointed out previously, a compressive stress would not support clean separation of the chip from the workpiece surface. In addition, the maximum strain energy density is significantly reduced to approximately 1.5 MPa under the indenter tip as shown in Figure 5.40. Therefore, it is unlikely that a chip would be formed for this large radius indenter.

It should be noted that the maximum principal stress reaches a tensile value far from the tip as shown in Figure 5.39 (element numbers 23903, 23904, and 23905). This could cause rupture of the rubber in this area which is far from the indenter tip, leading to severe tearing of the material and a rough surface finish.

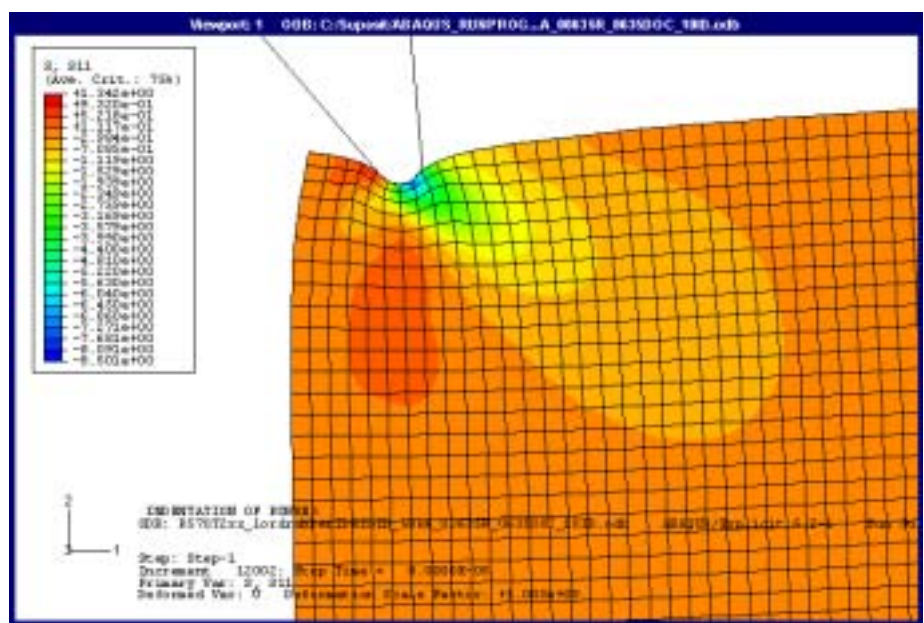


Figure 5.37 Normal stress contours (MPa) for a half-wedge angle of 40 degrees, tip edge radius of 0.01270 mm, feed of 0.0635 mm, friction coefficient of 0.60, and indentation depth of 0.10 mm.

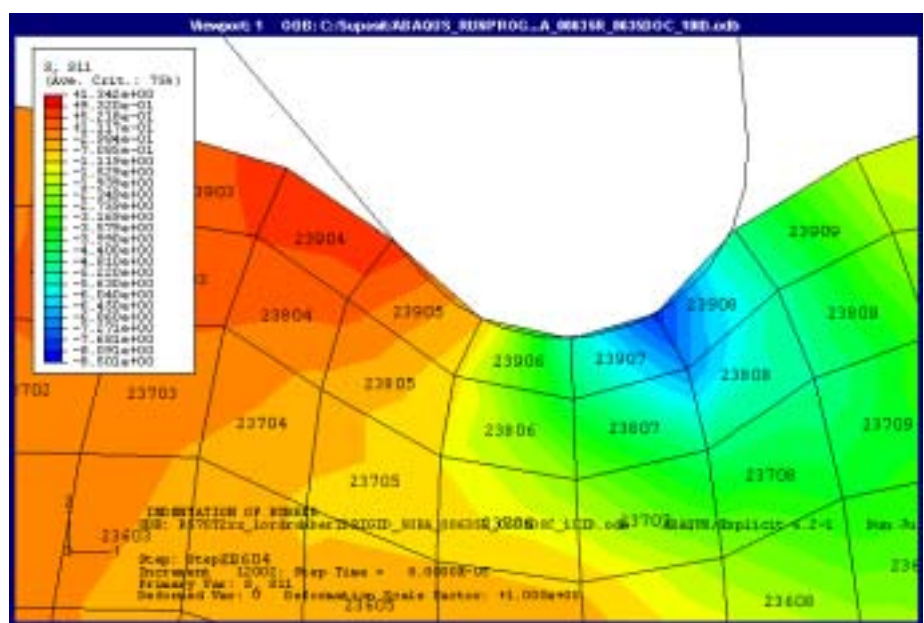


Figure 5.38 Detailed view of normal stress contours (MPa) for a half-wedge angle of 40 degrees, tip edge radius of 0.01270 mm, feed of 0.0635 mm, friction coefficient of 0.60, and indentation depth of 0.10 mm.

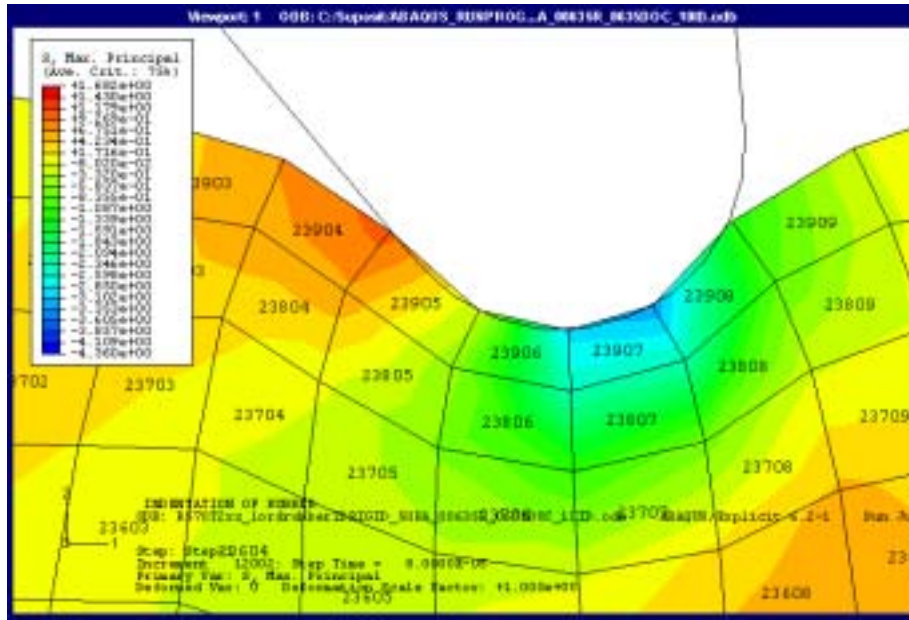


Figure 5.39 Detailed view of maximum principal stress contours (MPa) for a half-wedge angle of 40 degrees, tip edge radius of 0.01270 mm, feed of 0.0635 mm, friction coefficient of 0.60, and indentation depth of 0.10 mm.

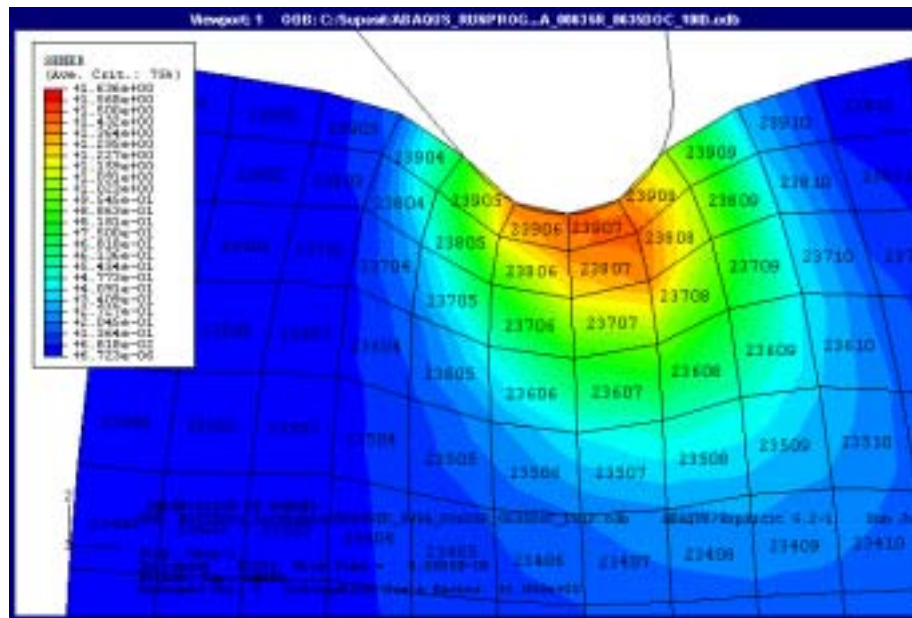


Figure 5.40 Detailed view of strain energy density contours (MPa) for a half-wedge angle of 40 degrees, tip edge radius of 0.01270 mm, feed of 0.0635 mm, friction coefficient of 0.60, and indentation depth of 0.10 mm.

It is useful to compare the normal stress and strain energy density near the indentation tip for the three half-wedge angle indenters. Figure 5.41 shows the normal stress in the workpiece under the indenter tip for various half-wedge indenter angles for a large tip edge radius. The stresses are compressive for all wedge angles, which indicates that an indenter with a large tip radius will not create a chip that separates cleanly from the workpiece. Note that a compressive normal stress occurred for both indentation depths. Furthermore, the strain energy density remains fairly constant for various indenter half-wedge angles as shown in Figure 5.42. This is due to the fact that the large indenter tip radius causes the strain energy density to be more uniformly distributed near the indentation point.

Figure 5.43 compares the strain energy density and maximum principal stress for two tip radii. The indenter tip edge radius has a more significant effect on the strain energy density and maximum principal stress as a half-wedge angle of an indenter is decreased.

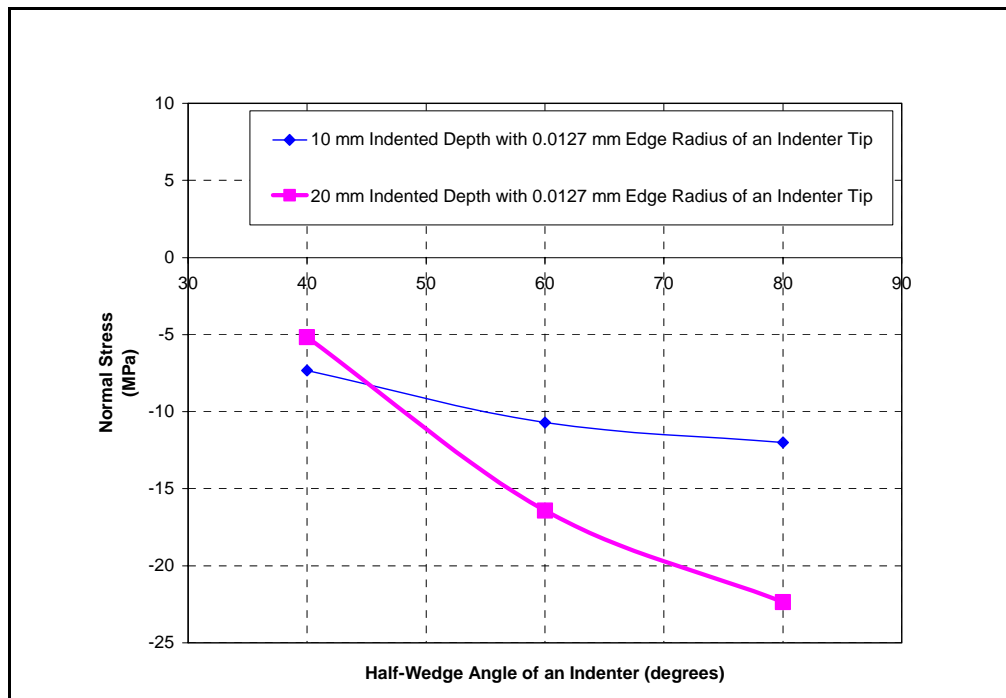


Figure 5.41 Normal stress of the elastomeric workpiece area under the indenter tip for a tip edge radius of 0.01270 mm, feed of 0.0635 mm, and friction coefficient of 0.60 with various half-wedge angles.

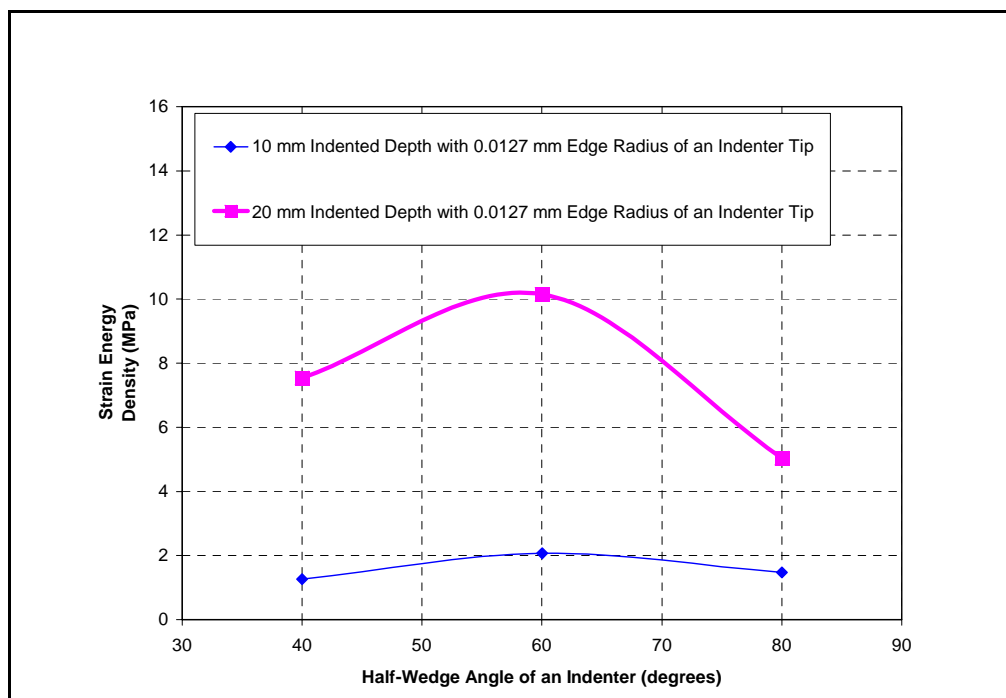


Figure 5.42 Strain energy density of the elastomeric workpiece area under the indenter tip for a tip edge radius of 0.01270 mm, feed of 0.0635 mm, and friction coefficient of 0.60 with various half-wedge angles.

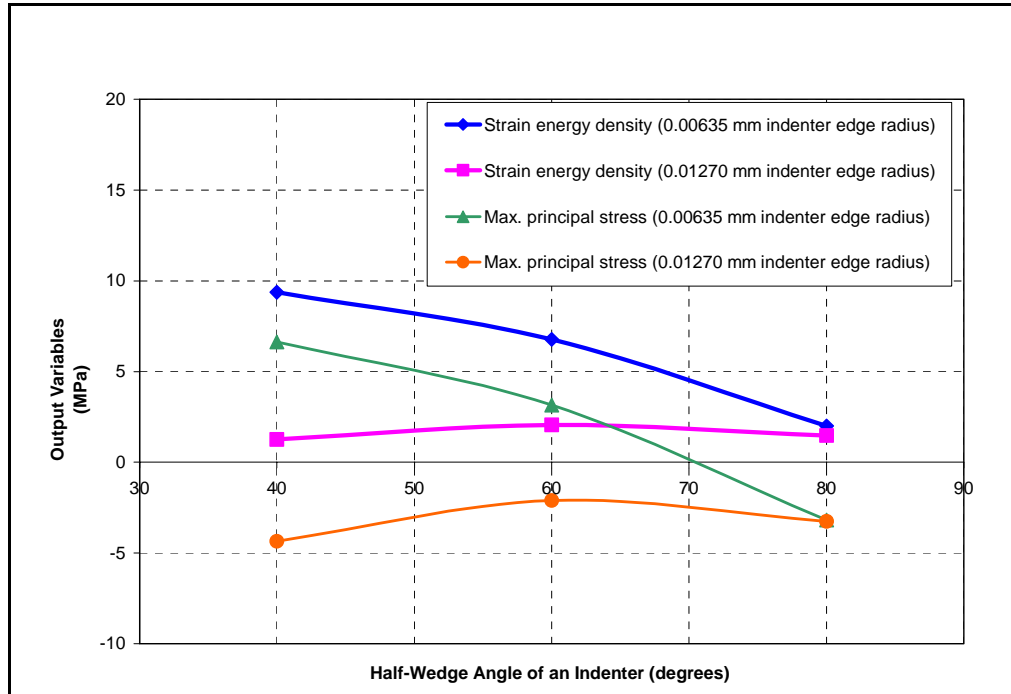


Figure 5.43 Effect of indenter tip edge radius on the strain energy density and maximum principal stress of the elastomeric workpiece area under feed of 0.0635 mm, and friction coefficient of 0.60 for various half-wedge angles at 10 mm indentation depth.

5.2.4 Wedge Indentation for a 40 degree Half-Wedge Indenter for Feed of 0.2540 mm (Case 4)

The effect of the distance to the free edge of the workpiece or feed on chip formation in wedge indentation is described in this section. Figure 5.44 shows the finite element mesh for both the undeformed and deformed configurations for an indenter with a half-wedge angle of 40 degrees and a tip edge radius of 0.00635 mm. A feed of 0.2540 mm with a friction coefficient along the indenter/workpiece interface of 0.60 for an indentation depth of 0.10 mm was used.

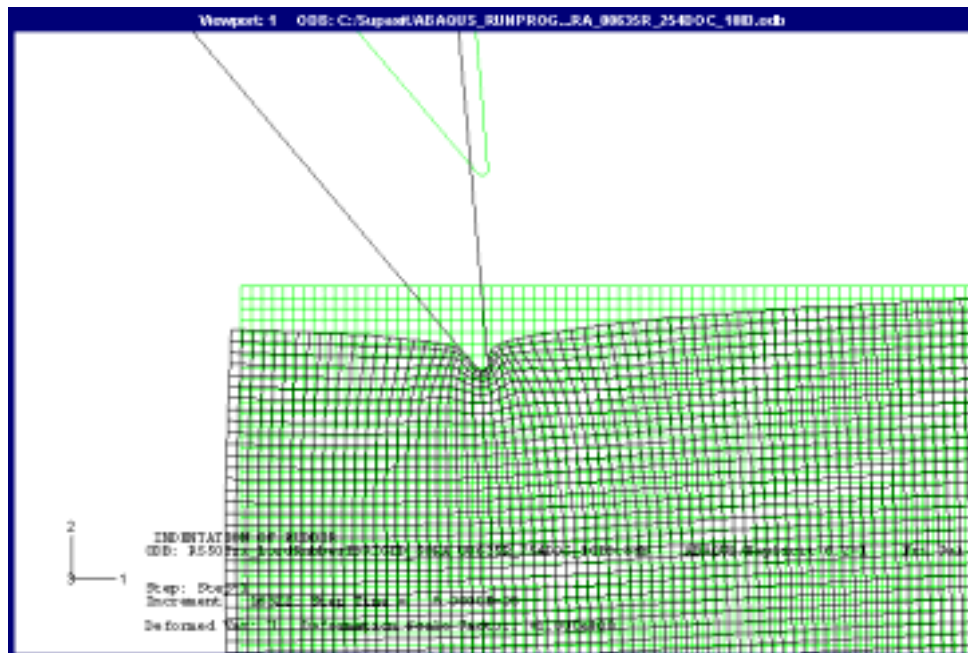


Figure 5.44 Deformed and undeformed configurations of the finite element mesh for a half-wedge angle of 40 degrees, tip edge radius of 0.00635 mm, feed of 0.2540 mm, friction coefficient of 0.60, and indentation depth of 0.10 mm.

Figure 5.44 shows that a 40 degree half-wedge indenter angle with a feed of 0.2540 mm produced less lateral expansion as compared with the feed of 0.0635 mm. Figures 5.45 and 5.46, show that a compressive normal occurs in the workpiece (element number 23927) near the vicinity of chip separation at approximately half the tip edge radius from the indenter clearance face. Figure 5.47 shows that both negative and positive maximum principal stresses occur under the indenter tip. Note that a large maximum strain energy density exceeding 9 MPa occurs under the indenter tip as shown in Figure 5.48. Therefore, high strain energy density at the tip indicates that incipient chip formation is likely to occur even though a compressive stress exists in the vicinity of the tip. Based on equation (2.13), tearing of elastomers occurs more readily when the strain energy density is large.

These conclusions are consistent with the orthogonal cutting tests performed in Chapter 3 in which a smooth surface finish and corresponding continuous chips were obtained for a tool with a rake angle of 50 degrees and a feed of 0.2540 mm. For reference, the chips are shown in Figure 3.4 and the corresponding surface finish is shown in Figure 3.5.

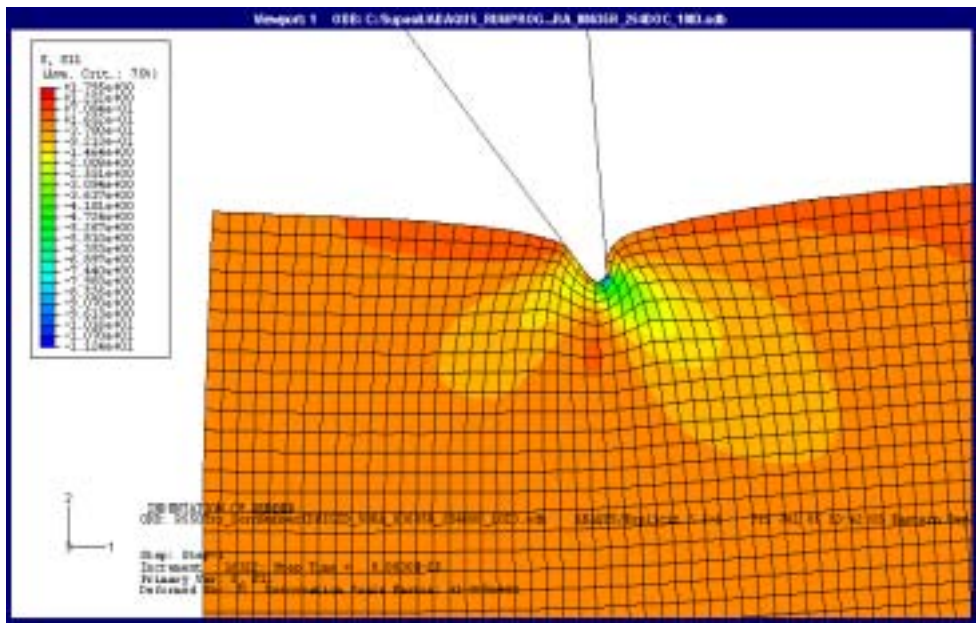


Figure 5.45 Normal stress contours (MPa) for a half-wedge angle of 40 degrees, tip edge radius of 0.00635 mm, feed of 0.2540 mm, friction coefficient of 0.60, and indentation depth of 0.10 mm.

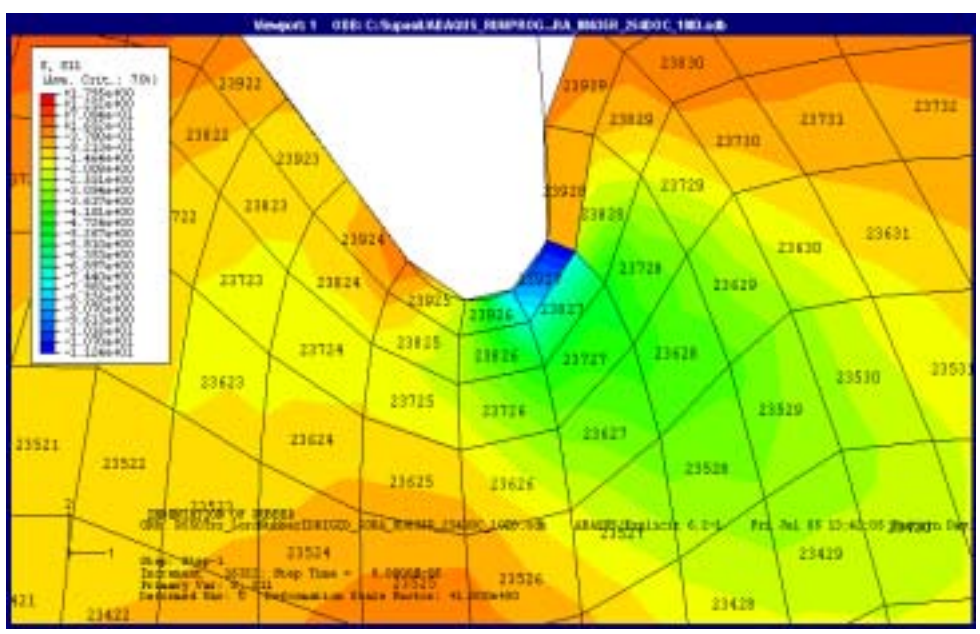


Figure 5.46 Detailed view of normal stress contours (MPa) for a half-wedge angle of 40 degrees, tip edge radius of 0.00635 mm, feed of 0.2540 mm, friction coefficient of 0.60, and indentation depth of 0.10 mm.

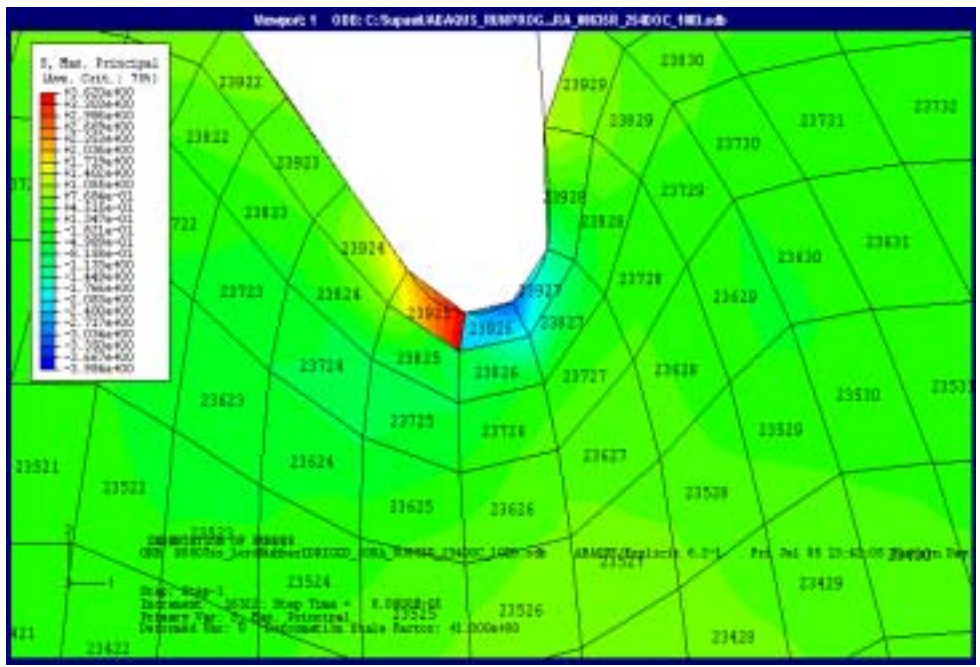


Figure 5.47 Detailed view of maximum principal stress contours (MPa) for a half-wedge angle of 40 degrees, tip edge radius of 0.00635 mm, feed of 0.2540 mm, friction coefficient of 0.60, and indentation depth of 0.10 mm.

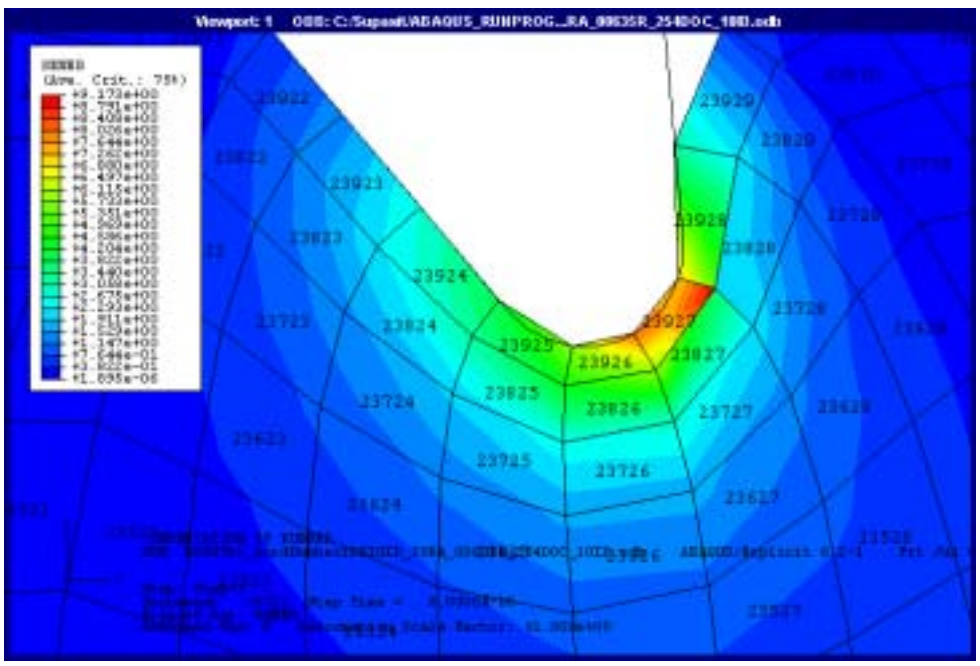


Figure 5.48 Detailed view of strain energy density contours (MPa) for a half-wedge angle of 40 degrees, tip edge radius of 0.00635 mm, feed of 0.2540 mm, friction coefficient of 0.60, and indentation depth of 0.10 mm.

The strain energy density and the maximum principal stresses are plotted in Figure 5.49 for a range of half-wedge indenter angles. The strain energy density remains unchanged for both feeds over the range of half-wedge indenter angles used in this research. Only a small difference occurred in the strain energy density for the large feed of 0.2540 mm. This figure also shows that as the feed increases, a relatively lower maximum principal stress occurs.

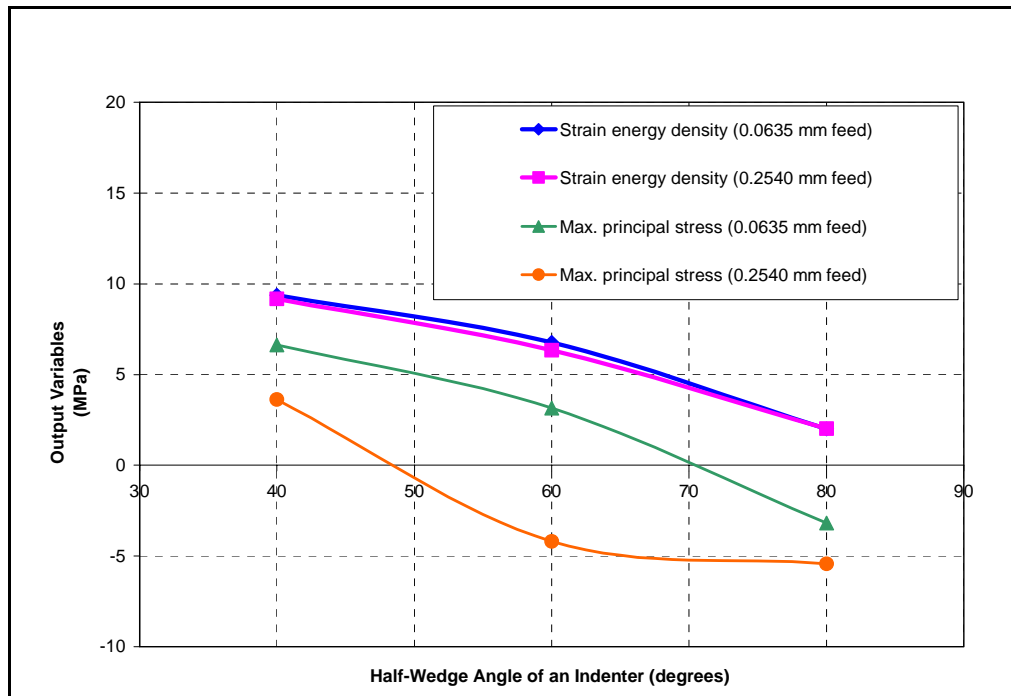


Figure 5.49 Effect of indentation feed on the strain energy density and maximum principal stress of the elastomer workpiece area under an indenter tip for a tip edge radius of 0.00635 mm, and friction coefficient of 0.60 for various half-wedge angles at 10 mm indentation depth.

5.2.5 Wedge Indentation for a 40 degree Half-Wedge Indenter and a Friction Coefficient of 1.20 (Case 5)

The effect of friction along the indenter/workpiece interface is discussed in this section. Figure 5.50 shows the finite element mesh for both the undeformed and deformed configurations using an indenter with a half-wedge angle of 40 degrees, and a tip edge radius of 0.00635 mm. A feed of 0.0635 mm, a friction coefficient along the indenter/workpiece interface of 1.20, and an indentation depth of 0.10 mm were used.

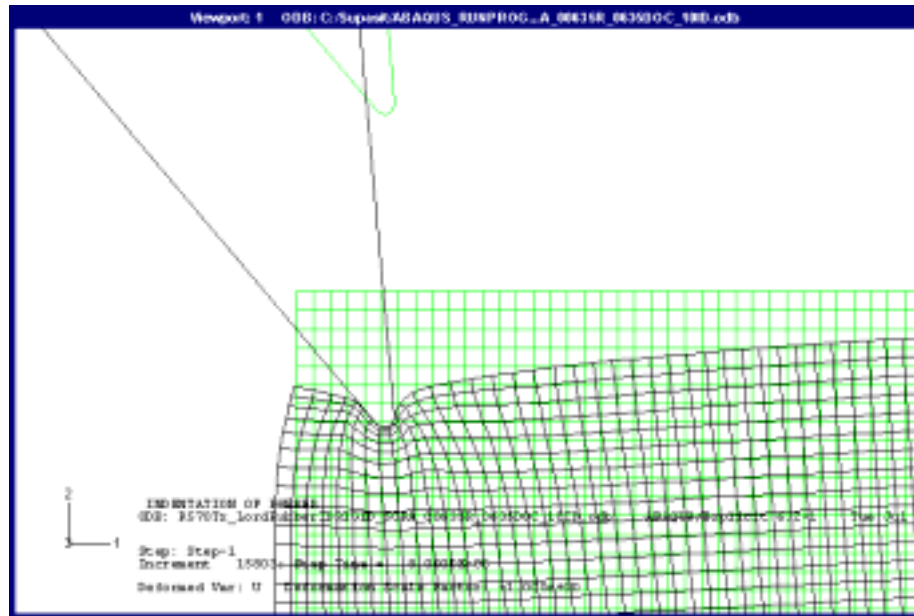


Figure 5.50 Deformed and undeformed configurations of the finite element mesh for a half-wedge angle of 40 degrees, tip edge radius of 0.00635 mm, feed of 0.0635 mm, friction coefficient of 1.20, and indentation depth of 0.10 mm.

Figures 5.51 and 5.52 show that the normal stress is largely compressive near the indenter tip. A tensile stress occurs in the workpiece (element number 23905 and 23906) at a distance far from the indenter tip. Figure 5.53 shows similar trends for the maximum principal stress. A small maximum strain energy density of 4 MPa occurs in the vicinity of the tip (element 23909) as shown in Figure 5.54. Based on the conditions for chip formation, it is unlikely that a chip will form because the tensile normal stress occurs far from the chip separation point and the strain energy density is very low. Therefore, a rough surface finish would be expected. This implies that the use of a lubricant to reduce the friction along the interface could improve chip formation in the machining of elastomers.

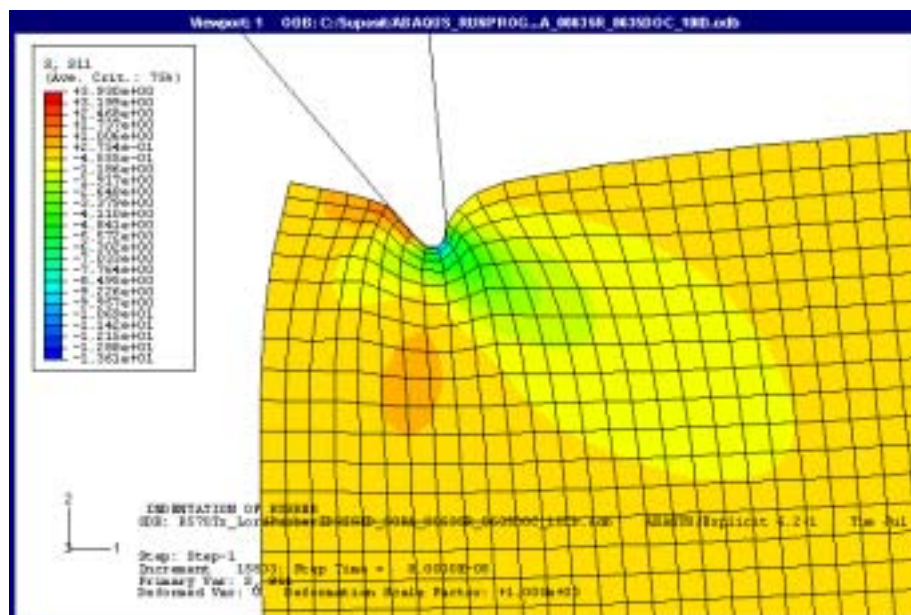


Figure 5.51 Normal stress contours (MPa) for a half-wedge angle of 40 degrees, tip edge radius of 0.00635 mm, feed of 0.0635 mm, friction coefficient of 1.20, and indentation depth of 0.10 mm.

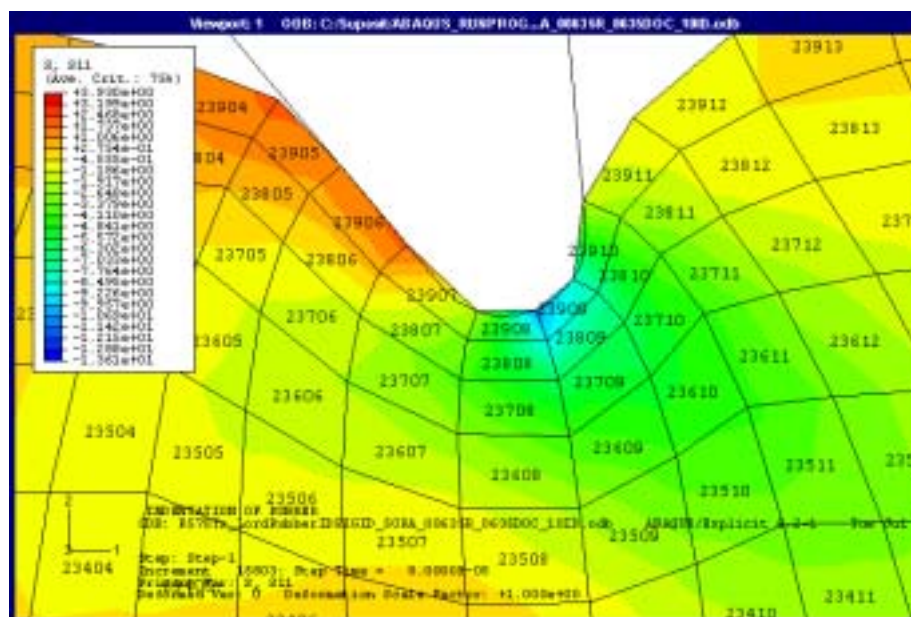


Figure 5.52 Detailed view of normal stress contours (MPa) for a half-wedge angle of 40 degrees, tip edge radius of 0.00635 mm, feed of 0.0635 mm, friction coefficient of 1.20, and indentation depth of 0.10 mm.

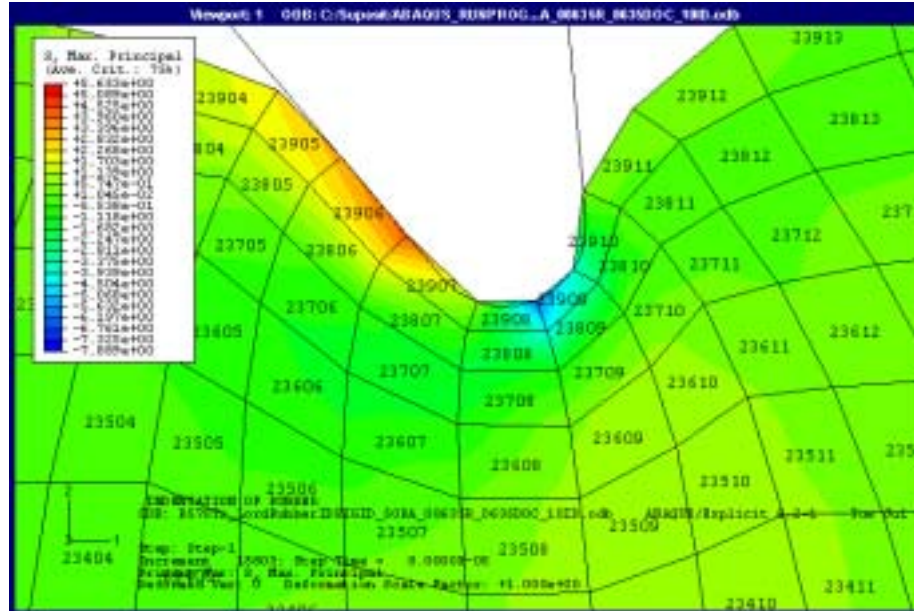


Figure 5.53 Detailed view of maximum principal stress contours (MPa) for a half-wedge angle of 40 degrees, tip edge radius of 0.00635 mm, feed of 0.0635 mm, friction coefficient of 1.20, and indentation depth of 0.10 mm.

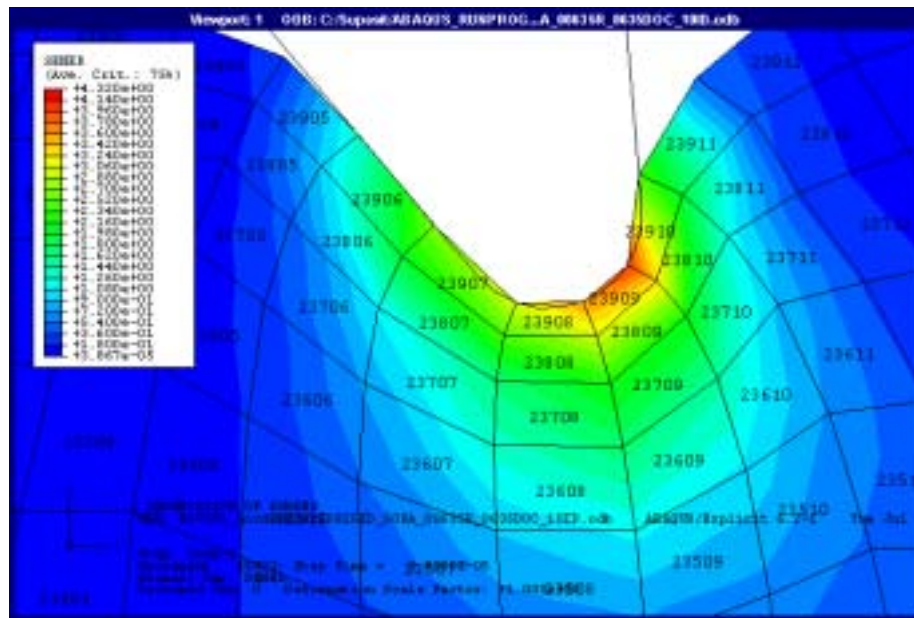


Figure 5.54 Detailed view of strain energy density contours (MPa) for a half-wedge angle of 40 degrees, tip edge radius of 0.00635 mm, feed of 0.0635 mm, friction coefficient of 1.20, and indentation depth of 0.10 mm.

Figure 5.55 shows the effect of friction on the strain energy density and maximum principal stress. It can be seen that as the friction increases, the strain energy density decreases significantly for small half-wedge indenter angles.

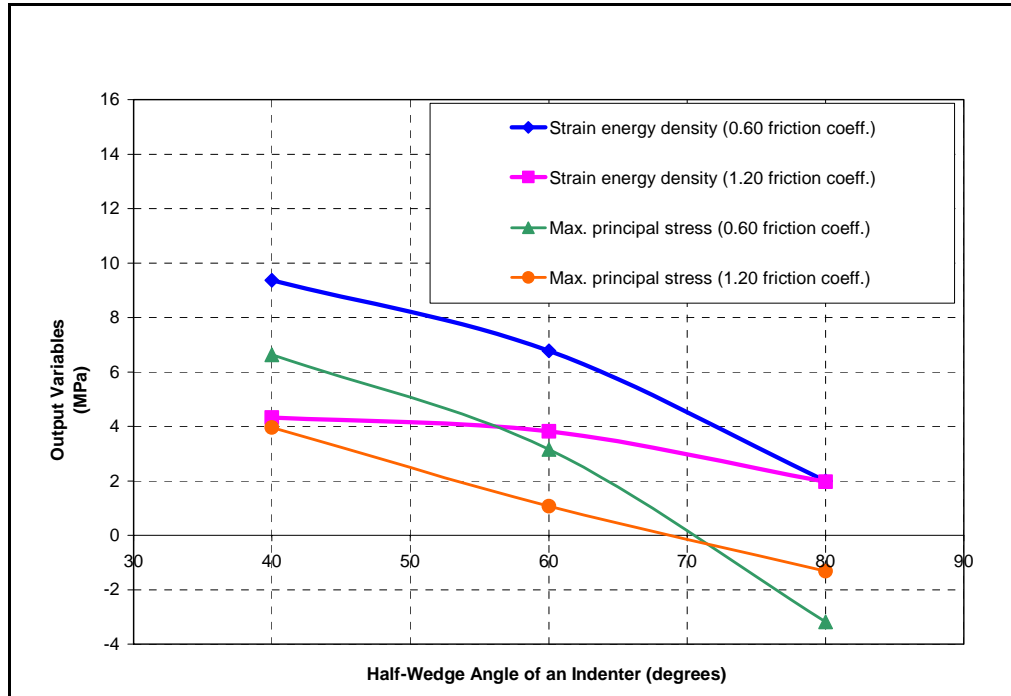


Figure 5.55 Effect of friction on workpiece/indenter interface on the strain energy density and maximum principal stress of the elastomeric workpiece area under the indenter tip for a tip edge radius of 0.00635 mm, and feed of 0.0635 mm for various half-wedge angles at 10 mm indentation depth.

5.2.6 Wedge Indentation for a 40 degree Half-Wedge Indenter and Boundary Condition Type 2 (Case 6)

The effect of fixture design of the workpiece on wedge indentation is described in this section. Figure 5.56 shows both the undeformed and deformed configurations for an indenter with a half-wedge angle of 40 degrees, and tip edge radius of 0.00635 mm. A feed of 0.0635 mm, friction coefficient along the indenter/workpiece interface of 0.60, indentation depth of 0.10 mm, and a boundary condition Type 2 were used.

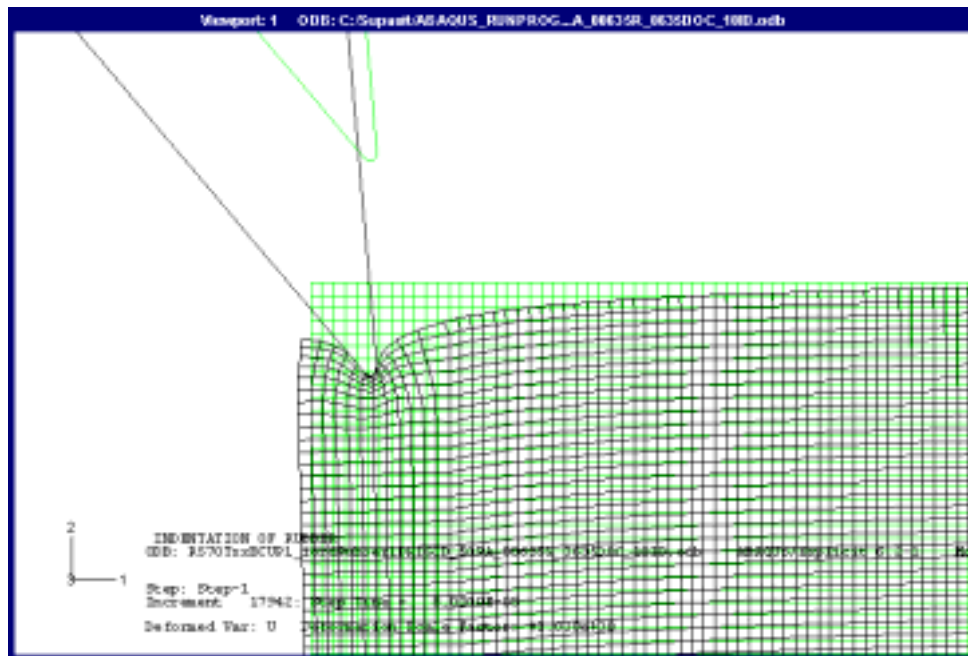


Figure 5.56 Deformed and undeformed configurations of the finite element mesh for a half-wedge angle of 40 degrees, tip edge radius of 0.00635 mm, feed of 0.0635 mm, friction coefficient of 0.60, indentation depth of 0.10 mm and a boundary condition Type 2.

Figures 5.57 and 5.58 show that a concentrated tensile normal stress occurs in the workpiece (element number 23906) in the vicinity of the chip separation point. Figure 5.59 shows a similar result for the maximum principal stress. A large maximum strain energy density exceeding 14 MPa occurs close to the chip separation point, as shown in Figure 5.60. Because the tensile normal stress and strain energy density are large near the chip separation point, a chip is likely to cleanly separate from the workpiece and produce a smooth surface finish.

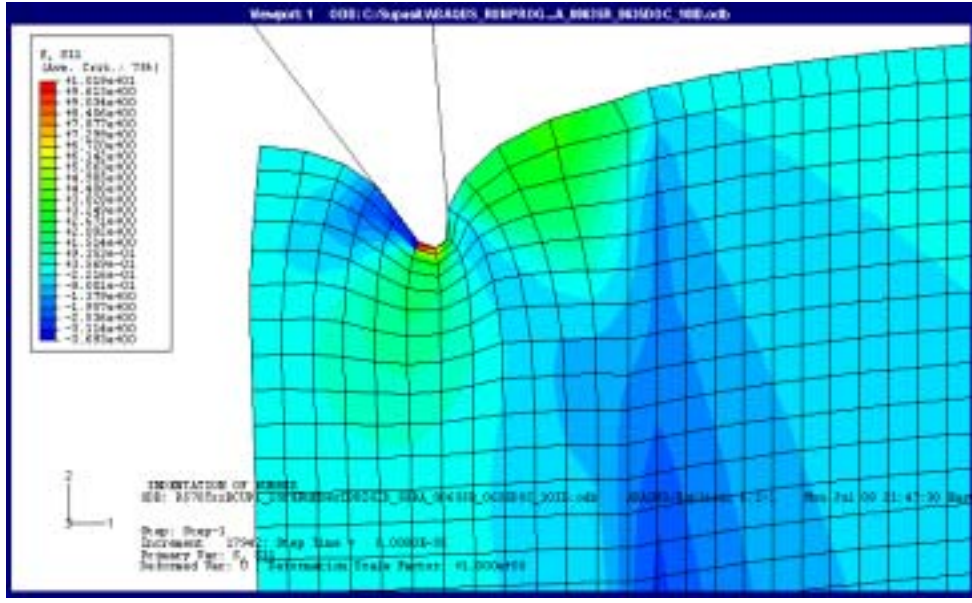


Figure 5.57 Normal stress contours (MPa) for a half-wedge angle of 40 degrees, tip edge radius of 0.00635 mm, feed of 0.0635 mm, friction coefficient of 0.60, indentation depth of 0.10 mm and a boundary condition Type 2.

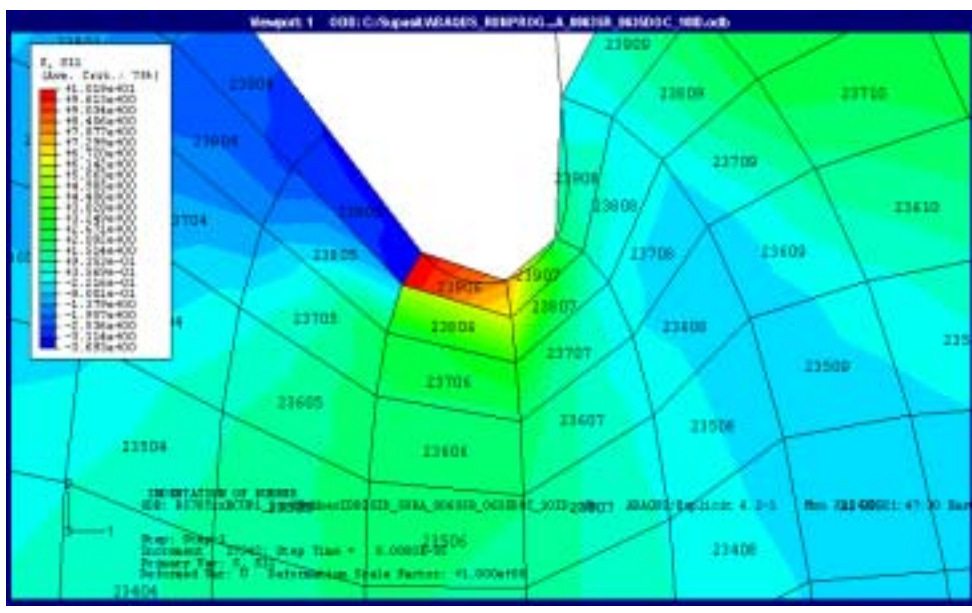


Figure 5.58 Detailed view of normal stress contours (MPa) for a half-wedge angle of 40 degrees, tip edge radius of 0.00635 mm, feed of 0.0635 mm, friction coefficient of 0.60, indentation depth of 0.10 mm and a boundary condition Type 2.

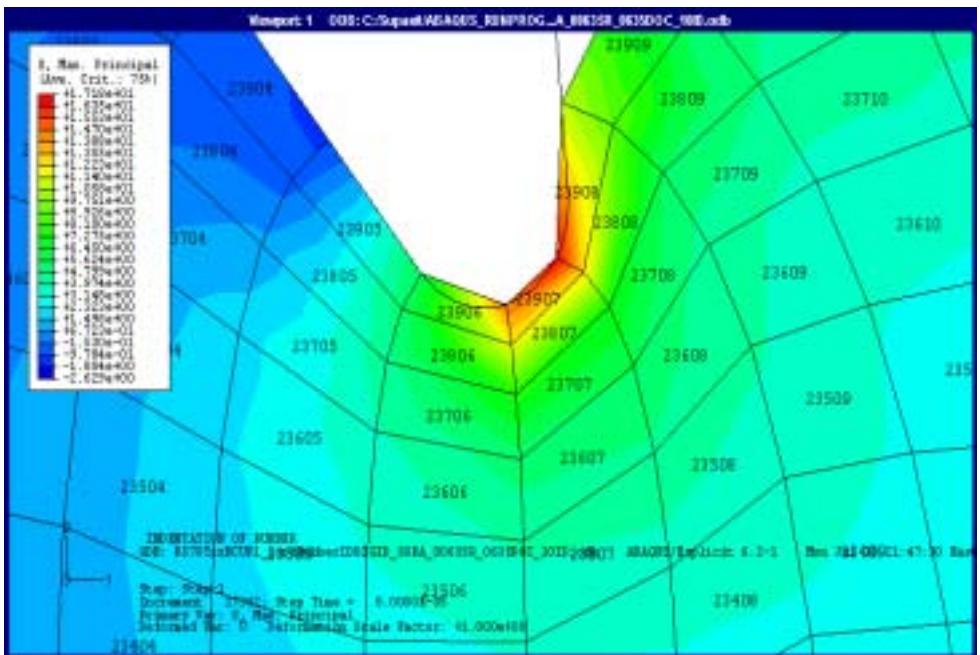


Figure 5.59 Detailed view of maximum principal stress contours (MPa) for a half-wedge angle of 40 degrees, tip edge radius of 0.00635 mm, feed of 0.0635 mm, friction coefficient of 0.60, indentation depth of 0.10 mm and a boundary condition Type 2.

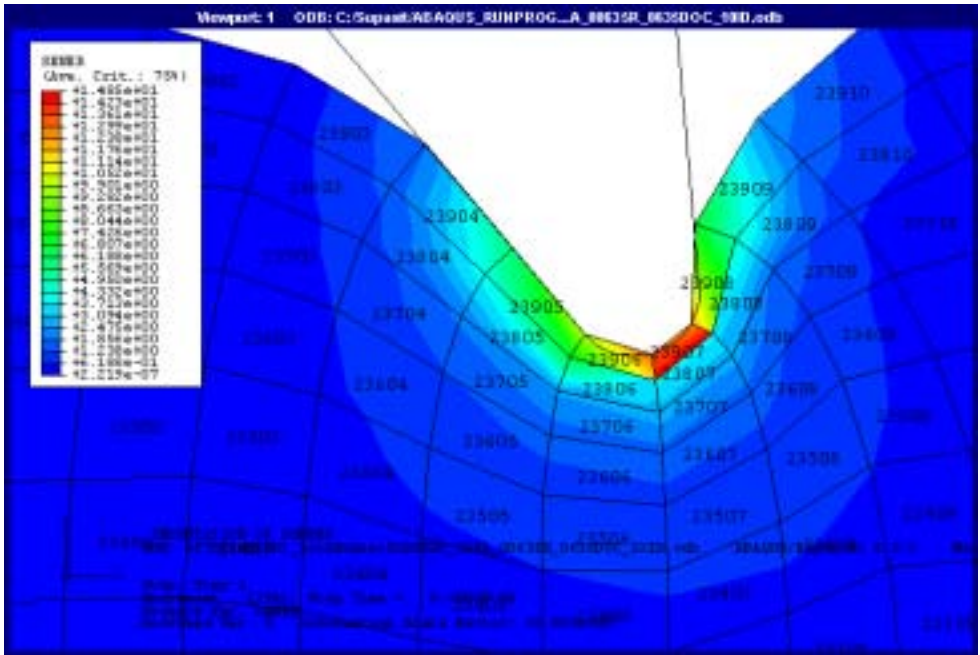


Figure 5.60 Detailed view of strain energy density contours (MPa) for a half-wedge angle of 40 degrees, tip edge radius of 0.00635 mm, feed of 0.0635 mm, friction coefficient of 0.60, indentation depth of 0.10 mm and a boundary condition Type 2.

Figure 5.61 shows that the strain energy density and maximum principal stress increases significantly when the boundary condition Type 2 is used. Therefore, a rigid fixture will improve the stiffness of the workpiece and leads to incipient chip separation and a smooth surface finish.

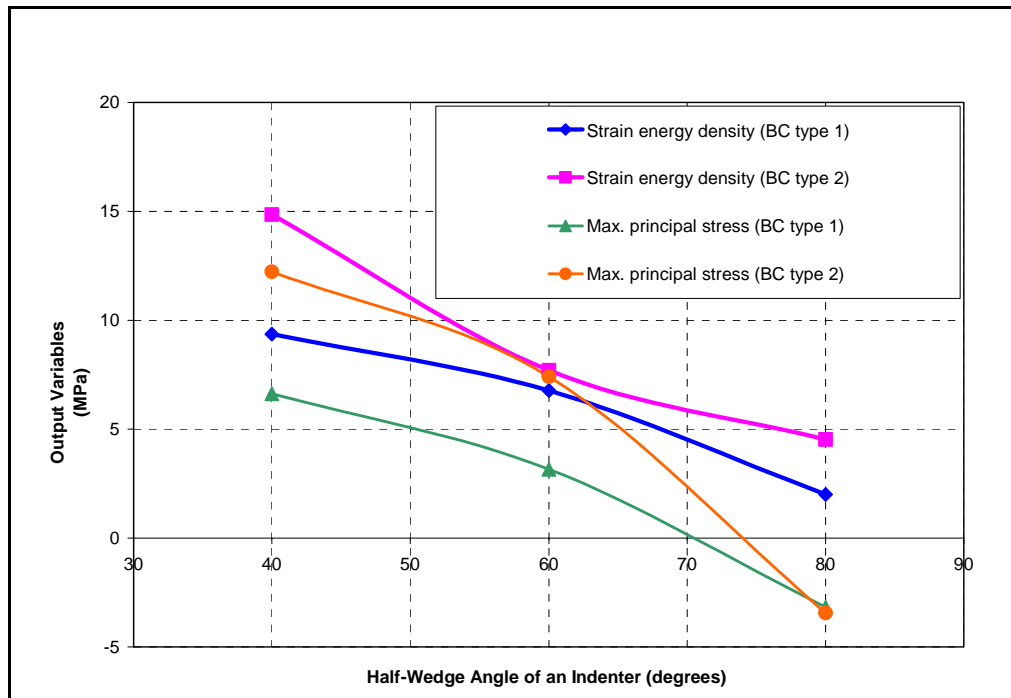


Figure 5.61 Effect of fixture design of the workpiece on the strain energy density and maximum principal stress of the elastomeric workpiece area under the indenter tip for a half-wedge angle of 40 degrees, tip edge radius of 0.00635 mm, feed of 0.0635 mm, friction coefficient of 0.60, and indentation depth of 0.10 mm for various half-wedge angles at 10 mm indentation depth.

5.3 Simulations of Orthogonal Cutting of Elastomers

An orthogonal cutting simulation of elastomers with a sharp cutting tool with a 30 degree rake angle and 5 degree clearance angle was conducted. Simulations were performed for a 0.1270 mm depth of cut and a cutting speed of 2.50 m/s. Similar to that used for metal cutting, a node separation algorithm based on a failure stress criteria was adopted for the elastomer cutting model. Note that the stress criterion for separation must be carefully selected because there is no obvious yield point in the stress-strain relationship. For these simulations, a critical normal tensile stress of 1 MPa was used.

Figure 5.62 shows the finite element mesh of the initial and final configurations of the cutting tool. The workpiece contained a total of 1659 nodes and 1512 elements which were two-dimensional, four-node bilinear plane strain elements. As compared with the metal cutting simulation shown in Figure 5.1, the elastomer workpiece exhibits significantly more deformation under the tool clearance face. The elastomer contacts the tool clearance face, which will lead to roughening of the machined surface. In addition, more contact would be expected for a worn tool with a large cutting edge radius. This simulation demonstrates the importance of using sharp tools with large clearance angles to obtain smooth machined elastomer surfaces.

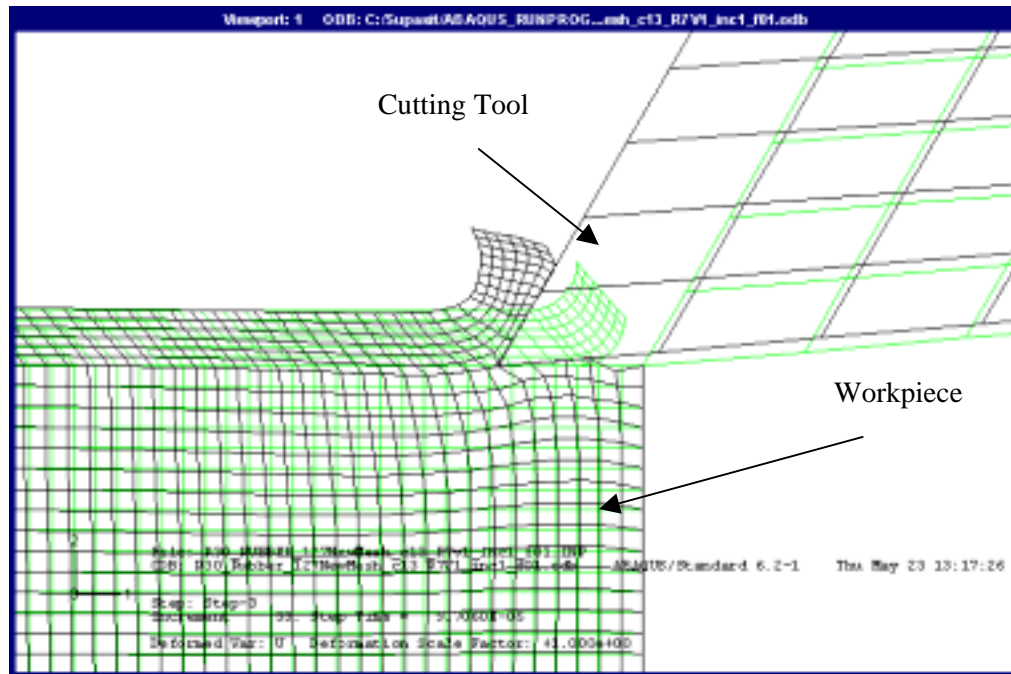


Figure 5.62 Undeformed and deformed configurations of the finite element mesh.

Von Mises stress contours are shown in Figures 5.63 and 5.64. As the cutting tool moves into the workpiece, the von Mises stress extends continuously from the point of initial chip separation to the free surface of the chip. However, no distinct area was found to occur in the primary shear zone as in metal cutting shown previously in Figures 5.2 and 5.3. Figures 5.65 and 5.66 show the Tresca stress contours. There is a significant difference in these contours as compared to the Tresca stress contours for metal cutting shown in Figures 5.4 and 5.5. There is a distinct shear zone that occurs for metal cutting while no such zone occurs for elastomers. Unlike metals, the mechanism for elastomer chip formation is not due to shear deformation in the primary shear zone.

Figures 5.67 and 5.68 show the normal stress contours in the vicinity of a tool tip. Figures 5.69 and 5.70 show similar trends for the positive maximum principal stress in the vicinity of

the tool tip near the separation point. These results agree with indentation simulations of elastomers in the previous section in which both a tensile normal stress and a positive maximum principal stress are needed to produce a continuous chip and a smooth surface finish.

Figures 5.71 and 5.72 show strain energy density contours which are calculated at the element integration point with respect to the element volume. Although, the strain energy density is higher in the vicinity of the tool tip, there is no distinct area in the primary shear zone as in metal cutting as shown in Figures 5.8 and 5.9. This supports the conclusion that the mechanism of chip formation for elastomers is significantly different than that for metals.

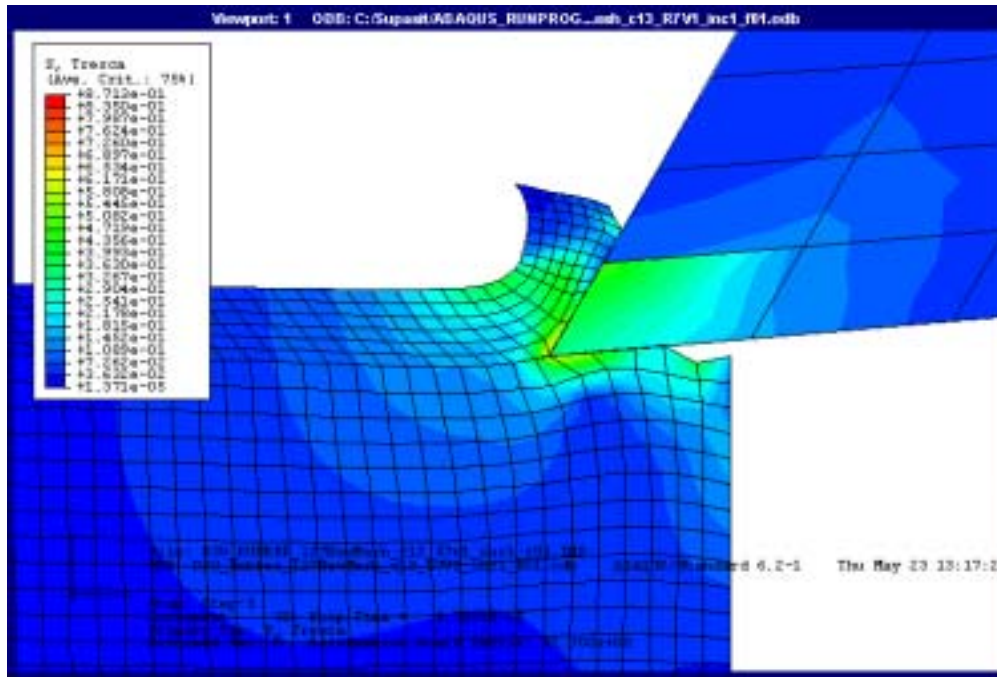


Figure 5.65 Tresca stress contours (MPa) at the analysis step 3, increment 33.

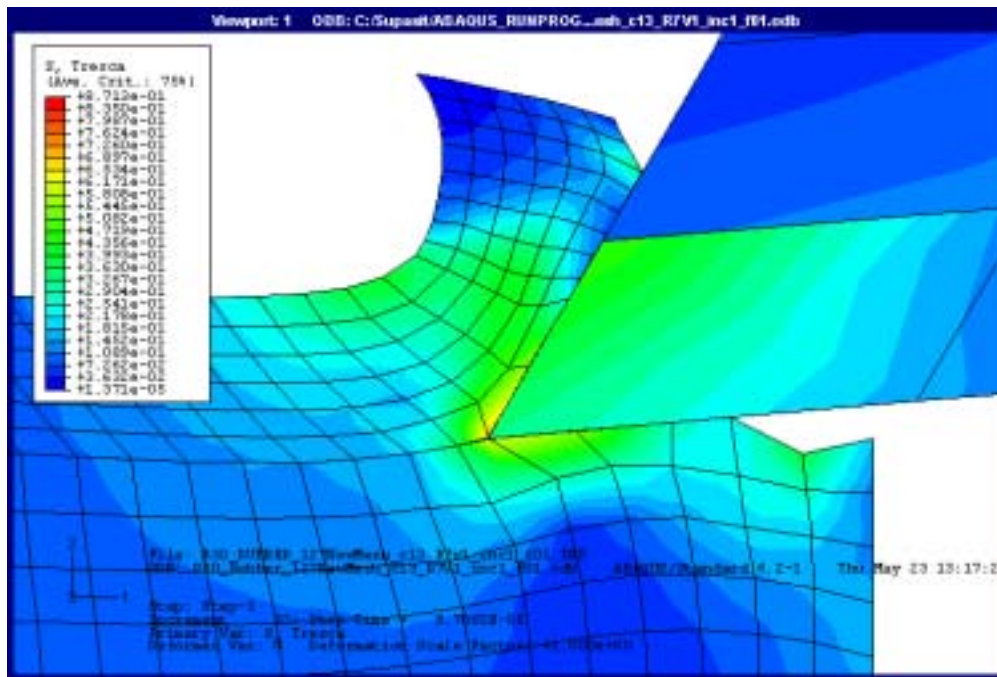


Figure 5.66 Tresca stress contours (MPa) at the analysis step 3, increment 33 (detailed view).

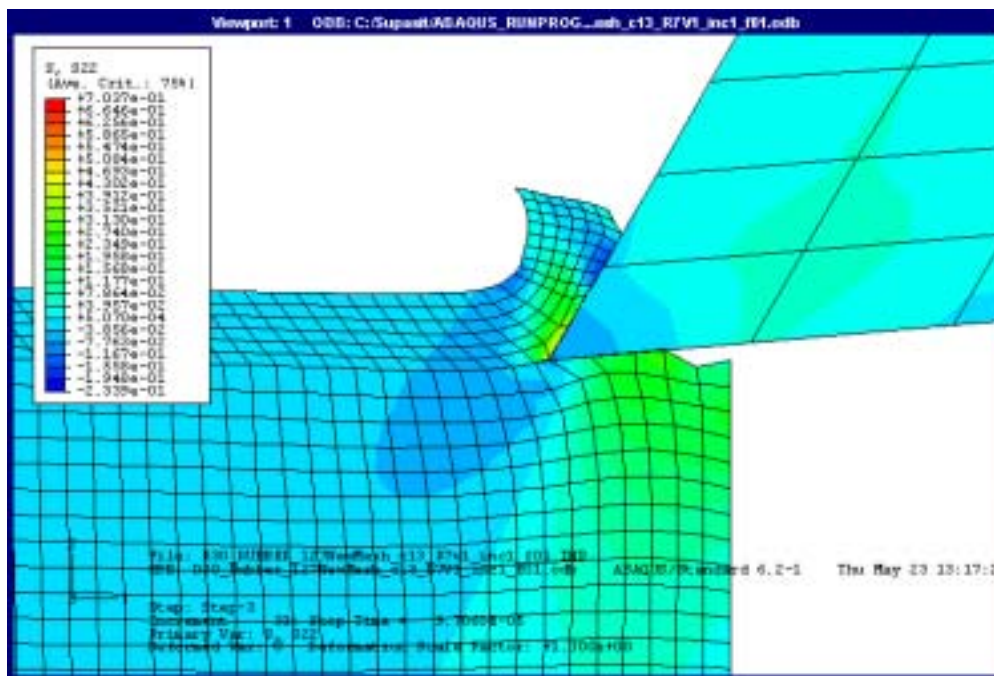


Figure 5.67 Normal stress contours (MPa) at the analysis step 3, increment 33.

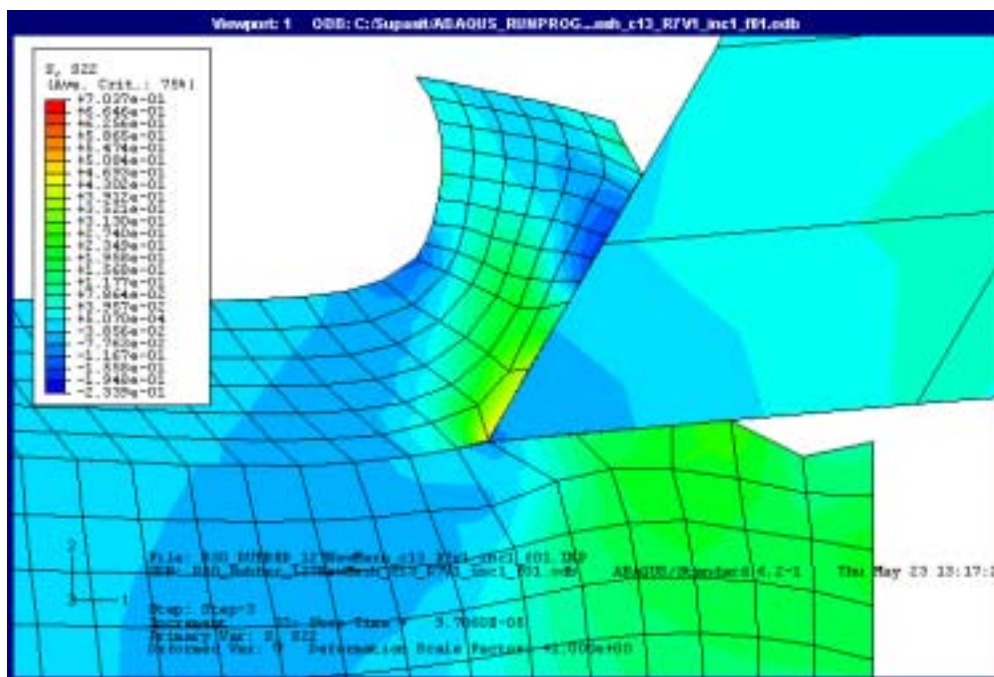


Figure 5.68 Normal stress contours (MPa) at the analysis step 3, increment 33 (detailed view).

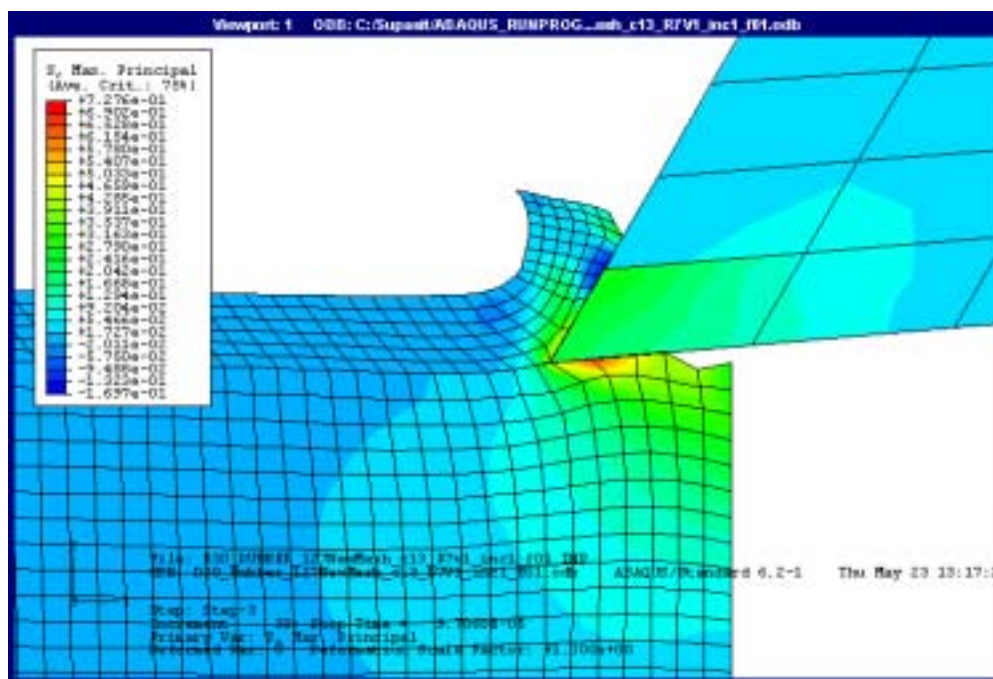


Figure 5.69 Maximum principal stress contours (MPa) at the analysis step 3, increment 33.

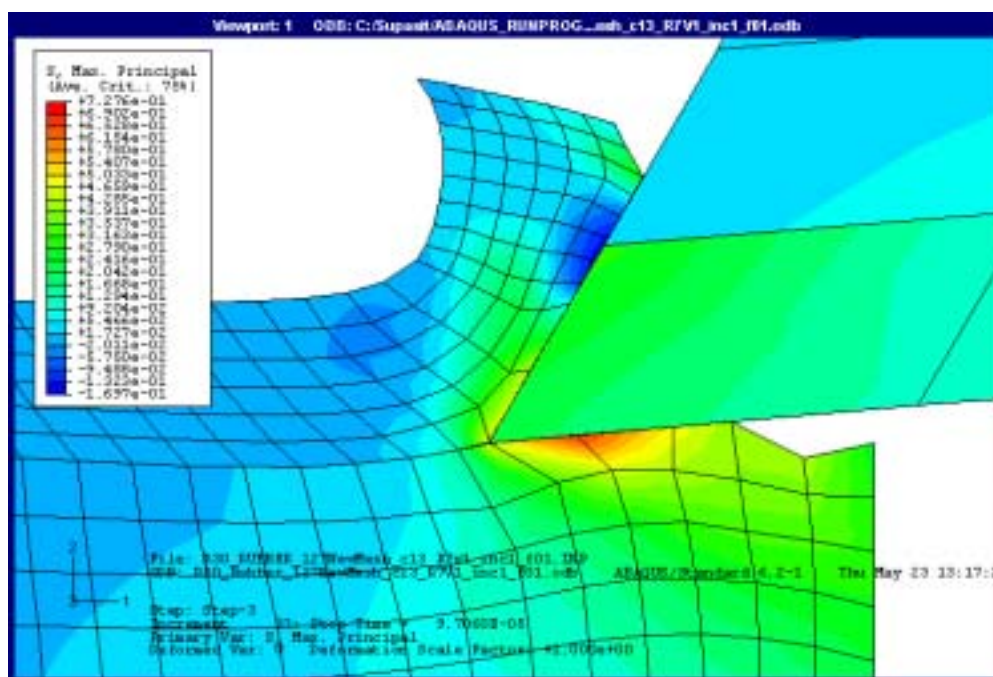


Figure 5.70 Maximum principal stress contours (MPa) at the analysis step 3, increment 33 (detailed view).

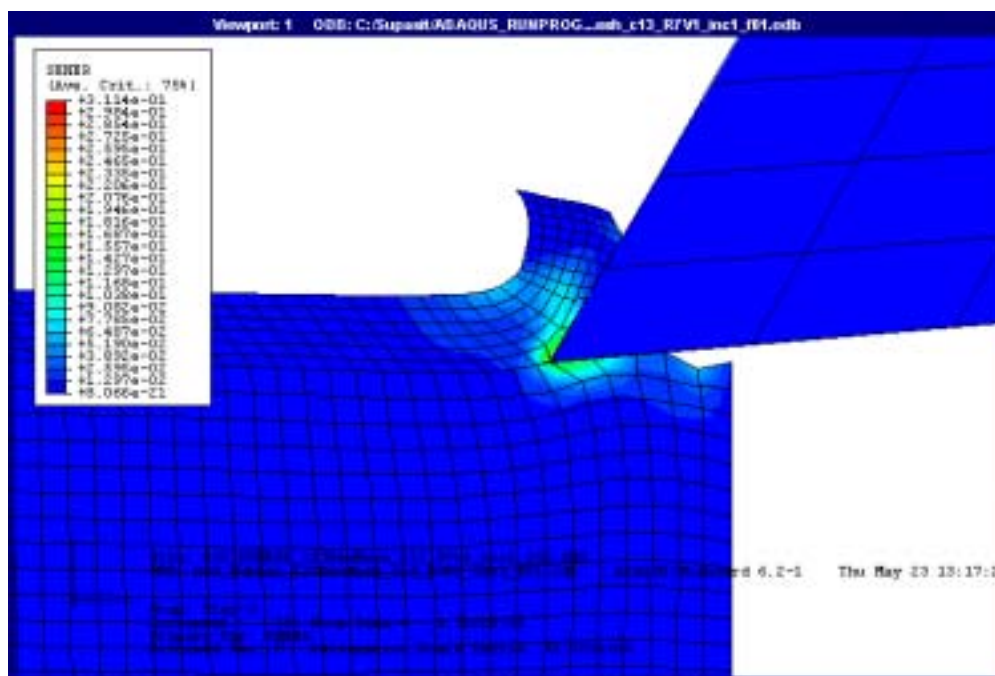


Figure 5.71 Strain energy density contours (MPa) at the analysis step 3, increment 33.

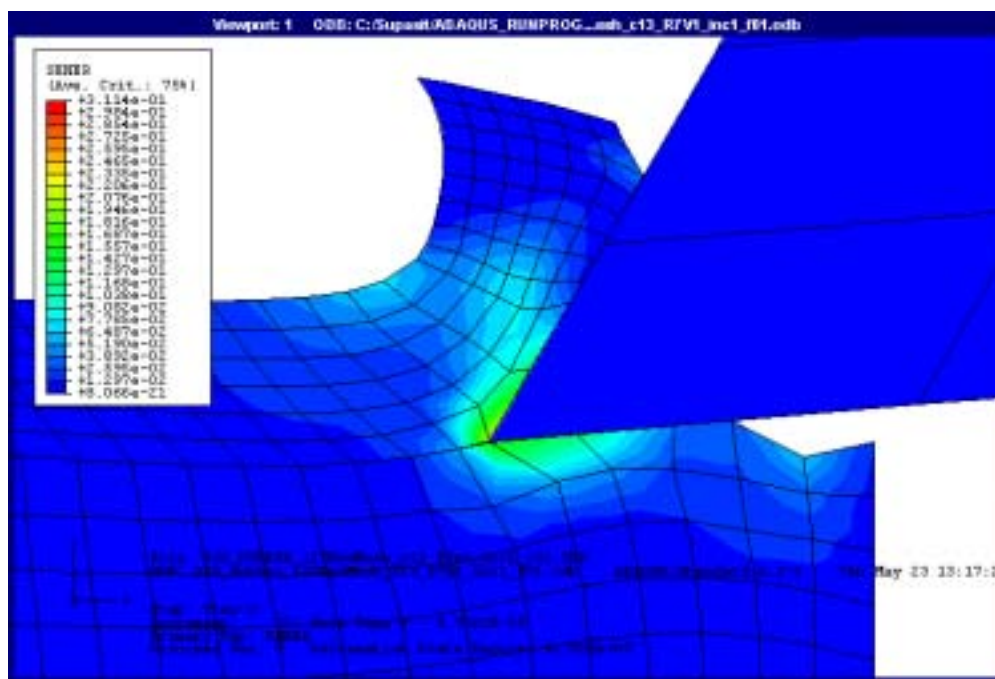


Figure 5.72 Strain energy density contours (MPa) at the analysis step 3, increment 33 (detailed view).

6. CONCLUSIONS AND FUTURE WORK

6.1 Conclusions

In this research, an investigation of the machinability of elastomers was undertaken using both orthogonal machining experiments and numerical simulations of wedge indentation as a precursor to incipient chip formation.

The effects of various machining parameters on chip morphology, machined surface roughness, and the associated machining forces were examined using orthogonal cutting tests. Feed speed and rake angle were found to have a significant effect on the types of chips generated during orthogonal cutting. Long and continuous ribbon-like chips and corresponding smooth machined surfaces were produced for high feed speed conditions and large rake angle tools. In addition, fixture design was also determined to be an important factor when machining elastomers.

Half-wedge indentation models of elastomers were developed to simulate incipient chip formation of elastomers. For comparison, a metal cutting simulation and half-wedge indentation of AISI 4340 steel with a sharp wedge were also conducted. Based on extensive analyses of indentation in terms of strain energy density and the normal and maximum principal stresses under the indenter tip, favorable conditions for which a chip would cleanly separate from the workpiece were identified. It was found that a tensile normal stress, a positive maximum principal stress and a highly concentrated strain energy density near the separation point were associated with continuous chip formation

and a smooth machined surface finish. The effects of the indenter half-wedge angle, edge radius of the indenter tip, feed, friction between the indenter and elastomeric workpiece, and fixture design of the workpiece were also investigated. Among the operating conditions and parameters investigated, a sharp indenter with a small half-wedge angle, in conjunction with a high feed, low friction coefficient and a highly rigid support of the workpiece generate stresses that create a tensile normal stress and large concentrated strain energy density under the indenter tip.

Good correlation was found between the indentation simulations and the orthogonal cutting tests. It was found that a tensile normal stress and a highly concentrated strain energy density near the separation point were associated with continuous chip formation and a smooth machined surface finish as obtained in the orthogonal cutting tests.

Preliminary results from an elastomer cutting model also revealed that the mechanism of chip formation for elastomers is very different for metals because no distinct shear deformation occurs in the primary shear zone.

6.2 Future Work

The empirical and numerical investigations performed in this research indicate that the machinability of elastomers can be improved with the proper choice of cutting conditions and tooling. Future research to further enhance the machinability of elastomers should address the following:

1. A variety of elastomeric materials should be studied to determine the applicability of the indentation models for a wide range of elastomer components.
2. More extensive mechanical and physical properties of elastomers including material data from uniaxial, equi-biaxial and pure shear tests should be determined for more accurate simulations.
3. Research should be initiated in fixture design to improve the rigidity and stiffness of the workpiece during machining.
4. The effect of temperature on elastomers such as cooling to increase the workpiece stiffness and rigidity should be examined to determine its usefulness for improving the machinability of elastomers.
5. A wider range of machining conditions such as cutting speed, feed speed, and tool geometry should be investigated to extend the results of this research.

6. A study of the failure modes of elastomers should be undertaken to better understand the complex nature of their material response. This information would be useful for developing more advanced tooling to improve the surface finish of elastomers.

7. The preliminary simulation of cutting of elastomers conducted in this research should be extended for other tool geometries and cutting conditions to more fully understand the mechanism of chip formation for elastomers.

REFERENCES

ABAQUS/Standard software Version 6.2 (2001), Hibbit, Karlsson & Sorensen, Inc., Pawtucket, RI.

ABAQUS/Explicit software Version 6.2 (2001), Hibbit, Karlsson & Sorensen, Inc., Pawtucket, RI.

ABAQUS/Explicit User's Manual Version 6.2 (2001), Hibbit, Karlsson & Sorensen, Inc., Pawtucket, RI.

ABAQUS/Standard User's Manual Version 6.2 (2001), Hibbit, Karlsson & Sorensen, Inc., Pawtucket, RI.

Advance Elastomer Systems (1998), "Coefficient of Friction –Santoprene Rubber Versus Steel, Aluminum and Polypropylene," Technical Correspondence:1-7.

Aklonis, J. J., W. J. MacKnight, et al. (1972), Introduction to Polymer Viscoelasticity, Wiley-Interscience.

ASTM (1999), Standard Terminology Relating to Rubber, ASTM 1566, Annal Book of ASTM Standards, Section 9: Rubber.

Athavale, S. M. and J. S. Strenkowski (1995), Material damage based model for predicting chip-breakability, ASME International Mechanical Engineering Congress and Exposition, Manufacturing Science and Engineering, San Francisco, CA.

Bhattacharya, A. K. and W. D. Nix (1988), "Finite element simulation of indentation experiments," International Journal of Solids and Structures **24**(9): 881-891.

Blatz, P. J., S. C. Sharda, et al. (1974), "Strain energy function for rubberlike materials based on a generalized measure of strain," Transactions of the Society of Rheology **18**(1): 145-161.

Briscoe, B. J. and K. S. Sebastian (1993), "An analysis of the "durometer" indentation," Rubber Chemistry and Technology **66**(5): 827-836.

Briscoe, B. J., K. S. Sebastian, et al. (1994), "The effect of indenter geometry on the elastic response to indentation," Journal of Physics. D: Applied Physics. **6**: 1156-1162.

Charlton, D. J. and J. Yang (1994), "A review of methods to characterize rubber elastic behavior for use in finite element analysis," Rubber Chemistry and Technology **67**(3): 481-503.

Dicarlo, A., H. T. Yang, et al. (2002), A semi-inverse method for predicting stress-strain relationship from cone indentation, 2002 NSF Design, Service and Manufacturing Grantees and Research Conference, San Juan, Puerto Rico.

Finney, R. H. and A. Kumar (1988), "Development of material constants for nonlinear finite-element analysis," Rubber Chemistry and Technology **61**(5): 879-891.

Getting Started with ABAQUS/Standard, Version 6.2 (2001), Hibbit, Karlsson & Sorensen, Inc, Pawtucket, RI.

Hill, R. (1950), "A theoretical investigation of the effect of specimen size in the measurement of hardness," The Philosophical Magazine **41**(312): 745-753.

Hill, R. (1953), "On the mechanics of cutting metal strips with knife-edged tools," Journal of the Mechanics and Physics of Solids **1**: 265-270.

Hill, R., E. H. Lee, et al. (1947), "The theory of wedge indentation of ductile materials," Proceedings of the Royal Society of London. Series A, Mathematical and Physical Sciences **188**(1013): 273-289.

Hsieh, C. (1998), Development of a force and temperature twist drill model for AISI 1020 steel, PhD Dissertation, Mechanical and Aerospace Engineering Department, North Carolina State University.

Jayadevan, K. R. and R. Narasimhan (1995), "Finite element simulation of wedge indentation," Computers & Structures **57**(5): 915-927.

Jerrams, S. J., M. Kaya, et al. (1998), "The effects of strain rate and hardness on the material constants of nitrile rubbers," Materials and Design **19**: 157-167.

Jin, M. and M. Murakawa (1998), "High-speed milling of rubber (1st Report) - Fundamental experiments and considerations for improvement of work accuracy," Journal of the Japan Society of Precision Engineering **64**(6): 897-901.

Johnson, W. (1958), "The cutting of round wire with knife-edge and flat-edge tools," Applied Scientific Research A VII: 65-88.

Karduna, A. R., H. R. Halperin, et al. (1997), "Experimental and numerical analyses of indentation in finite-sized isotropic and anisotropic rubber-like materials," Annals of Biomedical Engineering **25**: 1009-1016.

Kolman, R. and R. Rudziejewski (1968), "Turning of Rubber," Mechanik **41**(8): 431-435.

Komvopoulos, K. and S. A. Erpenbeck (1991), "Finite element modeling of orthogonal metal cutting," Journal of Engineering for Industry **113**(8): 253-267.

LabView 6i software (2001), National Instruments Inc., Austin, TX.

Liu, C. R. and Y. B. Guo (2000), "Finite element analysis of the effect of sequential cuts and tool-chip friction on residual stresses in a machined layer," International Journal of Mechanical Sciences **42**: 1069-1086.

Lockett, F. J. (1963), "Indentation of a rigid/plastic material by a conical indenter," Journal of the Mechanics and Physics of Solids **11**: 345-355.

Lovell, M. R., S. Bhattacharya, et al. (1998), Modeling of orthogonal machining processes for variable tool-chip interfacial friction using explicit dynamic finite element methods, Proceedings of the CIRP International Workshop on Modeling of Machining Operations, Atlanta, GA.

Mackerle, J. (2001), "Finite element boundary element simulations of indentation problems: A bibliography (1997-2000)," Finite Elements in Analysis and Design **37**: 811-819.

Mooney, M. (1940), "A theory of large elastic deformation," Journal of Applied Physics **11**(1): 582-592.

Ogden, R. W. (1997), Non-Linear Elastic Deformations, Dover Publications.

Okushima, K. and K. Hitomi (1963), "Transitional phenomenon in metal cutting," International Journal of Production Research **2**(3): 234-246.

Pidaparti, R. M. and G. Pontula (1995), "Fracture analysis of cracked rubber components in two and three dimensions," Theoretical and Applied Fracture Mechanics **22**: 1-8.

Rivin, R. S. (1948), "Large elastic deformations of isotropic materials. IV. Further developments of the general theory," Philosophical Transactions of the Royal Society of London. Series A, Mathematical and Physical Sciences **241**(835): 379-397.

Rivin, R. S. and A. G. Thomas (1953), "Rupture of rubber. I Characteristics energy for tearing," Journal of Polymer Science **10**(3): 291-318.

Shalaby, S. W. and B. G. Schwartz (1985), Plastics and Elastomers (Rubber), Materials and Processes, Part A: Materials, J. F. Young and R. S. Shane, Marcel Dekker.

Shet, C. and X. Deng (2000), "Finite element analysis of the orthogonal metal cutting process," Journal of Materials Processing Technology **105**: 95-109.

Shield, R. T. (1955), "On the plastic flow of metals under conditions of axial symmetry," Proceedings of the Royal Society of London. Series A, Mathematical and Physical Sciences **233**(1193): 267-287.

Shih, A. J. (1995), "Finite element simulation of orthogonal metal cutting," Journal of Engineering for Industry **117**(2): 84-93.

Shih, A. J. (1996), "Finite element analysis of the rake angle effects in orthogonal metal cutting," International Journal of Mechanical Science **38**(1): 1-17.

Shih, A. J. (1995), "Finite element simulation of orthogonal metal cutting," Journal of Engineering for Industry **117**(2): 84-93.

Shih, A. J. (1996), "Finite element analysis of orthogonal metal cutting mechanics," International Journal of Machine Tools & Manufacture **30**(2): 255-273.

Shih, A. J. (1996), "Finite element analysis of the rake angle effects in orthogonal metal cutting," International Journal of Mechanical Science **38**(1): 1-17.

Shih, A. J., M. A. Lewis, et al., [a], (To be published), "Chip morphology and forces in end milling of elastomers," Journal of Manufacturing Science and Engineering.

Shih, A. J., M. A. Lewis, et al., [b], (To be published), "End milling of elastomers-Fixture design and tool effectiveness for material removal," Journal of Manufacturing Science and Engineering.

Strenkowski, J. S. and J. T. Carroll (1985), "A finite element model of orthogonal metal cutting," Journal of Engineering for Industry **107**(11): 349-354.

Strenkowski, J. S. and J. T. Carroll (1986), An orthogonal metal cutting model based on an Eulerian finite element method, Manufacturing Process Machines and Systems, 13th Conference on Production Research and Technology, U. of Florida, FL.

Strenkowski, J. S. and G. L. Mitchum (1987), An improved finite element model of orthogonal metal cutting, Proceedings of North America Manufacturing Research Conference, Bethlehem, PA.

Strenkowski, J. S. and K. J. Moon (1990), "Finite element prediction of chip geometry and tool/workpiece temperature distributions in orthogonal metal cutting," Journal of Engineering for Industry **112**(11): 313-318.

Strenkowski, J. S., A. J. Shih, et al. (2002), Machining of Elastomers, 2002 NSF Design, Service and Manufacturing Grantees and Research Conference, San Juan, Puerto Rico.

Strenkowski, J. S. and J. T. Carroll (1985), "A finite element model of orthogonal metal cutting," Journal of Engineering for Industry **107**(11): 349-354.

Strenkowski, J. S. and J. C. Lin (1996), An analytical finite element model for predicting three-dimensional tool forces and chip flow, ASME International Mechanical Engineering Congress and Exposition, Manufacturing Science and Engineering, Atlanta, GA.

Strenkowski, J. S. and K. J. Moon (1990), "Finite element prediction of chip geometry and tool/workpiece temperature distributions in orthogonal metal cutting," Journal of Engineering for Industry **112**(11): 313-318.

Treloar, L. R. (1958), The Physics of Rubber Elasticity, Oxford University Press.

Unanue, I., J. Rubio, et al. (2001), Simulation of machining processes: Orthogonal cutting of common steels, ABAQUS Users' Conference, Maastricht, Netherlands.

Usui, E., T. Shirakashi, et al. (1978), "Analytical prediction of three dimensional cutting process: Part 3 Cutting temperature and crater wear of carbide tool," Journal of Engineering for Industry **100**(5): 236-243.

Valanis, K. C. and R. F. Landel (1967), "The strain-energy function of a hyperelastic material in terms of extension ratios," Journal of Applied Physics **38**(7): 2997-3002.

Waters, N. E. (1965), "The indentation of thin rubber sheets by cylindrical indentors," British Journal of Applied Physics **16**(9): 1387-1392.

Weinmann, K. J. (1977), "On wedge indentation and its relationship with incipient plastic deformation in metal cutting," Journal of Engineering for Industry **99**(3): 702-707.

Weinmann, K. J. and B. F. V. Turkovich (1971), "Mechanics of tool-workpiece engagement and incipient deformation in machining of 70/30 brass," Journal of Engineering for Industry **93**(4): 1079-1089.

Yeoh, O. H. (1993), "Some forms of the strain energy function for rubber," Rubber Chemistry and Technology **66**(5): 754-771.